Thermocapillary Motion of Droplets in Complex Fluid Flows

PhD Thesis

Paolo Capobianchi

James Weir Fluids Laboratory

Department of Mechanical and Aerospace Engineering

University of Strathclyde

February 21, 2019

"...fatti non foste a viver come bruti, ma per seguir virtute e canoscenza."
("...you were not made to live as brutes, but to pursue virtue and knowledge.")

Dante Alighieri, Inferno, Canto XXVI: Ulisse

Declaration

This thesis is the result of the author's original research. It has been composed by the author and has not been previously submitted for examination which has led to the award of a degree. The copyright of this thesis belongs to the author under the terms of the United Kingdom Copyright Acts as qualified by University of Strathclyde Regulation 3.5.0. Due to acknowledgment must always be made of the use of any material contained in, or derived from, this thesis.

Paolo Capobianchi,

University of Strathclyde, 21/09/2018

Research output

The outcomes of the work developed during this PhD include one (1) book chapter, the contents of which are presented in chapter 3; two (2) publications in international journals, and another paper in preparation. Moreover, different parts of this research have been presented in conferences, with six (6) oral presentations and two (2) posters, in order to disseminate the research performed, and discuss and receive feedback from experts in the field.

Journal papers

1. Capobianchi P., Morozov A., Lappa M., Oliveira M. S. N., Thermocapillary motion and shape of a Newtonian droplet in a dilute viscoelastic fluid, (paper in preparation).

2. Capobianchi P., Lappa M., Oliveira M. S. N., Deformation of a ferrofluid droplet in a simple shear flow under the effect of a constant magnetic field, Computers and Fluids, 2018, 173, 313-323.

3. Capobianchi P., Lappa M., Oliveira M. S. N., Walls and domain shape effects on the thermal Marangoni migration of three-dimensional droplets, Physics of Fluids, 2017, 29, 11, 112102.

Book chapters

1. Capobianchi P., Lappa M., Oliveira M. S. N., Implementation of a flexible and modular multiphase framework for the analysis of surface-tension-driven flows based on a LS-VOF approach, OpenFOAM: Selected Papers of the 11th Workshop. Nóbrega, J. & Jasak, H. (editors), Springer, 2018.

Conference talks

1. Capobianchi P., Lappa M., Oliveira M. S. N., Deformation of ferrofluid droplets: the interplay between shear flow and magnetic field, ECCM/ECFD, June 2018, Glasgow, UK.

2. Capobianchi P., Lappa M., Oliveira M. S. N., Prediction of the rheological properties of a dilute ferrofluid emulsion under the influence of a constant magnetic field, 31th Scottish Fluid Mechanics Meeting, May 2018, Aberdeen, UK.

3. Capobianchi P., Lappa M., Oliveira M. S. N., Thermocapillary motion of a Newtonian droplet in a viscoelastic fluid under Stokes flow conditions, AERC, April 2018, Sorrento, Italy.

4. Capobianchi P., Lappa M., Oliveira M. S. N., Numerical simulations of the thermocapillary migration of a deformable Newtonian droplet in an Oldroyd-B matrix fluid in Stokes flow conditions, 30th Scottish Fluid Mechanics Meeting, May 2017, Glasgow, UK.

5. Capobianchi P., Lappa M., Oliveira M. S. N., Thermal Marangoni migration of droplets in an Oldroyd-B fluid under creeping flow conditions, The Society of Rheology: 88th Annual Meeting, February 2017, Tampa, Florida, US.

6. Capobianchi P., Lappa M., Oliveira M. S. N., Implementation of a flexible and modular volume of fluid multiphase solver for non-isothermal incompressible flows, 11th OpenFOAM workshop, June 2017, Guimarães, Portugal.

Conference posters

1. Capobianchi P., Lappa M., Oliveira M. S. N., Behavior of a ferrofluid droplet under the combined effect of a uniform magnetic field and a simple shear flow, AERC, April 2018, Sorrento, Italy.

2. Capobianchi P., Lappa M., Oliveira M. S. N., Development of a multiphase solver for numerical simulations of thermally driven Marangoni flows, 29th

Abstract

Understanding how the presence of thermal gradients affects the motion of bubbles and drops is a subject of great relevance both from a theoretical and a practical standpoint, particularly when gravitational effects are minimal or completely uninfluential. In the past half century, considerable progress has been made on the investigation of the so-called thermocapillary phenomenon in an attempt to clarify the mechanisms at work in multiphase systems with liquid-liquid or liquid-gas interfaces. Given the complexity of the problem, most of these investigations have been carried out under simplified conditions, assuming unbounded flows or considering relatively simple geometries in which the presence of solid boundaries was not explicitly taken into account. Additionally, even though non-Newtonian fluids are ubiquitous in engineering and science, the majority of these works have been carried out assuming Newtonian phases.

The aim of the present thesis is to study the thermocapillary migration of a droplet in systems exhibiting an added level of complexity, specifically in terms of wall effects, domain shape and rheological properties of the fluids. To accomplish these objectives, we rely on a concerted approach based on well-established numerical strategies and, where possible, we derive analytical solutions. A thermocapillary solver based on a hybrid Level Set-Volume of Fluid method available in OpenFOAM has been implemented and validated against previous analytical results, numerical solutions and experimental observations obtained in reduced gravity conditions (Sect. 3.5). In the first part of the study, we investigate the problem of a droplet interacting with the boundaries of a parallelepipedic domain. The case study has been assessed by releasing the droplet in proximity to the lateral walls of the domain considering both adiabatic and purely conductive boundary conditions. The results showed that the droplet can experience a sec-

ondary motion perpendicular to the main direction of motion. In particular, it was observed that the droplet can either move away or towards the walls depending on the thermal boundary conditions at the wall (i.e., whether the wall is adiabatic or purely conductive) and on the extent of convective phenomena. The investigation was then extended by adopting more complex geometries (converging and diverging channels), which were found to produce distortion of the thermal field distribution with direct consequences on the migration process (Sect. 4.2.1 and 4.2.2). In the second part of the thesis, non-Newtonian effects have been expressly considered. Specifically, the role played by the fluid's elasticity (while neglecting convective transport of energy and momentum) has been accounted for by modelling the continuous phase on the basis of constant-viscosity viscoelastic models, namely the Oldroyd-B model and FENE-CR model. The numerical simulations were carried out for a specific value of the Capillary number and assuming the same material properties for both phases. We investigated the effects of the various model parameters (i.e., polymer concentration and extensibility parameter) and Deborah number on the droplet motion. The results showed that the droplet speed, evaluated as a function of the Deborah number, initially decreases following a quadratic trend. For larger Deborah number, the trend reverts its concavity and eventually reaches a plateau. In terms of shape, the results have shown that under the prescribed conditions the droplet deforms in a prolate manner and, for sufficiently large values of the Deborah number (having fixed the Capillary number), the viscoelastic stresses localised at the rear stagnation point are responsible for the formation of a pointed tail. The viscoelastic problem was also tackled by means of perturbation techniques under the assumption of absence of confinement and weak viscoelastic effects, which allowed the derivation of corrective formulae for the droplet migration velocity and expressions describing the shape of the deformed drop. The results of the analytical solutions were found to be in fairly good agreement with the outcomes of the computations, both in terms of drop shape and migration speed.

To my beloved Family. Especially to my nephew Edoardo, with the hope that this modest work will inspire you to accomplish something much greater.

Acknowledgements

It has been indeed rather strenuous and challenging arriving up to this point, and if I have managed to do so, it is also because of the precious contribution of invaluable people which I wish to thank in a special manner. First, I want to expresses my gratitude to my supervisors, Dr. Mónica S. N. Oliveira and Dr. Marcello Lappa for their invaluable support, patience and enthusiasm on guiding me along all these years. I wish to thank you for encouraging my research and giving me the motivation to keep pursuing it, especially during the most difficult moments. I consider myself extremely fortunate for having had the opportunity and privilege to work with you on the extraordinary worlds of non-Newtonian fluid mechanics and thermocapillary flows. I am also very grateful to Dr. Alexander Morozov for his patience, good will and meticulous support on helping me during the derivation of the analytical solution presented in Chapter 6 of this thesis. It is hard to believe that I could have managed to arrive to the same conclusions without your support. A special thanks also goes to my friends Dr. Vincent Casseau and Dr. Thomas Burel for helping me to get started with OpenFOAM and UNIX environments. Your help saved me from quite a few troubles. Many other people have contributed in different ways and different extents to this work, but unfortunately I cannot thank all of you separately, otherwise I would need another month to finish the thesis and actually I do not want to do so. I believe that you know who you are and that you will understand. Finally, my deepest thank goes to my dear parents who believed in me and constantly gave me their support along this endless journey through my formal education. Without you, this work never would have seen the light of day.

List of Figures

12

15

List of Tables

17

List of symbols

Latin symbols

A   Conformation (or configuration) tensor;

A_{xx}, A_{yy}, A_{zz}, A_{yz} Cartesian components of the conformation tensor;

a Droplet minor axis;

a_T Shift factor;

b Droplet major axis;

c Polymer concentration parameter;

C Confinement ratio;

C_1, C_2 Constants adopted to evaluate the optimal time step on the basis of stability considerations;

C_α Interface compression limiter;

Ca Capillary number;

Co_{Max} Maximum Courant number;

c_p Heat capacity [Jkg^{-1} K^{-1}];

$c_{p,d}$ Droplet fluid heat capacity [Jkg^{-1} K^{-1}];

$c_{p,m}$ Matrix fluid heat capacity [Jkg^{-1} K^{-1}];

$c_{p,r}$ Drop-to-matrix heat capacity ratio;

D Deformation parameter;

d Distance for the wall from the centre of the domain;

D   Twice the rate-of-strain tensor [s^{-1}];

D_1, D_2 Droplet major and minor axes;

D_a Droplet major-to-minor axes ratio;

De Deborah number;

De_T Thermal Deborah number;

18

$\hat{d}$ Upper-convected derivative operator [s^{-1}];

D_{th} Thermal diffusivity [m^{2}s^{-1}];

$\mathbf{E}$ Rate-of-strain tensor in tensor notation [s^{-1}];

e Eccentricity;

E_{ij} Rate-of-strain tensor in Einstein notation [s^{-1}];

F_c Compressive volume fraction flux;

$\mathbf{f}_S$ Generic surface force at the interface [Nm^{-3}];

$\mathbf{f}_\sigma$ Interfacial force [Nm^{-3}];

$\mathbf{f}_{\sigma,\mathbf{n}}$ Normal interfacial force [Nm^{-3}];

$\mathbf{f}_{\sigma,\mathbf{t}}$ Tangential interfacial force [Nm^{-3}];

F_u Volume fraction flux [ms^{-1}];

$\mathbf{g}$ Acceleration of gravity [ms^{-2}];

G Elastic modulus of an Hookean material [Nm^{-2}];

h Computational domain height;

$\mathbf{I}$ Identity tensor;

$\mathcal{I}$ Volume fraction indicator function for fluid "i";

I Level-set indicator function;

k Interface curvature [m^{-1}];

k_1, k_2 Constants adopted for the interpolation of the migration velocity obtained for the simulations of the viscoelastic Oldroyd-B case;

K_{ijmn} Generic fourth-order tensor made of constant coefficients in Einstein notation [Nm^{-2}s];

k_h Discrete curvature at the interface [m^{-1}];

L Domain length;

L^2 Extensibility parameter;

M_1, M_2, M_3 Mesh refinement levels;

Ma Marangoni number;

m Mass of the sphere of a dumbbell [kg];

$\mathbf{n}$ Normal unit vector at the interface;

$\mathbf{n}_h$ Discrete normal unit vector at the interface;

n Number of smoothing (mollification) cycles;

N_1, N_2 First and second normal stress coefficients;

$\mathbf{n}_f$ Cell face normal;

$\mathbf{n}_\varphi$ Normal unit vector at the interface evaluated with the level set function;

$\mathbf{n}_{\varphi,mol}$ Normal unit vector at the interface evaluated with the mollified level set function;

p Pressure [Pa];

Pr Prandtl number;

$\mathbf{q}$ Heat flux density [Wm^{-2}];

R Drop radius [m];

Re Reynolds number;

$\mathbf{r}$ Radius of gyration [m];

s Distance of the drop centre from the wall, auxiliary variable [m];

$\mathbf{S}_f$ Cell face vector;

t Time [s];

T Temperature;

T_0 Reference temperature [K];

T_{cold} Temperature of the cold side of the domain [K];

T_{hot} Temperature of the hot side of the domain [K];

t' Dimensionless time;

t_T Characteristic time of the thermal convection [s];

U Droplet velocity [ms^{-1}];

$\mathbf{u}$ Velocity vector field [ms^{-1}];

U_0 Newtonian dimensionless droplet velocity, imposed boundary velocity adopted for simulation of the Couette flow [ms^{-1}];

$\mathbf{u}_c$ Artificial compressive velocity [ms^{-1}];

$\mathbf{u}_f$ Velocity interpolated at the cell face [ms^{-1}];

U_T Reference thermal velocity [ms^{-1}];

U_{YGB} Young, Goldstein, Block droplet velocity [ms^{-1}];

V Volume of the computational cell [m^3];

w Domain width [m];

w_{cold} Domain cold side width [m];

w_{hot} Domain hot side width [m];

x   Vector position;

(x, y, z) Coordinates of a Cartesian frame of reference;

Greek symbols

α Viscosity ratio;

α_k Volume fraction function;

$\alpha_{k,mol}$ Mollified volume fraction function;

$\alpha_{k,mol}^*$ Mollified volume fraction function adopted for the adaptive mesh refinement;

$\alpha_{k,thr}^*$ Threshold of the mollified volume fraction function adopted for the adaptive refinement;

α_{th} Thermal diffusivity ratio;

β Viscoelastic viscosity ratio using notation $\beta = \eta_s/\eta_0$;

Γ Computational cell domain, parameter adopted in the level-set method, gamma function;

γ Density ratio;

$\dot{\gamma}$ imposed shear rate [s^{-1}];

$\Delta x, \Delta y, \Delta z$ Grid resolution along the coordinate axes;

δ Distribution at the interface [m^{-1}];

δ_{ij} Kronecker delta;

ε Empirical parameter adopted in the Level-Set method;

$\dot{\varepsilon}$ Elongational strain rate [s^{-1}];

ζ Shape function;

ζ_M MULES limiter;

η Viscosity [Pa s];

η_0 Zero-shear viscosity [Pa s];

$\eta_{0,m}$ Matrix fluid zero-shear viscosity [Pa s];

η_d Droplet fluid viscosity [Pa s];

η_{ext} Extensional viscosity [Pa s];

η_m Matrix fluid viscosity [Pa s];

η_p Polymer viscosity [Pa s];

$\eta_{p,m}$ Matrix fluid polymer viscosity [Pa s];

η_r Drop-to-matrix viscosity ratio;

η_s Solvent viscosity [Pa s];

$\eta_{s,m}$ Matrix fluid solvent viscosity [Pa s];

θ Degree of proximity;

κ Thermal conductivity [Wm^{-1}K^{-1}];

κ_d Drop thermal conductivity [Wm^{-1}K^{-1}];

κ_m Matrix thermal conductivity [Wm^{-1}K^{-1}];

κ_r Drop-to-matrix thermal conductivity ratio;

λ Relaxation time [s];

λ_r Retardation time [s];

ν relaxation time ratio;

ν_r Retardation time ratio;

ξ Drop axis;

ρ Fluid density [kgm^{-3}];

ρ_d Drop density [kgm^{-3}];

ρ_m Matrix density [kgm^{-3}];

ρ_r Drop-to-matrix density ratio;

$\mathbf{\Sigma}$ Cauchy stress tensor [Nm^{-2}];

σ Interfacial tension [Nm^{-1}];

σ_T Interfacial tension temperature gradient [Nm^{-1}K^{-1}];

$\varsigma_{k,mol}$ Generic mollified variable;

$\boldsymbol{\tau}$ Stress tensor in tensor notation [Nm^{-2}];

τ_f Fictitious time step;

τ_{ij} Stress tensor in Einstein notation [Nm^{-2}];

τ_{mol} Fictitious mollified time step [s];

$\boldsymbol{\tau}_p$ Polymer stress tensor [Nm^{-2}];

$\boldsymbol{\tau}_s$ Solvent stress tensor [Nm^{-2}];

φ Droplet orientation angle [deg];

φ_k Level-set function;

$\varphi_{k,0}$ Initial level-set function;

$\varphi_{k,mol}$ Mollified level-set function;

χ Generic material property;

χ_d Generic material property for the drop;

χ_m Generic material property for the matrix fluid;

χ_r Drop-to-matrix generic material property ratio;

Ω_{ij} Vorticity tensor [s^{-1}];

(r, θ, ϕ) Spherical frame of reference coordinates;

Acronyms

AMR   Adaptive mesh refinement;

AR   Overall geometry aspect ratio;

CSF   Continuum surface force model;

CSS   Continuum surface stress model;

ER   Expansion ratio;

FVM   Finite volume method;

ISS   International space station;

LBM   Lattice Boltzmann method;

LS, LSM   Level-Set method;

MAC   Marker and Cell method;

MULES   Multi-dimensional limiter for explicit solution;

NC   Near corner configuration;

N-N   Newtonian-Newtonian configuration;

NS   Near side configuration;

N-V   Newtonian-Viscoelastic configuration;

PISO   Pressure-implicit with splitting operator algorithm;

PROST   Parabolic reconstruction of the surface tension model;

QUICK   Quadrratic upwind interpolation for convective kinematics;

SOLA-VOF   Solution algorithm for transient fluid flow with multiple free boundaries;

SPH   Smoothed-particle Hydrodynamics method;

V-N   Viscoelastic-Newtonian configuration;

VOF   Volume of Fluid method;

V-V   Viscoelastic-Viscoelastic configuration;

YGB   Young, Goldstein, Block

Other symbols

∇ Gradient operator [m^{-1}];

∇_h Discrete gradient operator [m^{-1}];

$\nabla_h T$ Discrete temperature gradient [Km^{-1}];

$\nabla_\infty T$ Imposed temperature gradient [K];

$\nabla_s \sigma$ Surface (tangential) interfacial tension gradient [Nm^{-2}];

$\nabla_s T$ Surface (tangential) temperature gradient [Km^{-1}];

$\sim$ Used to indicate variables and material quantities referred to the the dispersed phase (droplet);

Contents

Chapter 1

Introduction

This thesis focuses on the dynamics of thermocapillary motion of droplets immersed in immiscible liquids in complex flow configurations. In this chapter, we first provide a brief introduction of the thermocapillary migration problem providing a qualitative explanation of the physical mechanisms responsible for the thermally-driven motion of a drop or a bubble. Then, we present a comprehensive overview of the existing literature subdivided according to the various approaches that have been used for the investigation of the flow under discussion. Finally, we discuss the motivation for the present work and finalise with an outline where we provide a detailed list of all the topics discussed in each chapter.

1.1 Literature review

Fluid particles motion is relevant in a variety of industrial processes and technological applications. Manipulation of many substances often involves the presence of two immiscible fluids in contact each other where heat and/or mass transfer between the two phases can be a requirement for the desired process (see, e.g., Han, 1981). Such goal can be efficiently achieved when one phase is continuously dispersed into another (carrier phase), i.e., is in the form of small droplets (or bubbles, when the dispersed phase is a gas). Understanding the behaviour of these systems requires the accurate knowledge of the motion and deformation of a single fluid particle (or the interaction between some of them) in simplified conditions (e.g., by neglecting inertial effects, as in the case of the gravitational rise or sedimentation in isothermal Stokes flows (Hadamard, 1911 and Rybczynski,

1911)). Even in absence of gravity, if the system is affected by the presence of interfacial tension gradients, the consequent imbalance of capillary stresses can also be responsible for fluid particle displacements and/or deformations. This class of flows, which are usually termed Marangoni flows, after the Italian physicist Carlo Marangoni, who was the first to provide a theoretical description in his doctoral dissertation (Marangoni, 1871), have been firstly described by James Thomson, who gave a basic explanation of the so-called "tears of wine" phenomenon (Thomson, 1855). Subsequently, a more complete theoretical treatment was provided by the American scientist Josiah Willard Gibbs, who gave a detailed description of the phenomenon on his work "On the equilibrium of heterogeneous substances" (Gibbs, 1878).

Generally speaking, interfacial tension gradients can be induced, for instance but not only, by a non-uniform distribution of surface active compounds (e.g., surfactants) at the interface (in such a case the flow is termed solutal Marangoni flow), or due to the presence of interfacial temperature gradients, and in such a case the motion is usually called thermocapillary, or thermal Marangoni flow (see, for instance Subramanian and Balasubramaniam, 2001).

The investigation of the thermocapillary motion of bubbles and drops dates back to late 1950s, when Young et al. (1959) provided the experimental evidence that an air bubble surrounded by a heavier immiscible liquid can be maintained at rest (or move against the gravitational motion) under the application of an appropriate temperature gradient in such a way that the corresponding resultant of the thermocapillary and viscous forces balanced exactly the gravitational force. The same authors derived a landmark solution (in analytical form) of the governing equations under some limiting assumptions (cf. Sect. 2.4 and Sect. 6.3). In such an approach, velocity and temperature fields were considered to be fully established at every moment in time under the assumption of negligible inertia and convective transport of energy. With this approximation the temperature field and the flow field decouple allowing the derivation of an analytical solution to the problem (in the following also referred as YGB theory).

Following the work of Young et al. (1959), an increasing number of researchers

over the years have addressed the problem under discussion. This was essentially made possible by the availability of reduced gravity environment facilities, by the increased performances of computers and to the progressive development of sophisticated computational methodologies for the numerical representation of problems involving moving interfaces.

In the following, we provide a thorough review of the works related to thermo-capillary motion of bubbles and drops in reduced gravity environments produced in the past years. Due to the variety of different approaches used, we found advisable to subdivide the discussion according to the technique adopted for their investigation.

1.1.1 Experiments in reduced gravity conditions

An important implication inherent to the YGB theory, is the possibility to use temperature gradients alone to produce droplet motion, when these are not overwhelmed by buoyancy effects. Performing experiments in such conditions is usually very problematic on Earth. One in fact should either adopt density matched fluids (but also in this case it should be taken into account that the two fluids might have different thermal expansion coefficients, meaning that as the drop moves toward regions at different temperature, their densities will change in a different fashion), or consider situations in which the characteristic dimension of the fluid particles is very small, as for the case of atomised droplets (see, e.g. Grant et al. 1990, Arienti M. and Sussman M., 2017), or in microfluidic devices (see, e.g., Karbalaei et al., 2016). The obvious alternative would be conducting experiments in microgravity conditions. Here, we provide an account of the progresses made in this particular context.

The first systematic study in a reduced gravity environment was conducted by Thompson and co-workers in 1979 (Thompson, DeWitt and Labus, 1980), 20 years after the pioneering experiment of Young and co-workers (Young et al., 1959). The investigation was conducted in a drop tower at NASA's Lewis Research Centre using ethylene glycol, silicone oil, ethanol and water as the continuous phase, and nitrogen bubbles as the dispersed phase. The experiments

revealed a clear Marangoni effect for the case of ethylene glycol, silicone oil and ethanol, while no migration was observed in water. It is interesting to point out that the migration velocity of the nitrogen bubbles in ethylene glycol was in agreement with the YGB theory despite the flow conditions being beyond the limit of its applicability. Szymczyk and co-workers carried out experiments aboard of the space shuttle in 1985 (Szymczyk, Wozniak and Siekmann, 1987). Systems of water drops in silicone oil and air bubbles in silicone oil were considered. Also in this case the experiments revealed absence of thermocapillary flow in the presence of a water phase. It is interesting to note that despite water being characterised by strong variations of the surface tension with the temperature, in both experiments discussed above, no Marangoni flow was observed in the presence of aqueous phases. This was attributed to the tendency of water to be contaminated by impurities, which might prevent the activation of the mechanism necessary for the development of thermocapillary flows (see, e.g., Thompson et al. 1980). In a subsequent experiment, Wozniak observed the thermocapillary motion of paraffin drops in a water-ethanol mixture during and experiment conducted aboard of a sounding rocket (Wozniak, 1991). The results obtained for the droplet velocity were in qualitative agreement with a numerical solution exhibiting differences within 30%. A few years later, another experiment on a sounding rocket was performed by Braun and co-workers (Braun et al. 1993). They considered a mixture of 2-butoxyethanol and water with inverted miscibility gap. The system was initially kept at a temperature below the phase separation limit. Immediately after the beginning of the experiment, the temperature was increased to 0.45 K above the separation limit and drops rich in 2-butoxyethanol were enucleated. The drops were observed to move toward the cold side, which is consistent with the fact that in this specific system the interfacial tension is an increasing function of the temperature. The flow conditions were such that convective transport effects were negligible and the results were in agreement with the velocity predicted by the YGB theory. More recently, Treuner et al. (1996) studied the thermocapillary motion of air bubbles in three different organic liquids: n-octane, n-decane and n-tetradecane released from a drop tower. The same authors provided a

numerical solution used for comparison, which showed an agreement of about 20% with the experimental findings. Finally, several other results were obtained during a series of experiments conducted aboard of the space shuttle Columbia by Balasubramaniam and co-workers. The investigations were conducted in two different missions (1994 and 1996) and detailed accounts are reported in Balasubramaniam et al. (1996) and in Hadland et al. (1999). This latter work is particularly relevant in the context of this thesis as it was used for the validation of our solver (cf. Sect. 3.5.2). In the experiment of Hadland et al. (1999), a 60 mm long container having a square cross section 45×45 mm was filled with silicone oil having nominal kinematic viscosity of 10 centistokes. The two opposite square sections were made of aluminium and kept at different temperatures by Peltier elements. The other four sides of the cell were made of fused silica coated with a thin film of Indium. Two different series of tests were performed by injecting air bubbles or drops of fluorinert FC-75 from an injection port placed in the middle of the "cold" aluminium element. For each test, a single bubble (or a drop) was injected and monitored until it reached the opposite side of the cell. Fig. 1.1 summarises the results in terms of velocity migration normalised by the velocity provided by the YGB theory obtained for the experiments with fluorinert drops available in Hadland et al. (1999). The abscissa represents a dimensionless group called Marangoni number, which provides an indication of the relative extent of thermal convection compared to its diffusive counterpart (cf. Sect 2.4 for a detailed description of all the parameters adopted in this thesis). It is evident the monotonic decreasing velocity trend, however it is worth pointing out that the dimensional drop velocity is actually increasing for increasing values of the Marangoni number since this parameter is directly proportional to the extent of the thermocapillary driving force. Numerical simulations carried out by Ma (1998) have been added as they also appear in the original plot available in Hadland et al. (1999).
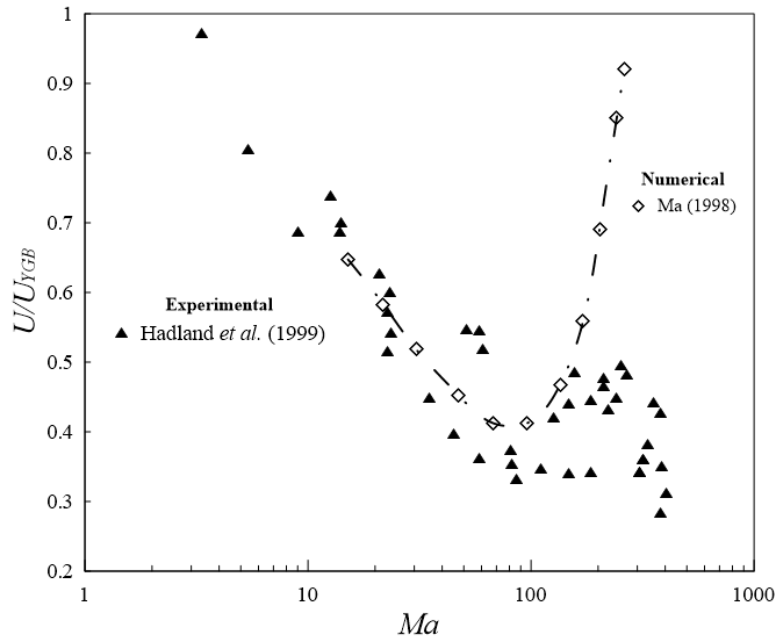
Figure 1.1: Normalised droplet migration velocity as a function of the marangoni number for a fluorinert drop embedded in silicone oil reported in the experiments Hadland et al. (1999). The open symbols represents the results of the numerical simulations of Ma (1998).

1.1.2 Solution of the problem by means of analytical and computational techniques

After the initial study of Young et al. (1959) most ensuing works have been devoted to assessing the role played by mechanisms which were neglected in that initial work. As an example, Subramanian (1983) included the effect of convective transport of energy as a small perturbation (setting the Reynolds number, Re, equal to zero and using a perturbation expansion in the Marangoni number for $Ma < 1$); in practice, inertial terms were neglected in the momentum equation (as we shall see later on in Sect. 2.4, the Reynolds number measures the relative importance of inertia in respect to viscous forces, thus, setting it to zero means that the inertial contributions are entirely ignored) whereas they were preserved in the energy equation (from a physical point of view this would be equivalent to considering a fluid with Prandtl number $Pr = MaRe \gg 1$, i.e., a liquid with a very high viscosity and a relatively small thermal diffusivity, since the Prandtl number compares the extent of molecular diffusion of the fluid relative to its thermal counterpart, therefore it actually represents a fluid property). Subramanian

(1983) showed that in such conditions the migration speed of a drop can be reduced or enhanced with respect to the analytical solution by Young et al. (1959) depending on the values of the various parameters.

The opposite case, in which convective transport of heat is ignored (in the limit of $Ma \to 0$) but small inertial effects are included in the momentum equation ($Re \neq 0$), was examined by Balasubramaniam and Chai (1987), Haj-Hariri et al. (1990), and Nadim et al. (1990), still in the framework of perturbation techniques. In particular, Balasubramaniam and Chai (1987) extended the range of applicability of the solution of Young et al. (1959) under the constraint or requirement that the temperature field is in purely diffusive steady conditions (this occurs when $Pr \ll 1$ and Ma remains small, i.e., $Ma < 1$). They also analysed the shape of the droplet in the limit of $Pr \to 0$, showing that droplets of the same density as the matrix fluid do not deform, droplets less dense than the matrix fluid tend to deform oblately, and that droplets denser than the fluid matrix tend to elongate in the flow direction.

For similar conditions (i.e., when convective transport of heat is neglected) and small but finite Re (i.e., influence of inertia taken into account), Haj-Hariri et al. (1990) and Nadim et al. (1990) calculated the correction to the migration velocity caused by the shape deformation. It was found that droplets with densities higher/lower than the outside liquid deform to prolate/oblate spheroidal shapes at small values of the Capillary and Reynolds numbers. The corrections to the temperature field and the migration velocity of the droplet resulting from this deformation were obtained using the Lorentz reciprocal theorem. These authors illustrated that the migration velocity could increase, decrease, or remain unchanged according to the value of certain controlling parameters.

An analysis dealing with the asymptotic case of very high values of Re and Ma has been presented by Balasubramaniam and Subramanian (2000). They analysed the steady Marangoni migration of a spherical drop in a continuous phase under the idealised conditions ($Ma \to \infty$ and $Re \to \infty$), assuming that inertial terms in the momentum equation and convective-transport terms in the energy equation dominate over the corresponding molecular-transport terms. In

such a mathematical context (partially based on the earlier model by Harper and Moore, 1968), the migration velocity of the drop was obtained on the basis of a potential-flow theory, where the rate at which work is done by the thermocapillary stress was equated to the rate of viscous dissipation of energy. The method of matched asymptotic expansions was also employed to solve the conjugate heat-transfer problem in the two phases (characterised by the presence of thin thermal boundary layers both outside and within the drop). In physical terms it was found that in the limit of $Ma \to \infty$ the velocity of a drop becomes proportional to the square of the temperature gradient and the cube of the radius of the drop.

Finally, we mention the work of Jiménez-Fernández and Crespo (2002). The authors derived an analytical solution for the case of a non-deformable gas bubble surrounded by a viscoelastic Oldroy-B liquid undergoing motion under the effect of a constant temperature gradient. The solution was obtained in the framework of a perturbation approach under the assumption of negligible convective transport and weak viscoelastic effects. Their results showed that the bubble speed decreases quadratically for increasing values of the Deborah number.

More recently (essentially over the last two decades), the availability of powerful computers (including the possibility to resort to multi-processor computations) and the development of modern moving-boundary methods, such as the Volume of Fluid (VOF) or the level set (LS) techniques (see, e.g., Haj-Hariri et al. 1997, Rudman, 1998; Gueyffier et al. 1999; Sussman and Fatemi, 1999; Sussman and Puckett, 2000; Tryggvason et al. 2001 just to mention some initial efforts), has made possible addressing the problem directly in the framework of direct numerical discretisation and solution of the governing balance equations in the most general (time-dependent and non-linear) form. Along these lines, for instance, it is worth mentioning the works of Yin et al. (2008, 2012), Zhao et al. (2011), Brady et al. (2011), Balcázar et al. (2016), who performed parametric studies to examine the influence of typical non-dimensional numbers on the migrating process of both rigid and deformable drops. As a common finding, all these studies for finite values of Re and Ma highlighted that when convective transport is important, the internal circulation in the drop has a profound influence on the

temperature distribution in its vicinity and hence on its migration speed. More-over, thermal boundary layers can form in front of the droplet, and fluid-dynamic instabilities can develop when the value of the Marangoni number is sufficiently large.

In addition to the above mentioned strategies, it is also worth mentioning the recent developments of lattice Boltzmann methods (LBM, Liu et al. 2017, Liu and Zhang, 2015). Other techniques based on the phase-field method have been also demonstrated to be suitable for the simulation of the thermocapillary migration of droplets. In such a context, it is worth mentioning the work of Guo and Lin (2015) who have adopted the phase field method in conjunction with a novel approach based on a "non-classical" energy balance equation. Liu and Valocchi (2013) combined the capabilities of the lattice Boltzmann and phase field methods showing that such strategy can be successfully adopted for the simulation of thermocapillary flows. Similar approaches have also been used to study the motion of droplets under the influence of localised sources of heat (Liu et al. 2012 and 2013).

1.2   Motivation

The aim of this PhD research is to study the thermocapillary motion of a droplet in complex flow conditions, with the specific intent to: a) elucidate some aspects not yet fully understood related to the motion of the droplet in proximity of solid boundaries, b) investigate the role potentially played by the presence of a viscoelastic phase on both speed and morphological evolution of the drop interface. In both cases, negligible gravitational effects have been postulated.

Numerical simulations have been performed adopting a thermocapillary solver specifically developed in the scope of the present doctoral research activity. Ad-ditionally, in some cases, analytical solutions were obtained with the intent to provide additional insight into the physics involved on the problems and give a further proof of the accuracy of the numerical computations. Indeed, the ther-mocapillary motion of fluid particles is still a relatively unexplored subject, and

at the present stage there are several open questions to be addressed.

In experimental conditions, it is frequent to encounter complex geometries, where the droplet is subjected to large degrees of confinement (meant as the ratio between the diameter of the drop and a suitable characteristic length of the geometry), it is therefore important to understand how the motion of a droplet (or a bubble) can be altered by its proximity to the boundaries, or how a specific geometric configuration might affect the thermal field, which in turn might alter the droplet motion. Moreover, despite the relatively small thermal conductivities of the materials used for the fabrication of the test facilities for the experiments of the thermocapillary migration of drops, or for the fabrication of microfluidic chips (Polydimethylsiloxane (PDMS) and glass), the hypothesis of adiabaticity, which is usually adopted on the modelling of thermocapillary flows, might not be realistic and seems reasonable to account for the presence of thermal fluxes at the walls to properly describe the physics involved during the migration process. Motivated by the necessity to evaluate the impact of all these effects, an entire chapter of the present thesis (Chapter 4) is devoted to the study of the drop-walls interaction in the presence of both adiabatic and purely conductive walls. The role played by the domain shape on the migration process is also discussed at the end of the chapter.

Thus far, almost the entire body of literature available on the thermocapillary motion of droplets has been produced under the assumption of Newtonian phases. Indeed, all the examples discussed in the previous sections lie within this category. However, thermocapillary flows in the presence of non-Newtonian fluids have been already investigated for the past two decades (cf. the introductory section of Chapter 5 for a brief account about these works) and are still attracting the attention of the scientific community. Most of these works focus on fluid layers and it is only in the analytical work of Jiménez-Fernández and Crespo (2002) that non-Newtonian effects have been taken into account for the case of the thermocapillary motion of a gas bubble in a viscoelastic fluid. By contrast, there are several situations in which the coupling between viscoelasticity and thermocapillarity in the presence of dispersed phases, i.e., bubbles and drops, might be observed. Here

below we provide a brief account of some technological applications that can be relevant in this context.

It is well known that the thermal Marangoni phenomenon can be exploited to generate droplets on demand through the actuation of thermal instabilities by controlling the temperature of the ink nozzle (see Furlani et al. 2006). While inkjet fluids generally behave in a Newtonian manner in steady shear flows (Tuladhar snd Mackley, 2008), they can also exhibit viscoelastic effects in the working conditions established in printers, where the characteristic time scale of the flow is of the order of a millisecond or less (Vadillo et al. 2010). Additionally, it is worth emphasising the potential offered by microfluidic applications. In this cases in fact, it is not infrequent to encounter situations where the fluid involved can show a non-Newtonian behaviour. Moreover, the adoption of thermocapillary effects is widely used at the microscale for a variety of different purposes such as droplet actuation, mixing and sorting and bubble micro-oscillators (see, e.g., Karbalaei et al. 2016). Thus, it is reasonable to suppose that under such working conditions it is necessary taking into account for both viscoelastic and thermocapillary effects.

To enhance our understanding of the non-Newtonian problem, two chapters of this thesis are dedicated to the thermocapillary migration phenomenon in the presence of a viscoelastic fluid. The proposed problems are solved adopting both numerical and analytical techniques.

1.3   Thesis outline

With the exception of Chapter 1 and 2, which are intended to provide a general overview of the main subject and the theoretical background underlying the problems addressed in the subsequent discussions, the remaining body of the present manuscript includes original material that has already been published or is under preparation for submission.

In Chapter 2, the equation of motion for an isothermal incompressible flow are introduced in general form without considering any specific constitutive model. Subsequently, the Newtonian constitutive law and the viscoelastic models adopted

for the solution of the problems discussed in Chapters 5 and 6 are provided. The governing equations are firstly presented in dimensional form and subsequently reformulated in dimensionless terms. Finally, the numerical techniques adopted in the present work are then introduced and discussed in detail.

The subsequent Chapter 3, is dedicated to the implementation and validation of a solver for the numerical solution of non-isothermal interfacial flows. Firstly, a detailed description of the numerical strategies adopted for the implementation of the code is provided. Subsequently, the solver is tested against an analytical solution and well established experiments performed in microgravity conditions.

In Chapter 4, the interaction of the droplet with the boundaries of the domain and the influence of the domain configuration on the droplet migration process are investigated numerically. Firstly, we consider the situation in which the drop is forced to transit next to a single boundary. Then, the analysis is repeated by releasing the drop in proximity to a corner. Subsequently, the interaction problem with a single boundary is studied considering conductive boundary conditions. In the final section, the thermocapillary problem in the presence of converging and diverging channels is investigated and the results are compared with the calculations obtained for the straight geometry.

In Chapter 5, the role played by the presence of a viscoelastic continuous phase is investigated by means of a computational approach. Two different constant-viscosity viscoelastic models are used for different flow conditions. The Oldroyd-B model is adopted for relatively small values of the Deborah number, while the FENE-CR model is employed for higher values of this parameter. The simulations with the Oldroyd-B model are initially carried out considering an "infinitely dilute" polymer solutions. Then, the problem is analysed for the cases in which the concentration of polymer is not negligibly small (i.e., viscoelastic stress are effectively included) and a comparison between the two cases is provided. Finally, the problem is tackled for the case of moderately large values of the Deborah number adopting the FENE-CR model.

Finally, in Chapter 6, the viscoelastic problem is further investigated analytically by means of perturbation techniques in the limiting condition of small

Deborah numbers. Initially, we consider the case of a non-deformable (spherical) droplet, then, the calculation are performed assuming a deformable fluid particle. Finally, we report a detailed discussion of the results and compare them with the numerical calculations presented in Chapter 5.

In the last chapter of the thesis (Chapter 7), we summarise the main findings and provide guidelines for future works.

Chapter 2

Background: physical models and numerical methodology

2.1 Introduction

An overview of the thermal Marangoni phenomenon and a review of the relevant literature on droplet migration in this context has been presented in the previous chapter. It was clear from this discussion that the analytical solution of the governing equations is possible only in certain simplified flow conditions (as is indeed true for any other fluid-related problem). In this work, we adopt a theoretical/numerical methodology to study thermocapillary flows under a range of flow conditions, including effects of confinement (and other geometric effects such as the domain shape), as well as the presence of fluids that exhibit a non-Newtonian behaviour.

In this chapter, a formal mathematical description of the thermocapillary migration of fluid particles, which constitutes the leitmotiv of the current work, is given and discussed in detail in order to provide the fundamental theoretical background for a clear understanding of the problems addressed in subsequent chapters. Important dimensionless numbers are defined and the Newtonian and viscoelastic constitutive equations used to describe the fluid rheological behaviour considered in this thesis are presented and discussed. In the final section of this chapter, we review numerical techniques adopted for handling flows involving moving interfaces, focusing on methods based on a "single-fluid" approach, which are employed in the simulations of the present thesis.

2.2 Conservation laws for the flow of an isothermal incompressible fluid

We initially consider the isothermal flow of an incompressible fluid in which we suppose, without lack of generality, that gravity constitutes the only long range (body) force applied to the fluid elements. We will moreover assume the existence of contact (surface) forces exchanged between the boundaries of the fluid parcels. The motion can be described by applying the basic conservation laws (mass and linear momentum) expressed in differential form written for an infinitesimal fluid element (see e.g., Batchelor, 1967)

$$\nabla \cdot \mathbf{u} = 0 \tag{2.1}$$

$$\rho \frac{D\mathbf{u}}{Dt} = \rho \mathbf{g} + \nabla \cdot \mathbf{\Sigma} \tag{2.2}$$

Eq. (2.1) states that the net flux of mass of a fluid having constant density ρ flowing through the boundaries of a material element is zero, i.e., it simply represents the conservation of mass of an incompressible fluid particle having velocity $\mathbf{u}$. Eq. (2.2) represents the law of conservation of momentum and is known as Cauchy equation of motion. The operator $D(\cdot)/Dt = \partial(\cdot)/\partial t + \mathbf{u} \cdot \nabla(\cdot)$ is usually called material or substantial derivative and represents the rate of change of a generic variable expressed in an Eulerian (or spatial) frame of reference, measured by an observer "attached" to a particle of fixed identity moving with the local velocity $\mathbf{u}$. In this representation therefore, the acceleration $D\mathbf{u}/Dt$ accounts for the fact that in a certain region (control volume) the velocity can change both in time ($\partial\mathbf{u}/\partial t$) and space ($\mathbf{u} \cdot \nabla\mathbf{u}$) as the particle is advected by the flow. In the right hand side of (2.2) we have the gravitational force, $\rho\mathbf{g}$, and a symmetric tensor $\mathbf{\Sigma}$ (the symmetry can be verified by applying the equilibrium of an element to rigid rotations) which is called Cauchy stress tensor and represents the state of tension of the material element. At this stage the problem is still undetermined since we are in presence of nine variables (three velocity components and six independent components of the stress tensor), therefore in order to close it mathematically it

42

is necessary to include a constitutive equation that relates the state of stress of the fluid element with the local velocity.

In the following a detailed derivation of the Newtonian constitutive equation and other non-Newtonian constitutive models that are of interest for the present work will be presented.

2.3 Constitutive equations: Newtonian vs non-Newtonian behaviour

If a fluid is at rest, the only components of the stress tensor which are different from zero are the diagonal components, and the state of tension would be independent of the orientation. In other words, the stress is isotropic *viz.*, $\Sigma_{ij} = -p\delta_{ij}$, where δ_{ij} is the Kronecker delta (in this context the Einstein convention is adopted for convenience of notation) and p is the thermodynamic pressure. The minus sign is introduced to indicate that the normal stresses are considered positive if they are compressive (the normal at the interface of a fluid element is taken positive in the outward direction) and vice versa. A fluid in motion, on the other hand, produces additional stresses, τ_{ij}, and the total stress tensor is given by

$$\Sigma_{ij} = -p\delta_{ij} + \tau_{ij}. \tag{2.3}$$

It will be still assumed here that p is the thermodynamic pressure although this is not strictly correct, since now the fluid is not in thermodynamic equilibrium. Nevertheless, the departure from the condition of equilibrium is expected to be negligible if the relaxation time of the molecules (time required to adjust the microstructure of the fluid after a fluid element displacement) is small compared to the characteristic time of the flow. The deviatoric part of the stresses can be related to the rate-of-strain tensor $E_{ij} = 1/2\left(\partial u_i/\partial x_j + \partial u_j/\partial x_i\right)$ through a linear relationship, $\tau_{ij} = K_{ijmn}E_{mn}$, where K_{ijmn} is a fourth-order tensor constituted by 81 constant elements (see, e.g., Aris, 1962) that depends on the thermodynamic state of the fluid. The antisymmetric part of the velocity gradient, $\Omega_{ij} = 1/2\left(\partial u_i/\partial x_j - \partial u_j/\partial x_i\right)$ represents rigid rotations of the fluid elements

43

thus does not contribute to the stress. The expression for τ_{ij} given above, simply states that the each component of τ_{ij} is linearly related to the nine components of the rate-of-strain tensor E_{mn} through the coefficients of K_{ijmn}. Since the rate-of-strain tensor is symmetric, under the assumption of isotropic fluid and assuming that pure volumetric changes do not affect the stress (Stokes hypothesis), the well-known Newtonian constitutive equation is retrieved

$$\Sigma_{ij} = -p\delta_{ij} + 2\eta E_{ij} \tag{2.4}$$

Eq. (2.4) takes its name in honour of Isaac Newton who was the first to hypothesise that the force exchanged between two adjacent layers of fluid in relative motion is related to the velocity gradient orthogonal to the direction of the motion through a constant of proportionality, which he called "lack of slipperiness". Nonetheless, this result is actually due to George Gabriel Stokes, who derived it about two centuries after the publication of Newton's seminal work *Philosophiae Naturalis Principia Mathematica*.

Plugging Eq. (2.4) into Cauchy equation (2.2), the familiar Navier-Stokes equation for an incompressible fluid is retrieved

$$\rho\frac{D\mathbf{u}}{Dt} = -\nabla p + \rho\mathbf{g} + \eta\nabla^2\mathbf{u} \tag{2.5}$$

This equation takes its name after Stokes for his contribution, and the French scientist Claude-Luis Navier, who was the first to arrive to this form of the momentum equation in 1822.

"Fluids with featureless microstructures are well described by the Newtonian constitutive equation, which states that the stress tensor is proportional to the shear rate tensor. Fluids with complex microstructures (. . .) exhibit a wide variety of behaviours." In this quote from the book of Phan-Thien (Phan-Thien, 2002), it is implicitly stated that whenever we are in presence of fluids with non-trivial microscopic configurations, as for the case of colloidal suspension of rigid particles, emulsions and polymer solutions, for instance, the Newtonian constitutive law can be inadequate to describe the fluid behaviour. Indeed, often

more sophisticated models are required to describe the large variety of behaviours one would observe in complex fluid flows.

Newtonian fluids in isothermal conditions are characterised by two material properties, ρ and η. On the other hand, when we are interested on the description of non-Newtonian fluids, additional information might be required. In the Newtonian constitutive law, the viscosity is a constant that does not depend on the flow conditions, however there are many situations where this is not true. For example, in many polymeric fluids the viscosity decreases for increasing shear rates (shear-thinning behaviour) because as the shear rate increases the polymer molecules, which at rest are in a relaxed state, tend to align with the local flow field and offer less resistance to the motion. In other situations, the opposite behaviour is observed: further increments of the shear rate bring to increments of the shear viscosity. This shear-thickening effect is typical of colloidal suspensions of rigid particles heavily concentrated. The shear rate dependence of the viscosity can be modelled using a generalisation of the Newtonian constitutive law, therefore these fluids are usually termed "generalised Newtonian fluids". Another phenomenon frequently reported in suspensions is the presence of a "yield stress". In practice, below a certain stress threshold the material behaves as a solid, while above the critical stress a fluid-like behaviour is observed. This phenomenon is indeed very common and many substances that are very familiar to us, like mayonnaise, toothpaste and mud, for instance, exhibit a yield stress. These fluids are usually called viscoplastic or Bingham fluids. Another class of non-Newtonian fluids, that under opportune conditions exhibit both viscous and elastic behaviours (one may also say they possess "memory", since the elastic response of a material depends on its past stretching history) that are of great interest in many engineering and scientific applications, are viscoelastic fluids. Even without introducing their formal definition, it is clear that an appropriate constitutive model should include at least an additional material constant since the elastic response depends on the time history of the flow. However, this would be the simplest possible scenario. In practice, these fluids can exhibit a variety of other behaviours (such as those discussed before) in addition to the elastic response, and supplementary material

constants are often required to characterise their behaviour.

The subject of viscoelastic modelling is very broad and in continuous development. Providing a detailed description is beyond the scope of the current work and here we restrict our discussion to the description of the viscoelastic models that are of interest for the present thesis.

2.3.1 The Maxwell and the Oldroyd-B models

In Chapter 5 and 6 the thermocapillary motion of a Newtonian deformable droplet migrating through a viscoelastic Oldroyd-B fluid will be examined. In the present section we will provide the derivation and a brief account of the main features of this constitutive law which, despite its simplicity and limitations, still represents one of the most employed viscoelastic models.

The first attempt to derive a constitutive equation capable of describing the behaviour of materials showing both viscous and elastic properties is due to Maxwell, who believed that gases under certain condition might be viscoelastic. The underlying physical idea behind Maxwell's derivation consists on the superposition of the viscous (Newtonian) and elastic (Hookean) responses of a material in a single constitutive law. The interested reader is referred to Morrison (2001) or any other rheology textbooks for a detailed derivation. The model proposed by Maxwell reads (see e.g., Bird et al. Vol. 1, 1987)

$$\tau_{xy} + \frac{\eta}{G}\frac{\partial \tau_{xy}}{\partial t} = 2\eta E_{xy}, \tag{2.6}$$

where G is the elastic modulus of a purely elastic material, while the other quantities have the same meaning provided in the foregoing sections. Under appropriate limiting conditions the model correctly reproduce either the behaviour of a viscous (Newtonian) fluid, or the response of a linear elastic (Hookean) material. The viscous behaviour is obtained when the second term of the left hand side becomes negligible compared to the component of the stress. This condition can be obtained, for instance, when the material constant ratio $\lambda \equiv \eta/G$ (notice that this quantity has the dimension of a time) is very small. On the other hand,

46

when the term containing the partial time derivative becomes predominant, the Hookean behaviour is recovered. Despite its simplicity, the model proposed by Maxwell highlights some of the features typical of viscoelastic flows and provides the existence of a characteristic relaxation time, λ, that is ubiquitous in non-Newtonian fluid mechanics. However, its validity is restricted to those situations where the deformation of the fluid element is small due to the limitations imposed by the Hookean (linear) constitutive law. Additionally, it can be shown that in some circumstances it can predict a stress that depends on the particular frame of reference adopted (see, for instance, the "turntable experiment" discussed in Bird et al. Vol 1, 1987). This is indeed a serious limitation common to all those constitutive laws belonging to the class of "linear models", which drastically restrict its usefulness for flows of practical application.

The Maxwell model can be generalised in several ways. For instance, we can write Eq. (2.6) in a form valid for any arbitrary small fluid element displacement by replacing the stress component τ_{xy} with the stress tensor $\boldsymbol{\tau}$

$$\boldsymbol{\tau} + \lambda \frac{\partial \boldsymbol{\tau}}{\partial t} = \eta_0 \mathbf{D} \tag{2.7}$$

where $\mathbf{D} \equiv 2\mathbf{E}$ and η_0 is the zero shear viscosity (*viz.*, the viscosity in the limiting condition of vanishingly small shear rates). This latter quantity has been used in place of the usual definition of viscosity to highlight the fact that in non-Newtonian fluid mechanics the viscosity is in general a variable rather than a constant.

Starting from Eq. (2.7), one can imagine to include other material constants to obtain alternative generalisations. A variant of Eq. (2.7) was proposed by Jeffreys for the study of wave propagation on earth's mantle (Jeffreys, 1929)

$$\boldsymbol{\tau} + \lambda \frac{\partial \boldsymbol{\tau}}{\partial t} = \eta_0 \left(\mathbf{D} + \lambda_r \frac{\partial \mathbf{D}}{\partial t} \right). \tag{2.8}$$

The additional material constant, λ_r, included in Eq. (2.8) represents what is usually called "retardation time": its value is not arbitrary, but is related to the relaxation time with the following restriction $\lambda > \lambda_r$. Other generalisations are

possible but will not be discussed here.

At this point we have all the elements necessary to introduce the Oldroyd-B model. During the description of the Maxwell constitutive law it has been mentioned that linear models might not be frame of reference-invariant in some particular conditions. This issue arises the necessity to build more general constitutive equations capable to describe any arbitrary flow irrespective of the particular reference system adopted. In fact, all the constitutive models should be invariant with respect to rigid body motion of the spatial frame of reference (principle of "objectivity"). The basic mathematical foundation required to build models that respect the principle of objectivity is due to Oldroyd (Oldroyd, 1950), who set out the basis to write the constitutive equations in a frame invariance form adopting coordinate systems advected with the material element. It is possible to show then (see e.g., Chapter 9 of Bird et al. 1987) that a possible frame invariant form of the Jeffreys model given in Eq. (2.8) is readily obtained by substituting the partial time derivatives with the so-called "upper-convected" derivative. We have then

$$\boldsymbol{\tau} + \lambda \hat{d}\boldsymbol{\tau} = \eta_0 \left(\mathbf{D} + \lambda_r \hat{d}\mathbf{D} \right), \tag{2.9}$$

where

$$\hat{d}\left(\cdot\right) = \left(\frac{\partial}{\partial t} + \mathbf{u} \cdot \nabla \right)(\cdot) - \left\{ \nabla \mathbf{u}^{\mathrm{T}} \cdot (\cdot) + (\cdot) \cdot \nabla \mathbf{u} \right\} \tag{2.10}$$

is the upper-convected derivative operator. Eq. (2.9) is known in the literature as upper-convected Jeffreys model or Oldroyd-B model, who was the first to write it in this form (Oldroyd, 1950). When $\lambda_r = 0$, Eq. (2.9) yields the upper-convected form of the Maxwell model (UCM) seen before.

With some mathematical manipulations we can split the stress tensor into the sum of a Newtonian (solvent) contribution, and a viscoelastic (polymer) contri-

bution, $\boldsymbol{\tau} = \boldsymbol{\tau}_s + \boldsymbol{\tau}_p$, which allows us to re-write Eq. (2.9) as

$$\boldsymbol{\tau}_s = \eta_s \mathbf{D} \tag{2.11}$$

$$\boldsymbol{\tau}_p + \lambda \hat{d} \boldsymbol{\tau}_p = \eta_p \mathbf{D} \tag{2.12}$$

having introduced the solvent and polymer viscosities (notice that although it is not infrequent to encounter viscoelastic fluids that are not polymeric solutions, the common practice is to refer to a polymer viscosity meant as an additional contribution to the viscosity to be attributed to the presence of elastic microstructures dispersed into the Newtonian solvent), η_s and η_p defined such that $\eta_0 = \eta_s + \eta_p = \beta\eta_0 + (1 - \beta)\eta_0$, where $\beta = \eta_s/\eta_0$. In the subsequent chapters we shall make use of this latter parameter or we will adopt, alternatively, the quantity $c = 1 - \beta = \eta_p/\eta_0$, which provides a measure of the concentration of polymers dispersed into the solution, depending on the convenience of the case discussed.

It is possible to show that the present model is able to capture several features typical of Boger fluids, *viz.*, viscoelastic fluids having (nearly) constant shear viscosity (see e.g., Bird et al. 1987 or Phan-Thien, 2002). For instance, in the steady-state simple shear flow, the Oldroyd-B model predicts a first normal stress difference, $N_1 = \tau_{yy} - \tau_{xx}$, that is quadratic with the shear rate and a zero second normal stress difference, $N_2 = \tau_{yy} - \tau_{zz}$; while in unsteady shear flows, the model predict stresses that increase monotonically in time to their steady values without stress overshoot. As a major drawback, in the extensional flow it predicts an elongational viscosity (see below for a definition of this quantity) that becomes infinite for the finite elongational rate of $\dot{\varepsilon} = 1/2\lambda$, as it is shown in the following example.

Let us consider the start-up of a purely elongational flow defined in the following manner

$$\nabla \mathbf{u} = \text{diag}\left\{\dot{\varepsilon}, -1/2\dot{\varepsilon}, -1/2\dot{\varepsilon}\right\}, \tag{2.13}$$

having used the notation "diag" to indicate that the off-diagonal element of the

velocity gradient are zero. Using Eq. (2.12) we can find (cf. Phan-Thien, 2002)

$$\tau_{p,xx} + \lambda \left(\dot{\tau}_{p,xx} - 2\dot{\varepsilon}\tau_{p,xx} \right) = 2\eta_p \dot{\varepsilon}, \tag{2.14}$$

$$\tau_{p,yy} + \lambda \left(\dot{\tau}_{p,yy} + \dot{\varepsilon}\dot{\tau}_{p,yy} \right) = -\eta_p \dot{\varepsilon}, \tag{2.15}$$

that can be easily integrated to find

$$\tau_{p,xx} = \frac{2\eta_p \dot{\varepsilon}}{1 - 2\lambda\dot{\varepsilon}} \left(1 - e^{-(1-2\lambda\dot{\varepsilon})t/\lambda} \right), \tag{2.16}$$

$$\tau_{p,yy} = \tau_{p,zz} = -\frac{2\eta_p \dot{\varepsilon}}{1 + \lambda\dot{\varepsilon}} \left(1 - e^{-(1+\lambda\dot{\varepsilon})t/\lambda} \right). \tag{2.17}$$

We notice then, if either $\lambda\dot{\varepsilon} \geq 1/2$ or $\lambda\dot{\varepsilon} \leq -1$, one of the two components of the stress grows unboundedly. The extensional viscosity is given by

$$\eta_{ext} = \frac{\tau_{xx} - \tau_{yy}}{\dot{\varepsilon}} = 3\eta_s + \frac{3\eta_p}{(1 - 2\lambda\dot{\varepsilon})(1 + \lambda\dot{\varepsilon})} \tag{2.18}$$

which shows the presence of the singularity mentioned before.

The Oldroyd-B model is often used to evaluate the role of elasticity without introducing any complication related to the presence of shear dependent viscosity effects. However its use is limited for relatively small values of the relaxation time, imposing a severe restriction on the range of viscoelastic regimes that can be explored

A possible way to partially overcome such limitation consists on the adoption of a more realistic model for the polymer filament, which can be obtained, for instance, by limiting its maximum elongation, as in the class of models known as Finite Extensible Non-linear Elastic models (FENE).

2.3.2   The FENE-CR model

Before starting the description of the FENE-CR model (Chilcott and Rallison, 1988), it is advisable to rewrite the Oldroyd-B model in terms of a tensor quantity, **A**, usually termed conformation (or configuration) tensor.

All the models discussed so far have been derived on the basis of a continuum

approach without making any assumption about the actual microstructure of the fluid. By contrast, the viscoelastic character is conferred to the fluid by the presence of complex elastic structures (that might be in the form of small fluid particles, as for the case of an emulsion, or long polymer chains, as in polymeric solutions) that undergo deformation in relation to the stretch history of the region of fluid in which they are placed in. Appears clear, thus, the necessity to approach viscoelastic modelling adopting a more physically sound methodology, which can take into account the actual microstructure of the fluid even if with some degree of approximation. For such reason, in the past years the role of statistical mechanics became increasingly more preponderant in the discipline of "modelling" viscoelastic fluids.

When we consider a viscoelastic fluid in the sense depicted before, the simplest model that can be used to describe an elastic microelement subjected to the viscous drag of a Newtonian fluid is composed of two identical spheres of mass m connected by a massless linear spring (dumbbell). The conformation tensor can be defined then as the ensemble average of the dyadic product of the radius of gyration, $\mathbf{r}$, (end-to-end vector connecting the two extremities of the dumbbell) of the polymer chain, $\mathbf{A} = \langle \mathbf{rr} \rangle$. Adopting this alternative representation, it is possible to demonstrate (see, for instance Oliveira, 2009) that the following equation

$$\lambda \hat{d} \mathbf{A} = - (\mathbf{A} - \mathbf{I}) \tag{2.19}$$

is equivalent to expression (2.12). The tensor, $\mathbf{I}$, represent the identity tensor, and the "relaxed" configuration for the polymer molecules is represented the condition $\mathbf{A} = \mathbf{I}$. The polymer stress tensor can be retrieved then using the following expression due to Kramers (1946)

$$\boldsymbol{\tau}_p = \frac{\eta_p}{\lambda} (\mathbf{A} - \mathbf{I}). \tag{2.20}$$

The idea of Chilcott and Rallison (1988) was to reformulate the law expressed by Eq. (2.19) by adopting a force model in which the spring maximum elongation

51

was effectively bounded. The proposed model was

$$\lambda \hat{d} \mathbf{A} = -f\left(\operatorname{tr}\left(\mathbf{A}\right)\right)\left(\mathbf{A} - \mathbf{I}\right) \tag{2.21}$$

where $f\left(\operatorname{tr}\left(\mathbf{A}\right)\right) = L^2/(L^2 - \operatorname{tr}\left(\mathbf{A}\right))$ and L^2 represents a quantity called extensibility parameter, which accounts for the actual maximum elongation that the spring can undergo. When $f\left(\operatorname{tr}\left(\mathbf{A}\right)\right) = 1$ (notice that $\operatorname{tr}\left(\mathbf{A}\right)$ can be seen as a measure of the deformation of the dumbbell), which corresponds to an infinite extensibility of the polymer molecule ($L^2 \to \infty$), the Oldroyd-B model is recovered.

Whenever we aim to study a flow that shows elongational behaviour (even locally, as for the cases of the moving droplet considered in Chapter 5 and 6), the FENE-CR model allows the investigation of a wider range of relaxation times when compared to the Oldroyd-B model.

Table 2.1 summarises the models discussed so far. Linear models can be retrieved by replacing the upper-convected derivative with the time partial derivative.

Table 2.1: Constitutive equations for the viscoelastic fluids discussed in the present Section. The Newtonian constitutive equation has also been included for completeness.

Model	Material constants	Constitutive equations
Newtonian	η_0	$\boldsymbol{\tau} = \eta_0 \mathbf{D}$
UCM	η_0, λ	$\boldsymbol{\tau} + \lambda \hat{d}\boldsymbol{\tau} = \eta_0 \mathbf{D}$
Oldroyd-B	η_s, η_p, λ	$\boldsymbol{\tau}_s = \eta_s \mathbf{D}$ $\boldsymbol{\tau}_p + \lambda \hat{d}\boldsymbol{\tau}_p = \eta_p \mathbf{D}$
FENE-CR	$\eta_s, \eta_p, \lambda, L^2$	$\boldsymbol{\tau}_s = \eta_s \mathbf{D}$ $\lambda \hat{d}\mathbf{A} = -\frac{L^2}{L^2 - \operatorname{tr}(\mathbf{A})}\left(\mathbf{A} - \mathbf{I}\right)$ $\boldsymbol{\tau}_p = \frac{\eta_p}{\lambda}\left(\mathbf{A} - \mathbf{I}\right)$

2.4 Governing equations for thermocapillary flows in the presence of two immiscible phases

To introduce the complete set of equation required for the description of the motion of fluid particles in non-isothermal conditions, let us consider a flow system constituted by two incompressible isotropic, homogeneous, immiscible viscoelastic fluids. We postulate the presence of a thermal gradient that, at least in one point, has a component tangential to the interface (it is worthwhile to emphasise that only surface (or tangential) interfacial tension gradients are allowed, therefore in order to produce thermocapillary motion, tangential temperature differences must exist). Additionally, we assume the absence of gravity and any other long-distance force. The motion of such system is then described by the following set of conservation (mass, momentum and energy, in the order reported below) equations

$$\nabla \cdot \mathbf{u} = 0 \tag{2.22}$$

$$\rho \frac{D\mathbf{u}}{Dt} = -\nabla p + \nabla \cdot \boldsymbol{\tau} \tag{2.23}$$

$$\rho c_p \frac{DT}{Dt} = \kappa \nabla^2 T \tag{2.24}$$

for one phase, where T represents the absolute temperature, and

$$\nabla \cdot \tilde{\mathbf{u}} = 0 \tag{2.25}$$

$$\tilde{\rho} \frac{D\tilde{\mathbf{u}}}{Dt} = -\nabla \tilde{p} + \tilde{\eta} \nabla \cdot \tilde{\boldsymbol{\tau}} \tag{2.26}$$

$$\tilde{\rho} \tilde{c}_p \frac{D\widetilde{T}}{Dt} = \tilde{\kappa} \nabla^2 \widetilde{T}. \tag{2.27}$$

for the other fluid, having adopted a "tilde" to underline the fact that variables and material quantities are different from one phase to the other. The material parameters appearing in the energy equations (Eqs. 2.24 and 2.27) are the heat capacity, c_p, and thermal conductivity, κ. These two equations have been written upon the hypothesis that the fluids obey Fourier's law of thermal conduction,

$\mathbf{q} = -\kappa \nabla T$, where $\mathbf{q}$ is the local heat flux density. Under the hypothesis of homogeneous and isotropic fluids, the thermal conductivity, κ, is a scalar that is constant on each phase. In general, however, fluids might be non-homogeneous and/or non-isotropic, hence the conductivity should be represented by a rank 2 tensor in which any component is a function of the position rather than a constant. In viscoelastic fluids, for instance, the internal microstructure might assume "preferential" directions upon the effect of local deformations, and the hypothesis of isotropicity and homogeneity might not be realistic. Nevertheless, for the sake of simplicity, in the following we shall assume that the thermal conductivity is uniform everywhere within each phase.

To characterise the system completely, it is necessary to include a viscoelastic model for each phase (in the present discussion we refer to the Oldroyd-B model given by Eq. 2.9, but in principle any other model can be adopted)

$$\boldsymbol{\tau} + \lambda \hat{d} \boldsymbol{\tau} = \eta_0 \left(\mathbf{D} + \lambda_r \hat{d} \mathbf{D} \right) \tag{2.28}$$

$$\tilde{\boldsymbol{\tau}} + \tilde{\lambda} \hat{d} \tilde{\boldsymbol{\tau}} = \tilde{\eta}_0 \left(\widetilde{\mathbf{D}} + \tilde{\lambda}_r \hat{d} \widetilde{\mathbf{D}} \right) \tag{2.29}$$

and a law that relates the interfacial tension to the temperature. In most of the cases, this variation is negative (regions of the interface at higher temperature are characterised by lower values of the interfacial tension, see, e.g., Subramanian and Balasubramanian, 2001), *viz.*, $\sigma_T = \partial \sigma / \partial T < 0$. Additionally, the problem requires the definition of interfacial boundary conditions. The fluid interface is a two-dimensional entity defined in a three-dimensional region of space, thus it can be represented by the following implicit equation

$$F\left(\mathbf{x}, t\right) = 0 \tag{2.30}$$

where $\mathbf{x}$ is the position vector. Then, if we assume absence of mass exchange between the two phases, each fluid particle that lies at the interface at a certain instant will remain on it as the flow evolves in time. In other terms, the material

derivative of Eq. (2.30) must be zero, *viz.*

$$\frac{\partial F(\mathbf{x}, t)}{\partial t} + \mathbf{u} \cdot \nabla [F(\mathbf{x}, t)] = 0. \tag{2.31}$$

From the above equation we can then define the unit normal at the interface (we assume positive the vector pointing from the phase designed with a tilde toward the other one) as

$$\mathbf{n} = \frac{\nabla F}{|\nabla F|}. \tag{2.32}$$

Then, with the aid of this definition, from Eq. (2.31) we obtain

$$\mathbf{u} \cdot \mathbf{n} = \tilde{\mathbf{u}} \cdot \mathbf{n} = -\frac{1}{|\nabla F|} \frac{\partial F}{\partial t} \tag{2.33}$$

which represents a kinematic condition for the normal component of the velocity at the interface. If the fluid surface does not evolve in time, Eq. (2.33) finally becomes

$$\mathbf{u} \cdot \mathbf{n} = \tilde{\mathbf{u}} \cdot \mathbf{n} = 0. \tag{2.34}$$

which states that for steady state flows, the two normal components of the velocity at the interface must be zero. Additionally, we need to prescribe another kinematic condition for the tangential velocity. In this case, it is common practice to postulate shear-free conditions, i.e., assume that the tangential velocities inside and outside the drop are equal (Hadamard, 1911, Rybczynski, 1911), thus we have

$$\mathbf{u} \cdot \mathbf{t} = \tilde{\mathbf{u}} \cdot \mathbf{t} \tag{2.35}$$

where $\mathbf{t}$ is the tangent vector at the interface.

Since the above results does not specify the velocity itself, but rather relate the field on both sides of the interface, we need to introduce additional conditions. On the basis of physical considerations we observe that the stresses at the interface

must be discontinuous due to the presence of capillary tension. Recalling the definition of total stress given in Sect. 2.2, $\boldsymbol{\Sigma} = -p\mathbf{I} + \boldsymbol{\tau}$, the stress jump condition is then given by

$$\mathbf{n} \cdot \left(\boldsymbol{\Sigma} - \widetilde{\boldsymbol{\Sigma}} \right) = \sigma \mathbf{n} \left(\nabla \cdot \mathbf{n} \right) - \nabla_S \left(\sigma \right) \tag{2.36}$$

where the two terms in the right hand side represent the capillary and thermocapillary force, respectively and $\nabla_S = \nabla - \mathbf{n} \left(\mathbf{n} \cdot \nabla \right)$ is the surface gradient operator. Projecting expression (2.36) along the normal and tangential direction, we obtain the normal and tangential stress balance, respectively

$$\tilde{p} - p + \mathbf{n} \cdot \left(\boldsymbol{\tau} - \tilde{\boldsymbol{\tau}} \right) \cdot \mathbf{n} = \sigma \left(\nabla \cdot \mathbf{n} \right) \tag{2.37}$$

$$\left[\mathbf{n} \cdot \left(\boldsymbol{\tau} - \tilde{\boldsymbol{\tau}} \right) \right] \cdot \mathbf{t} = -\nabla_S \left(\sigma \right) \cdot \mathbf{t} \tag{2.38}$$

It is worth to notice that the balance (2.37) can be satisfied either in the presence or not of fluid motion, since the capillary force can be balanced only by the pressure difference between the two phases if the fluid is at rest. On the contrary, in presence of tangential interfacial tension gradients, Eq. (2.38) clearly shows that a flow at the interface must exist. Assuming that σ varies only with temperature (i.e., we are excluding the presence of any other effect that might cause surface tension gradients), upon the hypothesis that its rate of change is constant the latter stress balance condition becomes

$$\left[\mathbf{n} \cdot \left(\boldsymbol{\tau} - \tilde{\boldsymbol{\tau}} \right) \right] \cdot \mathbf{t} = -\sigma_T \nabla_S T \tag{2.39}$$

Additionally to the kinematic and stress conditions defined before, we need to prescribe boundary conditions for the temperature field. Assuming that no phase changes are allowed, the following equations must be satisfied at each point of

the interface

$$T = \widetilde{T} \tag{2.40}$$

$$\mathbf{n} \cdot \mathbf{q} = \mathbf{n} \cdot \tilde{\mathbf{q}} \tag{2.41}$$

where $\mathbf{q}$ is represented by the above mentioned Fourier's law, $\mathbf{q} = -\kappa \nabla T$, thus Eq. 2.41 yields

$$\mathbf{n} \cdot \kappa \nabla T = \mathbf{n} \cdot \tilde{\kappa} \nabla \widetilde{T} \tag{2.42}$$

In addition to the previous condition at the interface, closure of the mathematical problem requires the adoption of supplementary boundary conditions to be specified on the basis of the specific problem adopted (i.e., presence of solid boundaries or not, presence of possible symmetries, etc.). Due to the generic nature of the present discussion, these supplementary boundary conditions will be not introduced at this stage, but will be introduced in the subsequent chapters where the particular problems to be addressed are fully defined.

At this stage it is useful to introduce the nondimensional form of the governing equations to show their dependence on the dimensionless parameters adopted for the study of thermocapillary flows. For such a purpose, it is convenient to refer to the specific problem introduced below.

Let us consider the flow sketched in Fig. 2.1, where a spherical fluid particle of radius R translates in the upward direction driven by thermocapillary forces generated by a constant temperature gradient, $\nabla_\infty T$. We choose the radius of the drop, R, as the reference length and define the reference velocity, $U_T = -\sigma_T R \nabla_\infty T / \eta_0$, having assumed that the thermocapillary stresses at the interface generates velocity gradients having order of magnitude U_T/R. The stresses, including pressure, are nondimensionalised with the characteristic viscous stress, $\eta_0 U_T / R$. The temperature is made dimensionless by subtracting to its value the initial undisturbed temperature at infinity taken in the plane normal to the direction of the mean motion passing through the centre of the drop, and dividing it by the scaling temperature, $R \nabla_\infty T$. Finally, time is scaled with the

57
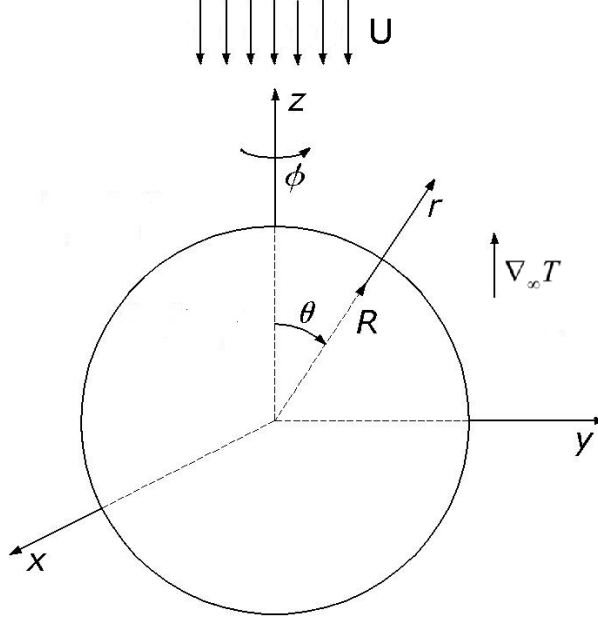
Figure 2.1: Schematic of a droplet moving in the upward direction, including the Cartesian and the spherical frame of references attached to its centre. Note that, coherently with the choice of the frame of references, the far-field flow appears directed downward.

characteristic convective time, R/U_T. Using these scaling laws, we obtain the following dimensionless form of the governing equations (mass is momentarily excluded for the sake of brevity, since no dimensionless parameters will appear on its equation) in the continuous phase are (notice that for the sake of simplicity we have represented dimensionless quantities with the same symbols adopted for the dimensioned ones)

$$\frac{D\mathbf{u}}{Dt} = -\frac{\eta_0}{\rho R U_T} \nabla p + \frac{\eta_0}{\rho R U_T} \nabla \cdot \boldsymbol{\tau} \tag{2.43}$$

$$\frac{DT}{Dt} = \frac{\kappa}{\rho c_p R U_T} \nabla^2 T \tag{2.44}$$

$$\boldsymbol{\tau} + \frac{\lambda U_T}{R} \hat{d}\boldsymbol{\tau} = \mathbf{D} + \frac{\lambda_r U_T}{R} \hat{d}\mathbf{D} \tag{2.45}$$

while in the dispersed phase are given by

$$\frac{D\tilde{\mathbf{u}}}{Dt} = -\frac{\rho}{\tilde{\rho}}\frac{\eta_0}{R\rho U_T}\nabla p + \frac{\rho}{\tilde{\rho}}\frac{\eta_0}{R\rho U_T}\nabla \cdot \tilde{\boldsymbol{\tau}} \tag{2.46}$$

$$\frac{D\tilde{T}}{Dt} = \frac{\rho c_p}{\kappa}\frac{\tilde{\kappa}}{\tilde{\rho}\tilde{c}_p}\frac{\kappa}{\rho c_p R U_T}\nabla^2 \tilde{T} \tag{2.47}$$

$$\tilde{\boldsymbol{\tau}} + \frac{\tilde{\lambda}}{\lambda}\frac{\lambda U_T}{R}\hat{d}\tilde{\boldsymbol{\tau}} = \frac{\tilde{\eta}_0}{\eta_0}\widetilde{\mathbf{D}} + \frac{\tilde{\eta}_0}{\eta_0}\frac{\tilde{\lambda}_r}{\lambda_r}\frac{\lambda_r}{\lambda}\frac{\lambda U_T}{R}\hat{d}\widetilde{\mathbf{D}} \tag{2.48}$$

Finally, the dimensionless form of the interfacial stress conditions are provided by

$$\tilde{p} - p + \mathbf{n} \cdot (\boldsymbol{\tau} - \tilde{\boldsymbol{\tau}}) \cdot \mathbf{n} = \frac{\sigma}{\eta_0 U_T}(\nabla \cdot \mathbf{n}) \tag{2.49}$$

$$\mathbf{n} \cdot (\boldsymbol{\tau} - \tilde{\boldsymbol{\tau}}) \cdot \mathbf{t} = \nabla_S T \cdot \mathbf{t} \tag{2.50}$$

Now, we can introduce the following set of dimensionless parameters. The first group reported below is the Reynolds number, which compares the relative extent of inertia respect to the magnitude of viscous forces. Here the Reynolds number is defined as

$$Re = \frac{\rho R U_T}{\eta_0}. \tag{2.51}$$

This group, which is arguably the most important number used in fluid mechanics, takes its name after the work of the British engineer Osborne Reynolds, who introduced it to quantify the results of his studies about the transition from laminar to turbulent regime in pipes.

The Marangoni number, which is named after the contribution of the Italian physicist Carlo Marangoni here is defined as

$$Ma = \frac{\rho c_p R U_T}{\kappa}. \tag{2.52}$$

This parameter gives a measure of the relative importance of convective transport of energy relative to its molecular counterpart (thermal diffusion). It can be seen as a special case of the Peclet number, $Pe = \rho c_p R U / \kappa$, when the characteristic

velocity of the flow is taken as $U = U_T$.

The Capillary number, which compares the importance of viscous effects relative to the interfacial tension force is defined as

$$Ca = \frac{\eta_0 U_T}{\sigma}. \tag{2.53}$$

Finally, we introduced a parameter that has been called "thermal" Deborah number (later on simply referred as Deborah number) defined as

$$De_T = \frac{\lambda U_T}{R}. \tag{2.54}$$

This group represents the ratio between the relaxation time of the fluid and the characteristic time of thermal convection, providing a measure of the unsteadyness introduced by viscoelasticity. The Deborah number takes its name from a verse of the Bible, stating: "The mountains flowed before the Lord" in a song sang by the prophet Deborah (Reiner, 1964). This definition emphasises the fact that, if the period of observation of a phenomenon is sufficiently high, even materials that are usually termed as solids, can flow. The adoption of this quantity instead of the usual Deborah number, which is generally defined considering the droplet migration speed, U, as a scaling velocity is twofold. On the first hand, it allows the dimensionless description of the problem in a "conventional" way, since for thermocapillary problems the Reynolds and Marangoni numbers are usually defined in the manner reported above, and on the other one, as it will be clear in Chapter 6, the non-Newtonian correction to the migration velocity will depend on the Deborah number, thus the adoption of U as a scaling velocity would provide an implicit representation of the droplet velocity. Contrarily, the adoption of U_T will avoid such complication.

Using these results, the dimensionless form of the governing equations and

constitutive law become

$$\nabla \cdot \mathbf{u} = 0 \tag{2.55}$$

$$Re\frac{D\mathbf{u}}{Dt} = -\nabla p + \nabla \cdot \boldsymbol{\tau} \tag{2.56}$$

$$Ma\frac{DT}{Dt} = \nabla^2 T \tag{2.57}$$

$$\boldsymbol{\tau} + De_T \hat{d}\boldsymbol{\tau} = \mathbf{D} + \beta De_T \hat{d}\mathbf{D} \tag{2.58}$$

for the continuous phase, and

$$\nabla \cdot \tilde{\mathbf{u}} = 0 \tag{2.59}$$

$$\delta Re\frac{D\tilde{\mathbf{u}}}{Dt} = -\nabla \tilde{p} + \alpha \nabla \cdot \tilde{\boldsymbol{\tau}} \tag{2.60}$$

$$Ma\frac{D\widetilde{T}}{Dt} = \alpha_{th}\nabla^2 \widetilde{T} \tag{2.61}$$

$$\tilde{\boldsymbol{\tau}} + \nu De_T \hat{d}\tilde{\boldsymbol{\tau}} = \alpha \left(\widetilde{\mathbf{D}} + \nu_r \beta De_T \hat{d}\widetilde{\mathbf{D}} \right) \tag{2.62}$$

for the dispersed phase. The additional parameters appearing in Eqs 2.59, 2.62 are the density ratio, $\delta = \tilde{\rho}/\rho$, the viscosity ratio, $\alpha = \tilde{\eta}_0/\eta_0$, the ratio between the two thermal diffusivities, $\alpha_{th} = (\tilde{\kappa}/\tilde{\rho}\tilde{c}_p)/(\kappa/\rho c_p)$ and the ratios of relaxation time and of retardation time, $\nu = \tilde{\lambda}/\lambda$ and $\nu_r = \tilde{\lambda}_r/\lambda_r$, respectively. We notice that the Capillary number does not appear explicitly into the governing equations listed above. We notice in fact that this group arises into the dimensionless form of the normal stress condition (Eq. 2.63), as well as in the momentum balance when we will adopt the so-called "one-fluid" formulation (cf. Sect. 2.5.1 and Sect. 3.2)

$$\tilde{p} - p + \mathbf{n} \cdot (\boldsymbol{\tau} - \tilde{\boldsymbol{\tau}}) \cdot \mathbf{n} = \frac{1}{Ca}(\nabla \cdot \mathbf{n}) \tag{2.63}$$

$$\mathbf{n} \cdot (\boldsymbol{\tau} - \tilde{\boldsymbol{\tau}}) \cdot \mathbf{t} = \nabla_S T \cdot \mathbf{t} \tag{2.64}$$

The general solution of the system of equations (2.22-2.29) (or equivalently, 2.55-2.62) with the addition of the required boundary conditions is not available for any arbitrary flow. Nevertheless, in some limiting conditions it is actually

possible to derive analytical solutions which, in spite of their "simplified character", provide insightful information about the physics involved in more general situations. For these reasons, during the past years a significant amount of effort has been dedicated to the derivation of analytical solutions for these type of flows. A thorough collection of these problems can be found in the book of Subramanian and Balasubramanian (2001). In the subsequent section the discussion will be limited to the simplest possible case (i.e., for Newtonian flows in the absence of convective transport) for the obvious reason that it is the most suitable for an introduction to the problem and also because it will be constantly used for reference throughout the next chapters. Also, in the presentation of the numerical methods introduced in Sect. 2.5, for the sake of simplicity, viscoelastic effects will not be considered in the discussion. The specific methodology adopted for their numerical characterisation will be introduced later in Chapter 5.

2.4.1 The analytical solution of Young, Goldstein and Block

Let us consider the flow depicted in Fig. 2.1. Under the following assumptions:

- Newtonian fluids;
- Steady-state conditions;
- Absence of convective transport (both in terms of momentum and energy);
- Constant material properties (i.e., indifferent to temperature variations);
- Constant rate of change of the interfacial tension with the temperature, i.e., $\sigma_T = \text{const}$;

it is possible to obtain a solution in "closed-form" of the governing equations in a relatively straightforward manner. The problem was originally solved by Young et al., (1959) and a detailed derivation will be provided in Chapter 6. In the following we will limit ourselves to show the main result and discuss some of the characteristic features of the flow.

It can be shown that in the absence of gravity, the steady-state velocity of the droplet is given by (it is worth to mention the presence of a typo in the original paper of Young at al. (1959), thus the reader is referred, for instance, to

Subramanian and Balasubramanian, 2001 for the correct expression of the result)

$$U_{YGB} = \frac{2\left(-\sigma_T\right)R\nabla_\infty T/\eta}{\left(2 + 3\tilde{\eta}/\eta\right)\left(2 + \tilde{\kappa}/\kappa\right)} \tag{2.65}$$

where the subscript YGB stands for the names of the authors who derived the above equation. From an inspection of Eq. (2.55) we can infer that the droplet speed is a linear increasing function of the drop radius, of the temperature gradient as well as of the interfacial tension variation coefficient. On the contrary, the droplet speed decreases when the viscosity of the continuous phase is increased. Moreover, when the drop viscosity tends to infinity, which resembles the case of a hard sphere, the speed correctly tends to zero. In the opposite scenario, i.e., when $\tilde{\eta}$ approaches zero, the fluid particle behaves as a gas bubble and the velocity is maximised. The only condition where the model fails to predict the drop velocity is when the continuous phase viscosity approaches zero. In this case the drop should not move at all because the hydrodynamic force on the drop is proportional to $\eta \rightarrow 0$, and the droplet would not experience any force from the surrounding fluid regardless of the motion that might be present at the interface and inside the drop. To see this from another perspective, the viscous stresses generated inside the drop are actually internal forces (per unit surface) of the system meant as a whole (drop and surrounding fluid) which cannot actually contribute to variation of linear momentum in a global sense. It is indeed puzzling that despite the rigorous physical and mathematical formulation, the solution seems to violate one of the conservation laws that constitutes the basis for its derivation.

Understanding the role played by the thermal conductivity is a bit more involved to grasp. In the simplest scenario of equal thermal conductivities, one realises that the temperature profile is everywhere linear. In fact, since the absence of convection has been postulated, the thermal field at the interface will develop coherently with the actual value of the thermal conductivity ratio between the two phases regardless the velocity field established in the region of the drop. Thus, when the two fluids have the same thermal conductivity, the temper-
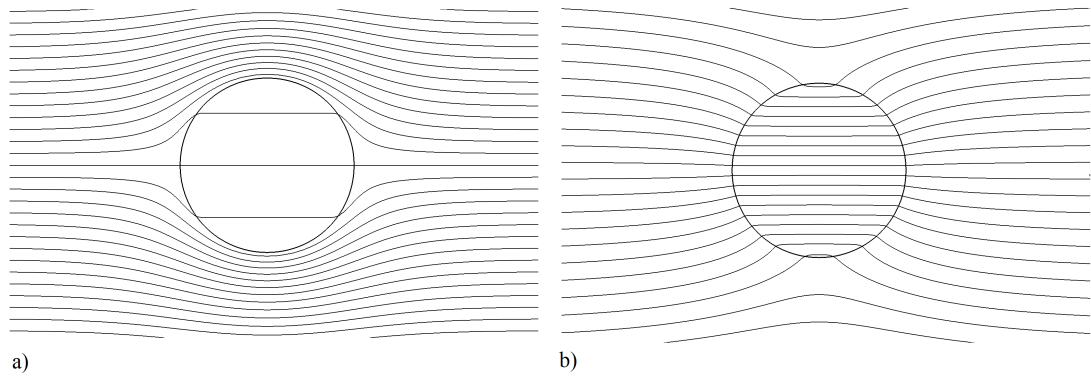
Figure 2.2: Isotherms contours near a spherical droplet for (a) $\tilde{\kappa}/\kappa = 10$, and (b) $\tilde{\kappa}/\kappa = 0.1$.

ature distribution is linear everywhere and one would not be able to recognise the presence of the drop from a simple inspection of the isotherms. On the contrary, when the conductivity of the two fluids are different, the thermal field around the interface is distorted and the velocity of the droplet is affected consequently (cf. Fig. 2.2). More specifically, when the drop conductivity is larger than that of the continuous phase, the migration velocity decreases because the isotherms show the tendency to "embrace" (being tangent to) the drop surface (Fig. 2.2a). In other words, in such conditions the normal components of the temperature gradients become comparatively larger than the tangential ones, which, for the reasons discussed before, constitute the actual "driving force" of the system. In the limiting condition of infinitely large conductivity ratios, the interfacial thermal gradients are exactly normal everywhere and the droplet velocity becomes effectively zero. When the conductivity of the continuous phase is much larger than that of the drop, on the other hand, the migration speed becomes larger because in such a case the isotherms around the interface are more prone to be oriented in the normal direction (Fig. 2.2b), i.e., the effective component of the temperature gradient is maximised.

On deriving Eq. (2.55), the authors postulated a spherical shape for the drop introducing a great simplification in the analytical treatment of the problem. However, as it will be shown in Chapter 6, it is possible to verify a posteriori through the application of the normal stresses balance at the interface, that the sphere is actually a configuration of equilibrium for the droplet, provided that

convective transport phenomena are totally absent. In simple terms, no matter the actual value of the interfacial tension, in steady state conditions and absence of convection the drop interface remains spherical. It is worth to point out that similar arguments apply to the case of a drop subjected the combined effect of gravity and thermocapillarity. Indeed, in the original derivation of Young and co-workers, the gravitational contribution was actually included into the governing equations. In this context however, the physical formulation has been opportunely specialised accordingly to the nature of the problems that have been considered for the present work, i.e., without taking into account the presence of the gravitational contribution.

2.5   Numerical methodology

In a rigorous categorisation, the flow of a system composed of two different immiscible fluids separated by an interface should be correctly referred to as multi-fluid or two-fluid flow, while the term multiphase flow refers to another category, including systems of fluids in the presence of their gaseous phase or in presence of solid phases (particle-laden flows). In this work however, due to the general nature of the methods that will be described below, which can be applied to both multi-liquid and multiphase (in the sense of the liquid-vapour configuration), we will simply refer to multiphase flows, understood the exact meaning that such definition assumes in the present context.

The numerical modelling of multiphase flows constitutes a challenging task. This is due in large measure, but not only, to the intrinsic difficulties related to the necessity to handle complex topological changes, presence of discontinuities across the interface and large separation of scales. During the past years, much effort has been dedicated to develop reliable, efficient and robust methods capable of reproducing accurately the complexity of the physics involved in multiphase flows. Among the extraordinary large variety of methods proposed, it is possible to separate them into four distinct classes of models: i) smoothed-particles hydrodynamics (SPH), ii) lattice Boltzmann methods (LBM), iii) methods based

on a "two-fluids" model, and iv) methods based on a "single-fluid" approach. In the present thesis only some specific sub-models belonging to the latter class (iv), which are pertinent to the present study will be analysed.

Techniques based on the single-fluid approach (the meaning of this term will be clarified in the following section), can be further subdivided in two main categories, namely interface-tracking methods and interface capturing methods (see, e.g., Tryggvason et al. 2011). In the former case, the interface is tracked by means of Lagrangian markers, like in front-tracking methods and marker-and-cells (MAC) method, while in the second methodology, the evolution of the interface is implicitly captured by advecting a suitable "indicator function". In the present thesis, only two of the methods belonging to the interface-capturing category will be examined in some detail; namely the Volume of Fluid method (VOF) and the Level-Set method (LSM), since the solver adopted in the present work is based on a hybrid combination of these two.

The details about the specific hybrid LS-VOF method adopted here will be provided in the next chapter. In the present section, only some general information which is common to the dozen of variants of VOF and Level-Set methods proposed in the past will be discussed.

2.5.1 One-fluid formulation

In section 2.4, it has been shown that a possible way to deal with multiphase flows is to define two separate systems of governing equations (or more generally, in a number equal to the number of phases required by the specific problem) together with the definition of appropriate boundary conditions. An alternative route is to consider the entire system as a single fluid experiencing material properties jump across the interface. In such a way, there would be no need to prescribe interfacial boundary conditions since the interfacial stresses would be directly incorporated into the momentum equation in the form of volume forces applied in the region of the interface. The momentum-balance for a Newtonian non-isothermal multiphase system written in the framework of the

so-called one-fluid or single-fluid approach reads (see, e.g., Lappa, 2005)

$$\rho \frac{D\mathbf{u}}{Dt} = -\nabla p + \nabla \cdot (\eta \mathbf{D}) + \sigma k \mathbf{n} \delta_S + \sigma_T \nabla_S T \delta_S \qquad (2.66)$$

The two additional terms appearing in Eq. (2.66) are the capillary force, $\sigma k \mathbf{n} \delta_S$, where k is the curvature of the interface, and the thermocapillary force, $\sigma_T \nabla_S T \delta_S$, where $\nabla_S T$ is the surface temperature gradient. The term, δ_S, is a distribution which allows to transform surface integrals into volume integrals in the following way

$$\int_S \mathbf{f}_S dS = \int_V \mathbf{f}_S \delta_S dV \qquad (2.67)$$

When the quantity $\mathbf{f}_S$ assumes the role of capillary and thermocapillary stresses, the right hand side of Eq. (2.57) yields the two terms described above. Additionally, it is worth to notice that in Eq. (2.56) the viscosity (as well as any other material property that might be present in the governing equations) must be regarded as a variable, thus it has been therefore retained within the divergence operator.

2.5.2 Volume of Fluid method

Historically, the first work on the Volume of Fluid method (VOF) dates back to Noh and Woodward (1976), but it was only after the introduction of the SOLA-VOF of Hirth and Nichols (1981) that became widely employed. Nowadays the family of VOF methods is arguably one of the most employed strategies for the numerical representation of fluid interfaces, and is constantly experiencing a continuous process of improvement (Mirjalili et al. 2017). The motivation of its success is due to several reasons:

1. Excellent mass preservation;
2. Ability to deal with complex topological changes (break-up and merging of the interface is handled in a natural way);
3. Ease of parallel implementation;

4. Relatively simple extension from two-dimension to three-dimension.

In the following, the basic features common to all VOF method will be presented.

Since the flow is represented by a single set of equations solved on a fixed grid, the different fluids must be clearly identified. This can be accomplished by adopting an "indicator function", $\mathcal{I}_i(\mathbf{x}, t)$, defined in the following way

$$
\mathcal{I}_i(\mathbf{x}, t) = \begin{cases} 1, & if\ \mathbf{x}\ is\ in\ fluid\ i \\ 0, & if\ \mathbf{x}\ is\ not\ in\ fluid\ i \end{cases} \tag{2.68}
$$

where "fluid i" is an arbitrary reference fluid which occupies the position $\mathbf{x}$ at the instant t. If no phase changes are allowed, each fluid particle retains its "identity" as it is advected by the flow. In other words, the derivative of the indicator function following the trajectory of the fluid particle is zero

$$
\frac{D\mathcal{I}}{Dt} = \frac{\partial \mathcal{I}}{\partial t} + \mathbf{u} \cdot \nabla(\mathcal{I}) = 0. \tag{2.69}
$$

On writing Eq. (2.69), the subscript "i" has been suppressed since the indicator function of the two fluids (fluid 1 and fluid 2, we might say) are related by the simple equation $\mathcal{I}_1(\mathbf{x}, t) = 1 - \mathcal{I}_2(\mathbf{x}, t)$. The indicator function can be then integrated over the computational cell (Γ) in the following manner

$$
\alpha_k = \frac{1}{V} \int_\Gamma \mathcal{I}(\mathbf{x}, t)\, dV, \tag{2.70}
$$

where V is the volume of the cell. Thus, the quantity α_k assumes the simple meaning of fractional volume of fluid enclosed into the computational cell. The interface is then simply localised in all the cells such that $0 < \alpha_k < 1$.

In order to derive the advection equation for the volume fraction (i.e., for the interface), we take advantage of the conservation of mass general form (i.e., valid for both compressible and incompressible fluids)

$$
\frac{\partial \rho}{\partial t} + \nabla \cdot (\rho \mathbf{u}) = 0, \tag{2.71}
$$

Using the indicator function, the generic material property field, $\chi(\mathbf{x}, t)$, can be

written as a linear combination of the two constant values assumed in the separate phases, χ_1 and χ_2, in the following manner

$$\chi\left(\mathbf{x}, t\right) = \chi_1 \mathcal{I}\left(\mathbf{x}, t\right) + \chi_2\left(1 - \mathcal{I}\left(\mathbf{x}, t\right)\right) \tag{2.72}$$

Substituting Eq. (2.72) written for the case of the density into Eq. (2.61), and integrating over the computational cell volume, it can be found that

$$\int_\Gamma (\rho_1 - \rho_2)\frac{\partial \mathcal{I}\left(\mathbf{x}, t\right)}{\partial t} dV + \int_\Gamma \nabla \cdot \left[(\rho_1 - \rho_2)\mathcal{I}\left(\mathbf{x}, t\right)\mathbf{u}\right] dV = 0 \tag{2.73}$$

Finally, adopting the Liebniz integration rule, and considering the definition of the volume fraction given in Eq. (2.70), it is possible to obtain an evolution equation for this latter quantity

$$\frac{\partial \alpha_k}{\partial t} + \nabla \cdot \left(\mathbf{u}\alpha_k\right) = 0 \tag{2.74}$$

The intrinsic mass preservation of the method stated before is then a direct consequence of the fact that the advection algorithm is based on a precise conservation law, as it is clarified by the derivation of Eq. (2.74).

Through the integration of Eq. (2.72), it is finally possible to obtain the expression of the generic material property written as a linear combination of the volume fraction phase

$$\chi = \chi_1 \alpha_k + \chi_2\left(1 - \alpha_k\right). \tag{2.75}$$

The system of equations (2.71), (2.74) and (2.75) constitutes the essence of the VOF method. However, the numerical problem is still indeterminate because we need to provide a suitable model that relates the geometrical information contained in the definition of the interfacial force to the volume fraction function.

The interfacial forces introduced in the previous sections have been defined in the context of a continuum approach. Indeed, the one-fluid formulation is general and can be in principle applied even without the necessity of its discretisation.

Nevertheless, in order to provide the mathematical closure of the numerical problem and highlight some well-known issues typical of the method under discussion, it is necessary to see the interfacial forces from a numerical perspective. A possible way to provide their discrete representation would be through the adoption of the so-called continuum surface force model (CSF) of Brackbill et al. (1992), in which the distribution, δ_S, can be numerically approximated as $\delta_S \approx |\nabla_h \alpha_k|$, where the subscript "$h$" has been added to underline the fact that the gradient now is a discrete operator. Other numerical descriptions are possible, like, for instance, the continuum surface stress (CSS) model or the parabolic reconstruction of the surface tension (PROST), but are not used in this thesis and will not discussed here. A possible way to represent the normal and the curvature would be (in the following the "$\approx$" symbol is replaced by an "$=$" for the sake of simplicity, understood that the next equations are discrete, i.e., approximate quantities)

$$\mathbf{n}_h\left(\alpha_k\right) = -\frac{\nabla_h \alpha_k}{|\nabla_h \alpha_k|}, \tag{2.76}$$

$$k_h\left(\alpha_k\right) = -\nabla \cdot \mathbf{n}_h = \nabla \cdot \left(\frac{\nabla_h \alpha_k}{|\nabla_h \alpha_k|}\right). \tag{2.77}$$

Inserting Eqs. (2.76) and (2.77) into the expression of the interfacial forces provided before gives

$$\left(\sigma k \mathbf{n} \delta_S\right)_h = \sigma k_h\left(\alpha_k\right) \mathbf{n}_h\left(\alpha_k\right) |\nabla_h \alpha_k|, \tag{2.78}$$

$$\left(\sigma_T \nabla_S T \delta_S\right)_h = \sigma_T \left[\mathbf{I} - \mathbf{n}_h\left(\alpha_k\right) \mathbf{n}_h\left(\alpha_k\right)\right] \nabla_h T |\nabla_h \alpha_k| \tag{2.79}$$

On deriving expression (2.79), the surface gradient has been explicitly written as the projection of the discrete temperature gradient, $\nabla_h T$, over the interface by means of the operator $\mathbf{I} - \mathbf{n}_h\left(\alpha_k\right) \mathbf{n}_h\left(\alpha_k\right)$. It is clear then, that a precise computation of the interfacial forces is subordinate to the accurate evaluation of the gradient of the volume fraction α_k, which is by definition a "sharp" function across the interface. Specifically, if the capillary force (2.78) is not properly evaluated, the local imbalance of stresses that may occur would originate pressure spikes at the interface that in turn will generate spurious (non-physical) velocity

oscillations that might compromise the accuracy of the computation. This issue, which is common to all the methods based on the one-fluid formulation, becomes particularly problematic whenever the interfacial tension force prevails, imposing stringent limitations on the range of flow regimes that can be covered with the numerical simulations. Adopting opportune smoothing kernels (see e.g., Tryggvasonn et al. 2011) or mollification strategies (cf. Chapter 3) can bring about a better evaluation of $\nabla_h \alpha_k$, which in general helps to reduce the level of spurious velocities. As it will be shown in the next section, in the Level-Set method the above mentioned issue is partially mitigated due to the intrinsic smooth nature of the level-set function.

2.5.3 The Level-Set method

The first application of the Level-Set method in the field of multiphase flows dates back to the work of Sussman, Smereka and Osher (Sussman et al. 1994), in which the method was used for the numerical computation of rising bubbles and falling drops, however the method was initially developed for computer graphic applications during the 1980s by the American scientists Stanley Osher and James Sethian.

Contrarily to the VOF approach, in the Level-Set method the interface is represented through a smooth function $\varphi_k (\mathbf{x}, t)$ called level-set function which reverts its sign from one phase to the other. The boundary between the fluids is located where the condition $\varphi_k (\mathbf{x}, t) = 0$ applies, and the interface is implicitly captured by advecting the level-set function in the following manner

$$\frac{\partial \varphi_k}{\partial t} + \mathbf{u} \cdot \nabla \varphi_k = 0 \tag{2.80}$$

The indicator function then is reconstructed from $\varphi_k (\mathbf{x}, t)$ as

$$I(\varphi_k) = \begin{cases} 0, & \text{if } \varphi_\mathrm{k} < -\varepsilon \Delta \mathrm{x} \\ \frac{1}{2} \left(1 + \frac{\varphi_k}{\varepsilon \Delta x} + \frac{\sin(\pi \varphi_k / \varepsilon \Delta x)}{\pi} \right), & \text{if } |\varphi_\mathrm{k}| \leq \varepsilon \Delta \mathrm{x} \\ 1, & \text{if } \varphi_\mathrm{k} > \varepsilon \Delta \mathrm{x} \end{cases} \tag{2.81}$$

In the above equation, Δx represents the computational cell spacing and ε is an empirical parameter. Similarly to the VOF method, it is possible to compute any material field by means of the indicator function, *viz.*,

$$\chi = \chi_1 I\left(\varphi_k\right) + \chi_2 \left(1 - I\left(\varphi_k\right)\right). \tag{2.82}$$

On advecting the level-set function then, a crucial requisite is that the indicator function remains spread over the same number of cells in the whole interface. This is unfortunately not the case since, when the interface is stretched the indicator function tends to become thinner, and vice versa. In order to deal with this issue, Sussman et al. (1994) proposed the following re-initialisation procedure

$$\frac{\partial \varphi_k}{\partial \tau_f} + \mathrm{sgn}\left(\varphi_{k,0}\right)\left(\left|\nabla \varphi_k\right| - 1\right) = 0, \tag{2.83}$$

where τ_f is an artificial or fictitious time step, and $\varphi_{k,0}$ is the level-set function at the beginning of the computation. Solving Eq. (2.83) until the steady-state has been reached, enforcing the condition $\left|\nabla \varphi_k\right| = 1$ guarantees that the indicator function conserves the same slope (meant as the jump between the two phases) everywhere. For slow moving interfaces, Eq. (2.83) needs to be solved only few times during the computation, while in the presence of fast topological changes it might be necessary to solve it at each time step. Unfortunately, such procedure results in poor mass conservation in a measure directly proportional to the number of re-initialisation steps which can only partially mitigated by the adoption of specific countermeasures but not completely resolved. In spite of this, Level-Set methods are still widely employed and in continuous development because of their relative simplicity and generally better accuracy on the representation of the interface. These characteristics become even more valuable when they are used in combination with other methodologies (hybrid methods), like for instance the VOF method (but not only) which is in general less accurate but preserves mass in a natural way.

The hybrid methodology adopted in the present work is peculiar in a sense that relies on specific variants of the most general interface capturing methodologies

discussed so far. For such reason, we found advisable to postpone its description in the subsequent Chapter 3, where a detailed discussion about the implementation of the solver will be presented.

Chapter 3

Implementation of a multiphase solver for the analysis of thermocapillary flows based on a hybrid LS-VOF approach

3.1 Introduction

The mathematical modelling and numerical simulation of non-isothermal multiphase flows, in which interfacial phenomena are a relevant component, are both demanding and highly complex. A number of effects resulting from the presence of temperature differences must be adequately taken into account to make the results of numerical simulations consistent and realistic. Moreover, in general, gradients of surface tension at the interface separating two liquids are a source of numerical issues that can delay (and in some circumstances even prevent) the convergence of the solution algorithm.

Here, we propose a fundamental and concerted approach for the simulation of the typical dynamics resulting from the presence of a dispersed phase in an external matrix fluid under non-isothermal conditions based on the modular computer-aided design, modelling, and simulation capabilities of the OpenFOAM environment. In the present chapter, we lay the general foundation of the solver used and discuss its implementation starting from an already existing algorithm for multiphase flows (Yamamoto et al. 2016). We discuss all of the steps necessary to expand the range of treatable physical effects and describe in detail the counter-measures taken to circumvent problematic issues associated with the simulation of this kind of flow. It should be noted that the numerical simulations presented

in this chapter are fully three-dimensional and rely on an adaptive mesh refinement (AMR) strategy for reducing the computational cost given the different space scales it involves.

The resulting framework is tested considering the migration of a droplet induced by thermocapillary effects in the absence of gravity considering Newtonian phases. The solver is first validated against the analytical solution of Young et al. (1959) valid under vanishing Marangoni and Reynolds numbers, and against existing experiments performed under microgravity conditions, in which Marangoni and Reynolds numbers are no longer negligibly small (Hadland et al. 1999).

3.2   Governing equations

Let us consider an incompressible multiphase system composed of two Newtonian fluids (a droplet embedded in another immiscible fluid) subjected to a constant temperature gradient $\nabla_\infty T$. It has been shown in Sect. 2.4 that a possible way to approach the problem is to introduce two distinct phases, each with its set of balance equations, and appropriate conditions at the interface to guarantee inter-phase coupling. However, in the present context, we are interested on a numerical solution of the governing equations based on an interface-capturing approach (coupled level-set volume of fluid method) which relies on the "one-fluid" formulation introduced in Sect. 2.5.1. Assuming negligible gravitational effects and the absence of any other external body force, the conservation of momentum for Newtonian fluids can be written (notice that on writing the viscosity, the subscript "0" has been suppressed since we are dealing with Newtonian phases)

$$\rho \frac{D\mathbf{u}}{Dt} = -\nabla p + \nabla \cdot \left[\eta \left(\nabla \mathbf{u} + (\nabla \mathbf{u})^{\mathrm{T}} \right) \right] + \mathbf{f}_\sigma \tag{3.1}$$

where $\mathbf{f}_\sigma$ term is the force accounting for the capillary ($\mathbf{f}_{\sigma,\mathbf{n}}$) and thermocapillary ($\mathbf{f}_{\sigma,\mathbf{t}}$) forces at the interface:

$$\mathbf{f}_\sigma = \mathbf{f}_{\sigma,\mathbf{n}} + \mathbf{f}_{\sigma,\mathbf{t}} = \sigma\left(T_0\right) k\mathbf{n}\delta_S + \nabla_S \sigma\left(T\right)\delta_S \tag{3.2}$$

75

Since the interfacial tension depends on the temperature T (T_0 being a suitable reference temperature), we have explicitly included the related dependence in Eq. 3.2. Closure of the mathematical model requires consideration of the conservation of mass for incompressible flows (Eq. 3.3) and the temperature transport equation (Eq. 3.4):

$$\nabla \cdot \mathbf{u} = 0, \tag{3.3}$$

$$\rho c_p \frac{DT}{Dt} = \nabla \cdot (\kappa \nabla T), \tag{3.4}$$

Following common practice for this kind of problems (see, e.g., Yin, 2012), all material properties are assumed to be constant in each phase and are evaluated at a suitable reference temperature. The dependence on temperature, however, is retained for the surface tension σ via a linear relationship:

$$\sigma(T) = \sigma(T_0) + \sigma_T (T - T_0) \tag{3.5}$$

Although the governing equations are solved in dimensional form, it is useful to provide their dimensionless counterpart to show the dependence of various terms to the dimensionless parameters in the context of the one-fluid formulation. Even though in such a case the material parameters appearing in Eqs. (3.1-3.4) are defined everywhere in the domain, i.e., each of them can be considered as a single (variable) entity characteristic of the fluid as a whole (cf. Eq. 2.75), it has been seen they can undergo discontinuity at the interface, thus, to each phase will be generally attributed a different constant value of each material parameter. Differently from the discussion presented in Sect. 2.5.2, where the material parameters of the two phases were indicated with the generic subscripts "1" and "2", we will now differentiate the two fluids with the subscripts "m" and "d" to indicate they belong to the matrix or to the droplet phase, respectively. In such a case, the dimensionless groups introduced in Sect. 2.4 need to be slightly reformulated for consistency to the definitions provided above, yielding, $Re = \rho_m R U_T / \eta_m$, $Ma = \rho_m c_{p,m} R U_T / \kappa_m$ and $Ca = \eta_m U_T / \sigma$, being the scaling

velocity $U_T = -\sigma_T R \nabla_\infty T / \eta_m$. Using these arguments, the dimensionless form of the momentum and energy balance equation respectively become (as usual, now all the variables must be now regarded as nondimensional)

$$\rho_r Re \frac{D\mathbf{u}}{Dt} = -\nabla p + \nabla \cdot \left[\eta_r \left(\nabla \mathbf{u} + \nabla \mathbf{u}^{\mathrm{T}} \right) \right] + \frac{1}{Ca} k\mathbf{n}\delta_S$$
$$+ \left(T - T_0 \right) k\mathbf{n}\delta_S + \nabla_S T \delta_S \quad (3.6)$$

$$\rho_r c_{p,r} Ma \frac{D\mathbf{u}}{Dt} = \nabla \cdot \left(\kappa_r \nabla T \right) \tag{3.7}$$

having introduced the "relative" material properties, defined as the ratio between the generic property relative to the drop to the one of the continuous phase, $\chi_r = \chi/\chi_m$. It is worth to notice the presence of the additional capillary stress term $\left(T - T_0 \right) k\mathbf{n}\delta_S$ which accounts for the non uniform distribution of the surface tension at the interface produced by temperature gradients. It is possible to show however, that such term can be safely neglected whenever the Capillary number is sufficiently small (refer to Chapter 6 for a more detailed explanation). In the following we will assume that such hypothesis is always verified for our purposes, thus the term under discussion will not be included in the implementation of our code.

3.3 The Simplified LS-VOF Method

Our solver relies on a simplified coupled LS-VOF code based on the hybrid formulation originally developed by Albadawi et al. (2013), (see also Sussman and Puckett, (2000)) implemented into the framework of OpenFOAM (Yamamoto et al. 2016) as an extension of the standard VOF solver "interFoam".

In the algebraic volume of fluid "interFoam" solver available in OpenFOAM, the volume fraction phase is advected using a surface compression approach in combination with high-resolution numerical schemes, making unnecessary the geometric reconstruction of the interface. The main advantage of such procedure lies on its robustness and ability to handle complex interfaces with a reduced computational cost. Unfortunately, despite the above mentioned benefits, the method

is generally less accurate than geometric VOF codes, especially for low Capillary number flows, where the accuracy on the evaluation of the interface geometrical properties (namely, the unit normal and the curvature) is imperative. A possible strategy to partially overcome such inefficiencies without the necessity to implement complicated and computationally expensive geometric methodologies is to combine the excellent mass preservation (in addition to the previous mentioned strong points) of an algebraic VOF code with a generally more accurate level-set method. In the following we describe briefly the simplified LS-VOF methodology introduced by Albadawi et al. (2013).

The equation for the volume fraction solved in OpenFOAM reads

$$\frac{\partial \alpha_k}{\partial t} + \nabla \cdot (\alpha_k \mathbf{u}) + \nabla \cdot (\alpha_k (1 - \alpha_k) \mathbf{u}_c) = 0 \tag{3.8}$$

where α_k is the above mentioned volume fraction and $\mathbf{u}_c$ is an artificial "compressive velocity" (Berberović et al. 2009). We notice that Eq. (3.8) differs from Eq. (2.74) from the presence of an additional term on the right hand side, which serves to alleviate the numerical diffusion of the interface through the compressive term that is active only in for $0 < \alpha_k < 1$. To see the effect of this contribution from a "kinematic" perspective, we can imagine the compressive velocity as an effective additional velocity normal at the interface acting on both sides in the same direction but opposite orientation (i.e., at each point, the resultant vector is zero), which prevents the interface smearing in a measure directly proportional to the extent of the velocity $\mathbf{u}_c$. From a numerical point of view, on the other side, the presence of an additional convective term serves to counterbalance the numerical error arising from the solution of the advection equation.

Although the hybrid implementation of Yamamoto et al. (2016) improved the solver in terms of accuracy, we had to take additional countermeasures to fix typical "algorithm stability" issues at the interface (where Marangoni stresses of thermal nature are produced). This was accomplished by "proper" smoothing, both of the level set and the volume of fluid phase functions, as further described in Section 3.4.

The resulting time-marching procedure can be outlined as follows: in order to calculate the level set function φ_k, we first calculate the field $\varphi_{k,0} = (2\alpha_k - 1)\Gamma$, where $\Gamma = 0.75\Delta x$ and Δx is the grid resolution (see Albadawi at al. 2013). Subsequently, the re-initialisation equation (Eq. 2.83) is solved with the initial condition $\varphi_k(\mathbf{x}, 0) = \varphi_{k,0}(\mathbf{x})$. Once the scalar field φ_k is known at each point, it is possible to evaluate the curvature at the interface

$$k(\varphi_k) = -\nabla \cdot \mathbf{n}(\varphi_k), \tag{3.9}$$

with $\mathbf{n}(\varphi_k) = \nabla\varphi_k/|\nabla\varphi_k|$ being the unit normal at the interface. Finally, the term described by Eq. 3.2 is evaluated, leading to the momentum equation cast in compact form as

$$\rho\frac{D\mathbf{u}}{Dt} = -\nabla p + \nabla \cdot \left[\eta\left(\nabla\mathbf{u} + (\nabla\mathbf{u})^{\mathrm{T}}\right)\right]$$
$$+ \sigma k(\varphi_k) I(\varphi_k) \nabla\varphi_k + \sigma_T \nabla_S T |\nabla\alpha_k| \tag{3.10}$$

where $I(\varphi_k)$ is given by Eq. 2.81.

3.4 Implementation of the thermal Marangoni migration method in OpenFOAM

The solution strategy has been based on a classical Finite Volume Method (FVM) approach relying on the governing equations cast in integral form over a set of control volumes. More precisely, the equations have been solved in a Cartesian coordinate system using a three-dimensional mesh composed of hexahedrons with the open-source tool-box OpenFOAM.

With OpenFOAM, as for all classical techniques pertaining to the so-called category of fractional step methods (also known under several other names, such as projection methods or pressure-based methods), the velocity and pressure fields are determined in a disjoint (sequential) manner. In particular, the pressure is computed via the solution of a Poisson-like equation obtained combining the discrete momentum equation and the continuity equation (the so-called PISO algo-

rithm, see, e.g., Jang et al. 1986 or the exhaustive book by Moukalled et al. 2016 for additional details). The implementation of the PISO method in OpenFOAM relies on a non-staggered collocation of the different problem variables on the underlying computational grid (which means all primitive variables are located at the same grid points); in order to prevent the code from developing spurious oscillations (caused by a not well-resolved coupling between pressure and velocity, see, e.g., Choi et al. 1994 and 1994a and references therein), the convective flux at each control volume face is determined resorting to the scheme originally developed for Cartesian grids by Rhie and Chow, (1982) which in OpenFOAM has been extended and adapted for generalised coordinates.

All the convective and diffusive terms are treated implicitly whereas other source terms eventually present in the equations (i.e., the surface-tension term in the momentum equation) are discretised explicitly. The solution of the energy equation has been implemented in the classical segregated manner (see, e.g., Patankar and Spalding, 1972 and Van Doormaal and Raithby, 1985), i.e., the momentum and energy equations are solved one at a time, with the coupling implemented in an explicit way.

For all the cases, the first order accurate implicit Euler temporal scheme has been used. The diffusive terms have been discretised using a standard central difference scheme, while in the momentum and energy equations the convective terms have been discretised using the QUICK scheme (Leonard, 1979). Such choices proved to be the best compromise in terms of 1) algorithm stability, 2) mesh convergence, and 3) numerical accuracy (the reader is referred to the grid-refinement tests and the validation studies reported in Sect. 3.5.2).

In addition to the above careful treatment, we had to use properly mollified variables to increase algorithm stability and mitigate unphysical effects at the interface. More precisely, the smoothing was applied to each "relevant variable" (representing various variables required by the LS and VOF implementation in different parts of the solver, as needed) using a "pure diffusive" evolution equation

$$\varsigma_{k,mol}^{n+1} = \varsigma_{k,mol}^n + \left(\nabla^2 \varsigma_{k,mol}^n\right) \Delta\tau_{mol} \tag{3.11}$$

where τ_{mol} is an artificial or fictitious time, to be solved with the initial condition for a prefixed number of cycles n (the condition $n = 0$ corresponding to the recovery of the original non-smoothed function). $\Delta\tau_{mol}$ is defined according to the following well-known numerical stability criterion (see, e.g., Fletcher, 1991):

$$\Delta\tau_{mol} = \frac{0.5^2}{(1/\Delta x)^2 + (1/\Delta y)^2 + (1/\Delta z)^2} \tag{3.12}$$

We used mollified quantities to evaluate the new curvature at each time step, i.e.,

$$k_{\varphi,mol} = -\nabla \cdot \mathrm{n}_{\varphi,mol} = -\nabla \cdot \frac{\nabla\varphi_{k,mol}}{|\nabla\varphi_{k,mol}|}, \tag{3.13}$$

where $\varphi_{k,mol}$ is the smoothed version of φ_k.

As discussed in Section 3.2, accounting for surface-tension effects requires two additional source terms in the momentum equation (see Eq. 3.2). In the framework of an optimisation strategy based on a trial-and-error approach, we could obtain the best results using the mollified level set function to determine the unit vector perpendicular to the interface (and the corresponding tangent unit vector) and retaining a non-mollified volume fraction in the gradient appearing in the expression of the thermal contribution (see Eq. 3.13). The level set function was also used accordingly to determine the curvature.

$$\mathbf{f}_{\sigma,\mathbf{t}} = \sigma_T \nabla_S T \, |\nabla\alpha_k| = \sigma_T \left(\mathrm{I} - \mathbf{n}_{\varphi,mol}\mathbf{n}_{\varphi,mol} \right) \nabla T \, |\nabla\alpha_k| \tag{3.14}$$

Following common practice in the literature (Brackbill et al. 1992), the smoothing philosophy can also been applied to the fluid properties (assumed to be constant in each phase) in order to prevent the algorithm from developing spurious oscillations due to the discontinuity established at the liquid-liquid interface. In our hybrid implementation, we decided to rely on a standard VOF approach, expressing each property as

$$\chi = \alpha_{k,mol}\chi_d + (1 - \alpha_{k,mol}) \chi_m \tag{3.15}$$

In order to improve the accuracy without increasing too much the computational cost (the considered problem is 3D), we also deemed it necessary to use an adaptive mesh refinement technique (especially for relatively high values of the Marangoni number for which relatively thin thermal boundary layers tend to emerge at the matrix-droplet interface). The approach implemented in Open-FOAM is based on the h-refinement strategy (see, e.g., Kittur and Huston, 1989), in which additional computational points are inserted locally in some regions without disturbing the rest of the mesh. It is also possible to remove points from regions in which they are no longer necessary through an "unrefinement procedure". To define the regions to be enriched with additional points we have used as a controlling variable, a mollified scalar field, $\alpha^*_{k,mol}$, expressly defined for such a purpose and defined using the volume fraction α_k (with points being dynamically added to the region where $\alpha^*_{k,mol} > \alpha^*_{k,thr}$ and removed from the rest of the domain). The method is particularly suitable for problems with discontinuous properties such as those considered here (Coelho et al., 1991 Vilsmeier and HÄanel, 1993 and Fuster et al., 2009).

Special care has also been devoted to the solution of the energy equation. Some mathematical manipulations were indeed necessary to increase algorithm stability and its related ability to reproduce available test cases in the literature (as discussed later in this chapter). We rearranged the energy equation (Eq. 3.4) as follows: by introducing the thermal diffusivity $D_{th} = \kappa/\rho c_p$ and considering that all the fluid material properties can, in general, change across the interface we have

$$\nabla \cdot (D_{th}\nabla T) = D_{th}\nabla^2 T + \nabla D_{th} \cdot \nabla T \tag{3.16}$$

which can be re-arranged as follow

$$D_{th}\nabla^2 T = \nabla \cdot (D_{th}\nabla T) - \nabla D_{th} \cdot \nabla T \tag{3.17}$$

furthermore, dividing both sides of Eq. 3.4 by ρc_p we find

$$\frac{1}{\rho c_p}\nabla\cdot(\kappa\nabla T) = \frac{\kappa}{\rho c_p}\nabla^2 T + \frac{1}{\rho c_p}\nabla\kappa\cdot\nabla T = D_{th}\nabla^2 T + \frac{1}{\rho c_p}\nabla\kappa\cdot\nabla T \qquad (3.18)$$

Finally, by substituting Eq. 3.17 into Eq. 3.18 we obtained the following equivalent expression for the energy equation:

$$\frac{DT}{Dt} = \nabla\cdot(D_{th}\nabla T) + \frac{1}{\rho c_p}\nabla\kappa\cdot\nabla T - \nabla D_{th}\cdot\nabla T. \qquad (3.19)$$

3.4.1   Solution procedure

The different macro-steps in which our algorithm has been articulated can be summarised as follows:

1. Set the boundary and initial conditions;
2. Solve the re-initialization equation (Eq. 2.83);
3. Solve the diffusion equation (Eq. 3.11) to obtain the smoothed level-set function $\varphi_{k,mol}$;
4. Solve the equation for the volume fraction (Eq. 3.8) using the MULES algorithm (see, e.g., the OpenFOAM user guide, 2008) to guarantee the boundedness of the scalar field. Applying the Gauss theorem, the integration of Eq. 3.6 leads to

$$\int_{\Gamma_{c.i}}\frac{\partial\alpha_k}{\partial t}dV + \int_{\partial\Gamma_{c.i}}\left(\alpha_k\mathbf{u} + \alpha_k\left(1-\alpha_k\right)\mathbf{u}_c\right)\cdot\mathbf{n}_f dS = 0 \qquad (3.20)$$

where $\Gamma_{c,i}$ is the volume of the computation cell i and $\partial\Gamma_{c,i}$ its boundary. Using the forward Euler scheme, the discrete counterpart of Eq. 3.20 can be written as

$$\left|\Gamma_{c,i}\right|\frac{(\alpha_k)_{c,i}^{n+1} - (\alpha_k)_{c,i}^{n}}{\Delta t} = -\sum_{f_{c,i}} F_u^n - \sum_{f_{c,i}} \zeta_M F_c^n \qquad (3.21)$$

where the flux term F_u arises from the integration of $\nabla\cdot(\alpha_k\mathbf{u})$, the subscript $f_{c,i}$ indicates the face of the cell i, and the term F_c is a linear combination

of the flux associated with the integration of the compressive term $\nabla \cdot (\alpha_k (1 - \alpha_k) \mathbf{u}_c)$ and the previous flux F_u. The coefficient ζ_M appearing in the second term in the right hand side of Eq. 3.21 is the MULES limiter. The term F_c is active only across the interface, where $\zeta_M = 1$, on the other hand, away from the interface, $\zeta_M = 0$, which makes F_c inactive. The effect of the limiter is therefore to split the numerical treatment of the advection term in two parts: away from the interface, the second summation appearing in Eq. 3.21 is set to zero, and F_u is treated with an upwind scheme, while across the interface, where a better accuracy is required, a higher order scheme is employed. This strategy allows to reduce the computational effort by activating the more accurate scheme only in the region of the interface, where higher accuracy is required. Finally, the compressive velocity $\mathbf{u}_c$ defined previously takes the following form

$$\mathbf{u}_c = \min \left[C_\alpha \frac{|\mathbf{u}_f \cdot \mathbf{S}_f|}{|\mathbf{S}_f|}, \max \left(\frac{|\mathbf{u}_f \cdot \mathbf{S}_f|}{|\mathbf{S}_f|} \right) \right] \mathbf{n}_f \tag{3.22}$$

Here, $\mathbf{u}_f$, $\mathbf{S}_f$ and $\mathbf{n}_f$ are the value of the velocity interpolated at the cell face, cell face area vector and cell face normal, respectively. The numeric constant, C_α, is a user defined parameter and usually is set in the range 0 (the compressive velocity is inactive) to 2. Larger values of C_α correspond to a sharper interface but higher spurious currents. In our simulations we used $C_\alpha = 2$ for all the cases;

5. Solve the energy equation (Eq. 3.16);

6. Compute the thermal Marangoni force $\mathbf{f}_{\sigma,\mathbf{t}}$ (cf. Eq. 3.2);

7. Calculate the velocity and pressure field using a projection method (PISO algorithm);

8. Go back to step 1 or end of calculation.

3.5 Solver validation

3.5.1 Drop migration velocity in the absence of convective transport

As indicated in Sect. 3.4, our overall framework has been built via the integration of self-contained modules, which could be individually tested. However, because it is crucial that the entire numerical architecture be tested as a single integrated unit, we considered available solutions in the literature for comparison. In order to validate our code, in particular, we focused on the thermocapillary motion of a spherical Newtonian droplet of radius R in a constant temperature gradient $\nabla_\infty T$ embedded in an unconfined Newtonian matrix in the limiting case of $(Ma, Re) \to 0$ and negligible buoyancy effects. As discussed in Sect. 2.4.1, in such a case, an analytical solution exists for the velocity of the droplet calculated by Young et al. 1959 (Eq. 2.65). In our simulations, we assumed conditions corresponding to the following set of (non-dimensional) characteristic numbers: $Pr = 0.1$, $Re = 1.0 \times 10^{-4}$, $Ma = 1.0 \times 10^{-5}$ and $Ca = 2.0 \times 10^{-1}$. For simplicity, we considered the fluid material parameters to be the same for both fluids (i.e., unit fluid property ratios). Assuming the radius of the droplet to be $R = 0.5\,\mathrm{cm}$, we fixed the size of the external container to $(6 \times 4.5 \times 4.5)\,\mathrm{cm}^3$ corresponding to a confinement ratio $C = 2R/w = 0.22$, where w represents the width of the cross-section of the domain. This size is intended to mimic the effective geometry of the container used in the experiments by Hadland et al. (1999) (illustrated in Fig. 3.1) for the reasons that will appear clear in the next section. In spite of the presence of confinement, it will be shown that the particular conditions considered here are such that the drop can reach the theoretical velocity predicted by the YGB theory with sufficient accuracy.

The simulations have been performed adopting a structured mesh with $85 \times 64 \times 64$ elements adaptively refined in the region of the drop (cf. Fig 3.3). For the boundary conditions, we have applied no-slip and no-through flow conditions for the velocity and "zeroGradient" for the pressure at each wall of the container (a reference pressure equal to 0 has been set at the centre of the "cold" wall). For the temperature, we set constant values at the "cold" and "hot" sides and
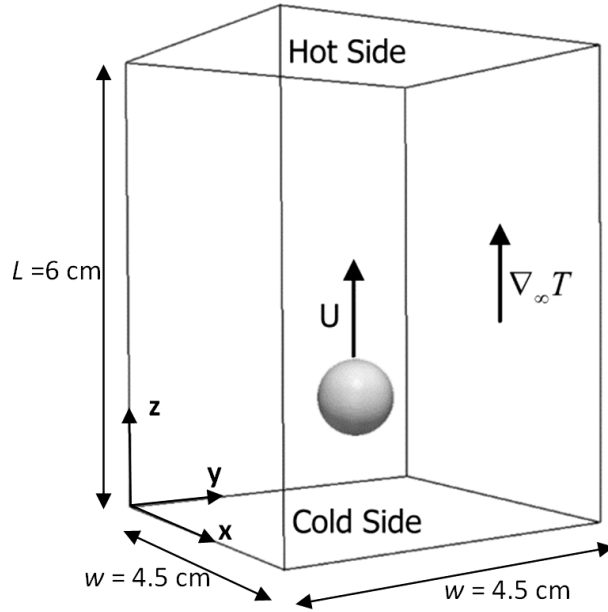
Figure 3.1: Schematics of the parallelepipedic configuration (equivalent to the experiment of Hadland et al. 1999) and coordinate axes considered in the numerical study.

adiabatic ("zeroGradient") conditions in the rest of the boundaries of the domain. All simulations were executed applying two ($n = 2$) cycles of smoothing for the
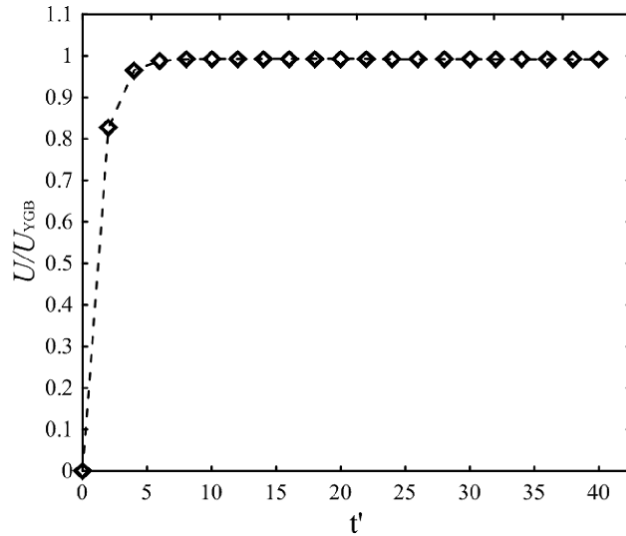
Figure 3.2: Temporal evolution of the drop migration velocity normalised with the theoretical value of Young et al. (1959) obtained in conditions of negligible convective transport.

Level Set function φ_k (for $n < 2$ the solution was found to be inaccurate, whilst for $n > 2$ no appreciable improvement have been observed), whilst the time step has been selected on the basis of stability considerations (see, e.g., Galusinski and

Vigneaux, 2008).

$$\Delta t \leq 0.5 \left(C_2 \frac{\eta \Delta x}{\sigma} + \sqrt{\left(C_2 \frac{\eta \Delta x}{\sigma} \right)^2 + 4 C_1 \frac{\rho \Delta x^3}{\sigma}} \right) \qquad (3.23)$$

where C_1 and C_2 are coefficients that depend on the particular solver used (as indicated by Deshpande et al. 2012). Fig. 3.2 shows the dimensionless migration velocity as a function of the dimensionless time $t' = \eta_m / |\sigma_T| \nabla_\infty T$ for the same case. After the transient, the droplet reaches a steady state in which its final migration velocity is in excellent agreement with the predictions of the YGB theory.

3.5.2 Comparison with existing experiments in microgravity conditions

In the previous section, the performance of our solver has been assessed in the limiting case of vanishing Marangoni and Reynolds numbers for which the velocity can be expressed via the so-called Young formula. In this section, we focus on the case where thermal and momentum convective terms play a key role, i.e., finite values of the Marangoni and Reynolds numbers. In particular, the reliability and accuracy of the code are tested considering the experimental measurements of Hadland et al. (1999) (cf. Sect. 1.2.1) obtained in microgravity conditions during a NASA space shuttle mission in which the thermal Marangoni migration of a fluorinert drop enclosed in a box filled with silicone oil was examined. The experiments were conducted using the same domain considered in Sect 3.5.1 (i.e., the box with a square cross-section $(4.5 \times 4.5)\,\mathrm{cm}^2$ and a height of 6 cm shown in Fig. 3.1). Droplets of different diameters were considered so that a relatively large range of Marangoni numbers was covered (from approximately 10 to 4000). An imposed temperature gradient was applied by maintaining two opposite sides of the domain at a different temperature. As the droplet moved from the cold region to the hot region, its position was monitored and recorded using a motion picture camera. Table 3.1 summarises the fluid properties adopted during the experiments, which have been also considered for our numerical simulations.

Table 3.1: Fluid properties adopted for the simulations (density and viscosity have been calculated at the average temperature of 313K using the correlations available in Hadland et al. 1999).

	$\rho\,[\mathrm{kg/m}]$	$\eta\,[\mathrm{Pa\ s}]$	$\kappa\,[\mathrm{W/(m\ K)}]$	$c_p\,[\mathrm{J/(kg\ K)}]$	$Pr[\text{-}]$
Matrix	918.3	0.00729	0.1339	1778	98.86
Drop	1728	0.00102	0.0630	1047	17.03

Our goal is to test the solver considering effective conditions, i.e., adopting the same geometrical constraints and flow conditions of a real experiment and performing fully three-dimensional (3D) simulations (most of past results available in the literature have been obtained under the approximation of axisymmetric flow). In addition, using this test case we were able to test the implementation in the presence of property jumps at the interface, which is usually problematic to handle with interface capturing methods.

As outlined in the previous section, to discretise the domain we have used the adaptive mesh capabilities offered by the OpenFOAM platform in order to ensure a sufficiently refined mesh in the region of the droplet, where a better resolution is required (the refinement being applied essentially to the whole drop and its surrounding area). In order to assess the sensitivity of the solution to the mesh density, we conducted a set of simulations (at a fairly high value of the Marangoni number (Ma = 100) as a representative reference condition) considering three different levels of refinement (indicated by M_1, M_2 and M_3, cf. Table 3.2) obtained by halving the mesh spacing at each refinement.

Table 3.2: Characteristics of the meshes used for the mesh-independence assessment study

	Mesh M_1	Mesh M_2	Mesh M_3
Nr of cells per drop diameter	28	56	112
Grid resolution ($\Delta x = \Delta y = \Delta z$)	0.0003572	0.0001786	0.0000893

On the basis of the results provided by the mesh independence study summarised in Fig. 3.3a, we could discern the minimum resolution needed to obtain grid-independent results (the resolution named "M_2" in Table 3.2). Note that,
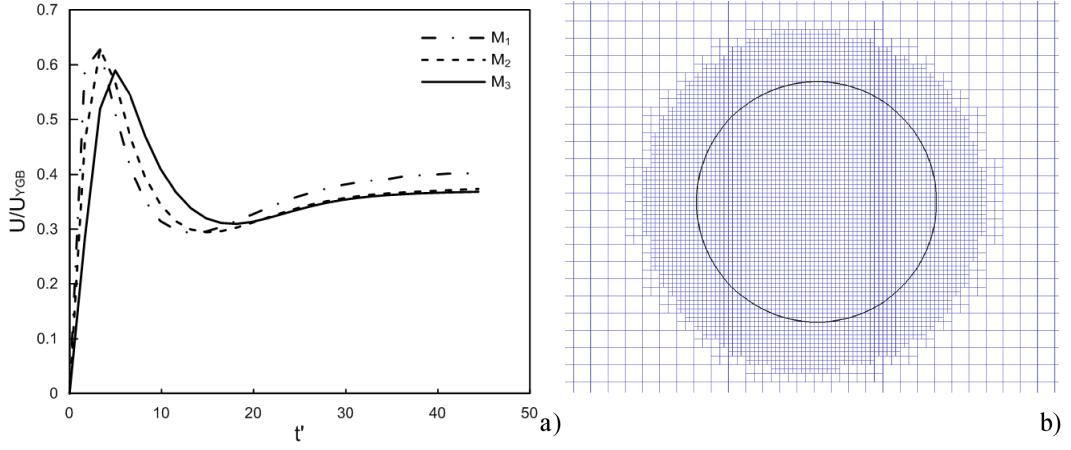
Figure 3.3: a) Outcomes of the 3D mesh refinement study for $Ma = 100$ (scaled droplet velocity for three different mesh resolutions); b) Adaptively refined 3D mesh with "local" resolution M_2 in the center-lane $y = 2.25$.

while mesh M_1 is not resolved enough to capture the thermal boundary layer established in the front region of the droplet (we performed this study considering $Ma = 100$, thus a thermal boundary layer is expected to be established in the front region of the droplet), meshes M_2 and M_3 capture the physics correctly, as shown by the migration velocity results in Fig. 3.3a, which converge to very similar values of the final velocity (percentage difference for the final velocity smaller than 1%). It is worth pointing out that a uniform 3D mesh having the same resolution throughout the domain would have required 26 millions of cells, which has to be regarded as an almost "prohibitive task" in the context of a parametric analysis such as that conducted in the present work.

Figure 3.4 shows the drop migration velocity normalised with the theoretical velocity predicted by the model of Young et al. (1959) as a function of the dimensionless time. A range of different values of the Marangoni number (from 2 up to 500) has been considered. For Ma up to 100, in agreement with previous simulations (see e.g. Yin et al. 2012) our results have confirmed that after an initial transient time the droplet velocity reaches a plateau region, attaining a steady state. For the highest values of Ma considered here ($Ma = 200$ and 500), however, the size of the considered domain was not sufficiently long to allow the droplet to reach such a state. As an example, for such values of the Marangoni number, Yin et al. (2012) showed that after attaining the first plateau region
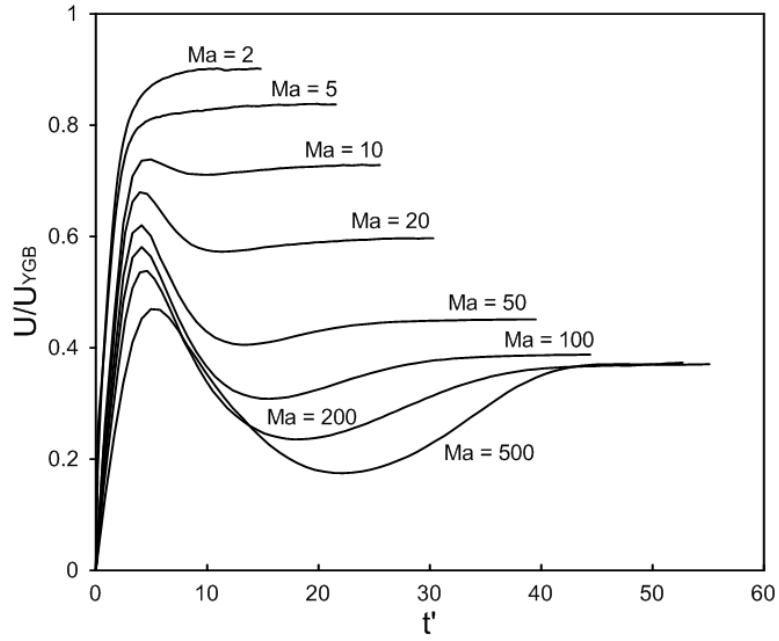
Figure 3.4: Time evolution of the normalised droplet velocity for different values of the Marangoni number.

visible in Fig. 3.4, the velocity would rise again and tend to a second plateau). In order to assess expressly the influence of the domain extension for such values of the Marangoni number, we performed an additional simulation using a (two times) larger domain length for the case for $Ma = 200$. The results, summarised in Fig. 3.5 confirm that after the first plateau the droplet undergoes a second stage of acceleration and eventually its speed converges to a final steady state value (the final velocity obtained in our simulation has been found to be in qualitative agreement with the result obtained by Yin et al. (2012) in similar conditions).

In order to compare our numerical results with the experiments of Hadland et al. 1999, we followed the same procedure used in the experiments, i.e., we considered for comparison the velocity attained by the droplet at $z \sim 4$ cm. Fig. 3.6 summarises our results on the effect of Marangoni number on the scaled migration and compares them to previous works in the literature, showing the good agreement between our results and the experiments of Hadland et al. (1999). Notice also the agreement between our data and the simulations by Ma (1999) for Marangoni up to 100. Above this value the two trends deviate considerably. Such differences might be explained by the limited extension of the geometry.
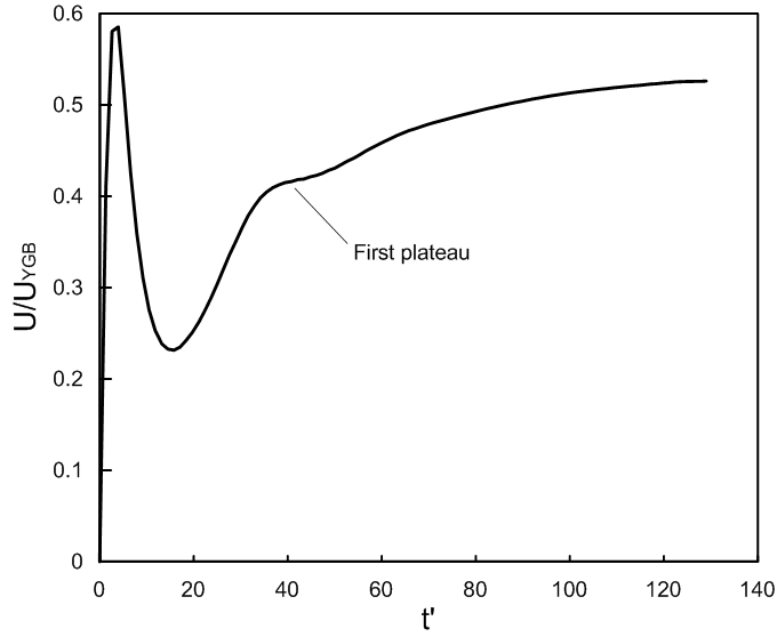
Figure 3.5: Normalised droplet velocity for $Ma = 200$ as a function of the dimensionless time in a domain two times longer than that used in the previous simulations.

As previously pointed out, for Marangoni numbers larger than 100 the distance covered by the droplet required to reach a final steady state increases considerably and, therefore during the experiments the droplet did not have enough time to reach the terminal velocity. By considering exactly the same domain of the experiments in our simulations, our results are able to capture correctly the experimental trend.

3.6   Conclusions

In this chapter, we addressed the question of how a typical numerical framework for isothermal multi-phase flows can be adequately extended to make it suitable for the simulation of phenomena in which surface-tension gradients act as the main flow or pattern driver. In particular, starting from existing implementations in OpenFOAM of moving-boundary methods, some effort has been put into strengthening the used approach by incorporating the possibility of accounting for thermal effects of different nature in the algorithm. Special care has been devoted to numerical stability issues that are typical of such problems (in which the phenomena occurring in a limited neighbourhood of the interface separating
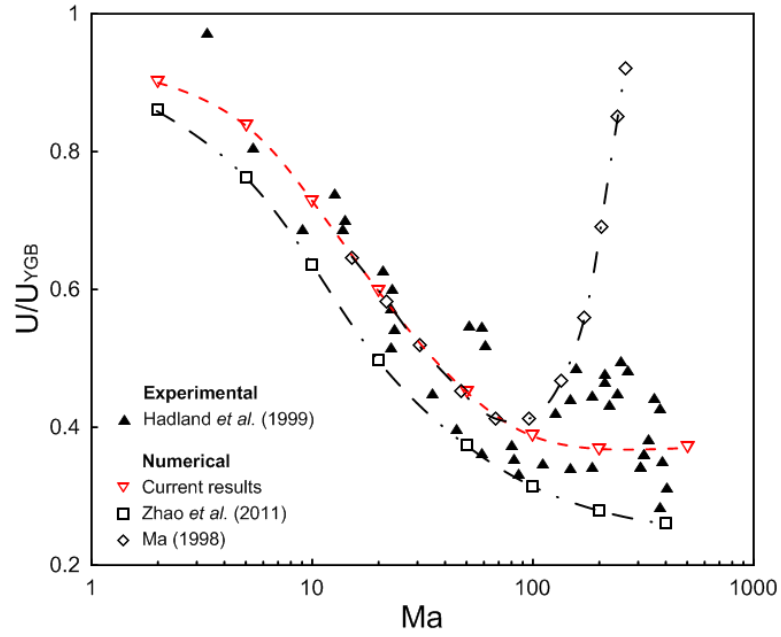
Figure 3.6: Effect of the Marangoni number on the normalised velocity. The dashed red line represents a spline fit to our numerical results (open triangles), the closed triangles represent experimental results; and the open symbols (squares and diamonds) correspond to numerical predictions from other authors.

the two liquids play a "crucial role"). The framework has been tested against the well established analytical results of Young et al. (1959) obtained in absence of convective transport (i.e., for $(Re, Ma) \rightarrow 0$), and considering the experimental results by Hadland et al. (1999) where property jumps, effect of inertia and convective transport of energy are considered. The numerical predictions have been found to be in excellent agreement with all test cases considered.

Chapter 4

Walls and domain shape effects on the thermocapillary migration phenomenon

4.1 Introduction

The thermocapillary motion of liquid droplets in fluid media depends on a variety of influential factors, including the not yet fully understood role played by the presence of the walls and other geometrical constraints, such as the effect of confinement, the initial (symmetric or asymmetric) position of the droplet and its proximity to solid walls, and the shape of the considered container. Apart from the general interest from the point of view of applied mathematics, wall-effects and geometrical constraints in general (see e.g. Meyyappan et al. 1981) may be an important source of discrepancies observed between idealised numerical simulations (carried out under the assumption that the droplet motion is initially located exactly at the "centre" of the container, e.g., the symmetry axis for a cylindrical container) and the results provided by experiments. In fact, results obtained in microgravity environments, such as in sounding rockets (see, e.g., Wozniak, 1991) or in the Space Shuttles (Balasubramaniam et al. 1996 and Hadland et al. 1999) have provided disjoint glimpses of a range of qualitatively and quantitatively different results in widely different parts of the parameter space.

In this chapter, our final aim is the proper discernment of the triadic relationship established among viscous phenomena, thermal effects and other specific behaviour due to the proximity of the droplet to one or more solid boundaries.

Different geometric configurations are considered, including straight, converging and diverging channels, droplets under different confinement, as well as the asymmetric proximity of the droplets to a single or adjacent sidewalls. Distinct boundary conditions and flow regimes are also examined, including both $(Ma; Re) \to 0$ and non-negligible Ma flows. In all the cases discussed in this chapter, both the dispersed and the matrix fluids are assumed to be Newtonian and solid boundaries are considered to be adiabatic unless stated otherwise as in the analysis discussed in Sect 4.3.

4.2 Effect of the walls on the motion of an off-centred droplet

In this section, we study the dynamics of the wall-droplet interaction for the same parallelepipedic domain, same droplet radius and fluid properties adopted in the previous chapter corresponding to the experimental set-up of Hadland et al. (1999). However, to assess the effect of the proximity to the wall, we performed a series of numerical experiments releasing the drop with an initial "off-set" position with respect to the centre of the channel as schematically shown in Fig. 4.1. In section 4.2.1, we analyse the case of an off-centred droplet by varying its initial position in the x-direction (this situation is referred to as the droplet-near-side "NS" case, Fig. 4.1a) whilst in Section 4.2.2, we look at the "joint" effects produced by the proximity of the droplet to two sidewalls (by setting the droplet off-set in both x- and y- directions, this configuration will be referred to as the droplet-near-corner "NC" case). To the best of our knowledge, no simulations or experiments have been expressly devoted to addressing this problem. In order to quantify the "proximity" of the droplet to the wall (i.e., the drop interface-wall distance), and to give a measure of how far its centre is set away from the centre of the channel, conveniently, we define the following two dimensionless parameters: the "degree of proximity" $\theta = R/(s - R)$, and the "off-set parameter" $e = (d - s)/d$ (refer to Fig. 4.1 for the definition of the
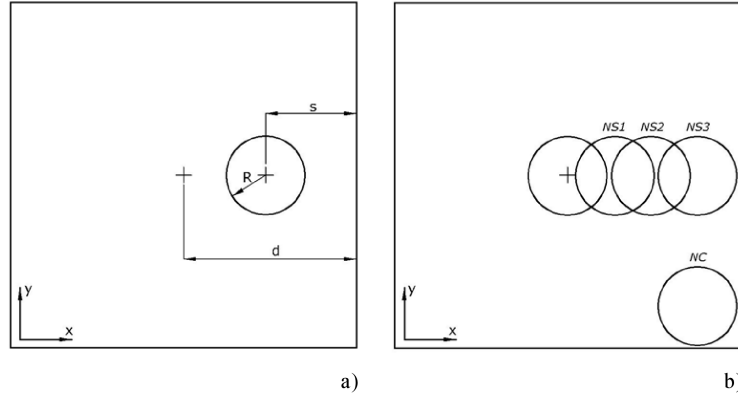
Figure 4.1: a) Sketch of the domain in a plane normal to the direction of the motion: a) off-set droplet, with relevant variables used to define its initial position. b) Initial position of the droplets for all the configurations considered.

geometrical variables). These two quantities are obviously related to each other:

$$\theta = \frac{1}{d/R\left(1-e\right)-1} \tag{4.1}$$

4.2.1   Proximity to a side-wall

In our analysis, we studied three different initial configurations in which the parameter e was $e = 0.25$ (NS_1, $\theta = 0.42$), $e = 0.50$ (NS_2, $\theta = 0.8$) and $e = 0.73$ (NS_3, $\theta = 4.65$), with the latter corresponding to a distance $d - s \sim 3R$, in addition to the original case for $e = 0$ ($\theta = 0.286$) considered previously in Chapter 3. In order to assess wall effects in two different cases for which the role of the temperature field is expected to be different, two distinct flow regimes with $Ma = O\left(1\right)$ and $Ma = O\left(10^2\right)$ are considered, namely $Ma = 2$ and $Ma = 100$, (notice that for the matrix liquid $Pr \approx 100$, therefore the Reynolds number is $Re < O\left(1\right)$ and $Re = O\left(1\right)$, respectively). While in the first case, both the convective transport of momentum and energy can be assumed to be negligible (creeping flow conditions), in the latter case they can not (especially the convective transport of heat, which is expected to produce significant distortions in the temperature field with respect to purely diffusive, i.e., thermally stratified, conditions).

The differences between these two regimes in terms of behaviour of the non-centred droplet can be clearly appreciated in Fig. 4.2, which shows the droplet
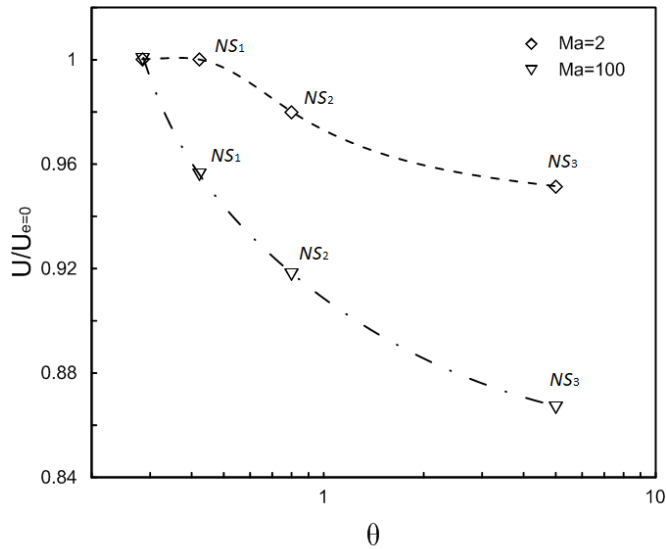
Figure 4.2: Effect of the proximity to a side-wall on the normalised migration velocity for two different flow regimes. The lines are a guide to the eye.

migration velocity normalised using the velocity it would reach if it was released from the centre of the domain (i.e., the steady-state velocity for $e = 0$) as function of the parameter θ. The results indicate that in both regimes, as the drop is released in a position increasingly closer to the wall, the migration velocity decreases. However, such a decrease is enhanced for larger values of the Marangoni number. For $Ma = 2$ when $e = 0.25$ ($\theta = 0.42$), the droplet does not "feel" any wall effect. On the other hand, at $Ma = 100$, the droplet undergoes a significant decrease in speed even for relatively small values of e. Such results suggest that for the particular geometry adopted by Hadland et al. (1999) for large Ma, even relatively small departures from the condition of perfectly centred droplet might influence the observed droplet dynamics and velocity of migration. As anticipated, this scenario can be explained by considering the specific behaviour of the temperature field. At $Ma = 2$, the temperature field attains a quasi-linear distribution (see Fig. 4.3a for the case in which the droplet was released at the closest position next to the wall ($e = 0.73$)). In such circumstances it is clear that most of the deceleration produced by the proximity to the side wall has to be ascribed to kinematic effects (the increased viscous drag to which the droplet is subjected owing to its interaction with the side wall, which leads to an increase in the shear stresses in the region between the droplet and the wall). For larger

96
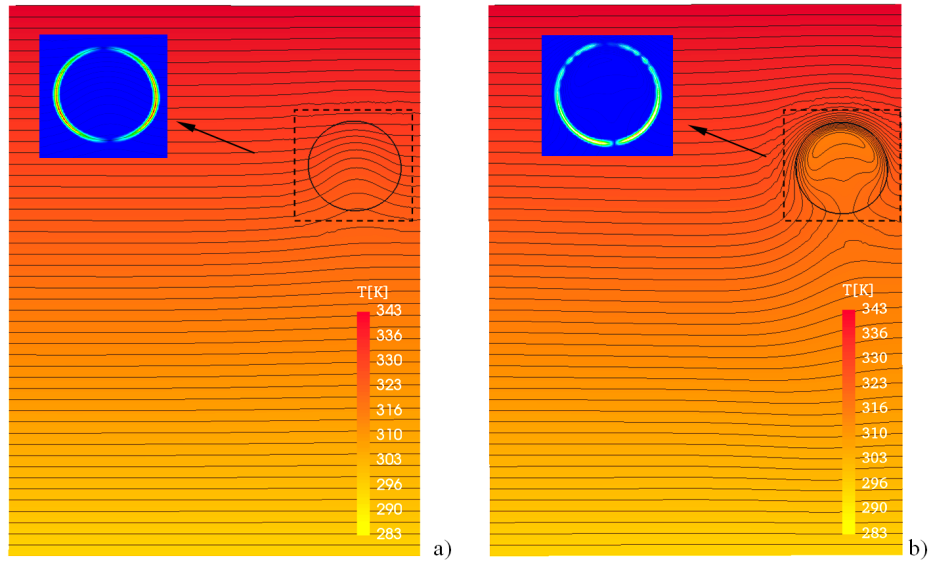
Figure 4.3: Temperature field and thermocapillary force contours in the "NS_3" case ($e = 0.73$, $\theta = 4.65$) for a) $Ma = 2$, b) $Ma = 100$. For $Ma = 2$, the thermocapillary force varies from a minimum of 0 (blue contour) to a maximum of 0.177 Nm^{-3} in the region of the interface. For $Ma = 100$, the thermocapillary forces varies from 0 to ~ 6.4 Nm^{-3} in the region of the interface.

values of the Marangoni number, however, the distortion of the temperature field due to its interaction with the droplet motion becomes significant and this, in turn, has a back effect on the velocity of the droplet itself (when the droplet is located close to the wall, such a proximity has an impact on the thermal field, which becomes highly distorted as shown in Fig. 4.3b). As a natural consequence, the distribution of thermocapillary stresses at the droplet surface changes with respect to the case in which the droplet is far from the wall (most remarkably, the resulting Marangoni force is no longer oriented along a direction parallel to the imposed temperature gradient leading to the emergence of an additional droplet velocity component perpendicular to the wall boundary as shown in Figs. 4.4 and 4.5). Hence, as the Marangoni number increases there are two different factors contributing to the decrease in velocity experienced by the droplet, one of purely viscous nature and another of a thermal origin. Interestingly, Fig. 4.5 shows an apparently oscillatory behaviour, which may indicate the onset of an instability (expected to be driven by the interplay between kinematic and shape deformation effects). This might be the subject of a future work entirely devoted to addressing such aspects, which are beyond the scope of the present study.

97
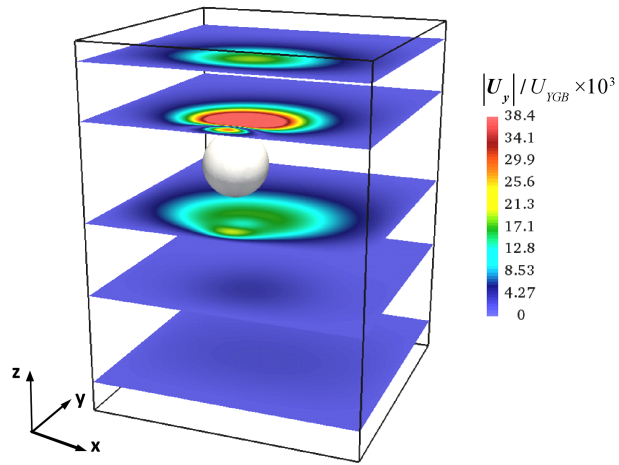
Figure 4.4: 3D view of the scaled y-velocity component in the "NS_3" configuration for $Ma = 100$ showing five different xy-planes taken at a distance of ~ 1.2 cm of distance between each other.
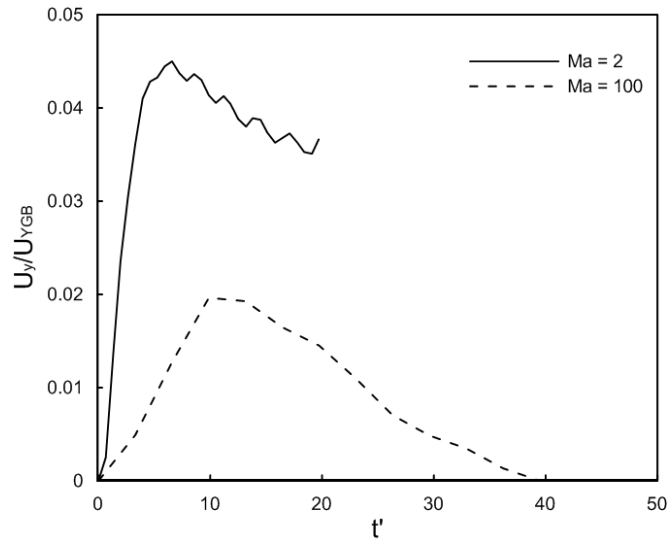
Figure 4.5: Time evolution of the droplet y-velocity component normalised with the Young limit for the "NS_3" configuration at $Ma = 2$ and $Ma = 100$. Note that the numerical value is larger in the case of $Ma = 100$ compared to that at $Ma = 2$.

4.2.2 Proximity to a corner

Since in a parallelepipedic domain, in principle, a drop may transit in a region located near the intersection of two adjacent walls (i.e., close to a corner), in the remainder of this section we expressly concentrate on such a case. In order to do so, we release the drop from an initial position constrained by two adjacent walls (indicated as case "NC" in Fig. 4.1b); because the z-axis is the axis of droplet motion, in practice, this is equivalent to considering an equal "off-set" parameter in both x- and y-directions. The migration velocity for the "NC" configuration is compared with previous cases with $e = 0$ (Sect. 3.5.2) and $e = 0.73$ and are shown in Figs. 4.6 and 4.7, for a range of Marangoni numbers. Fig. 4.6 provides the scaled droplet speed as function of the dimensionless time for three different configurations and several values of the Marangoni number. The most interesting
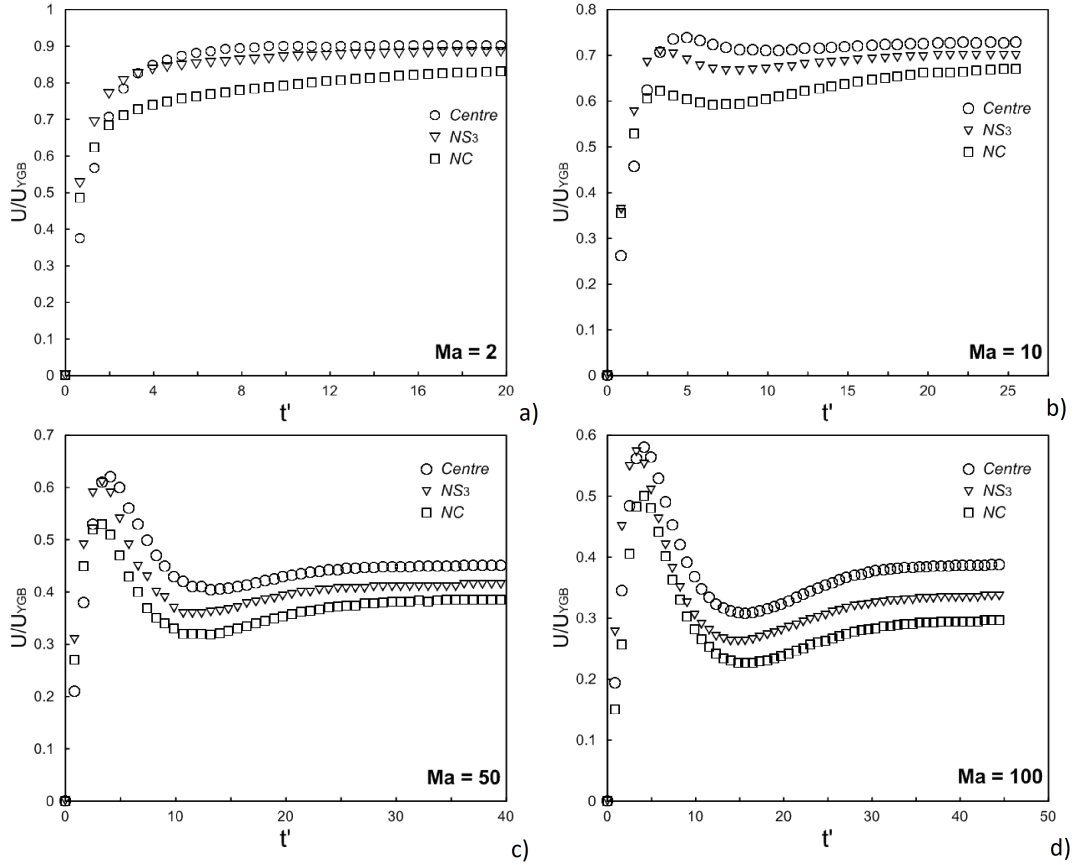
Figure 4.6: Time evolution of the droplet velocity normalised with the Young limit for the three configurations: $e = 0$ ("centre"), $e = 0.73$ along the y-axis ("NS_3") and $e = 0.73$ along both x and y axis ("NC"): a) $Ma = 2$, b) $Ma = 10$, $Ma = 50$, $Ma = 100$.
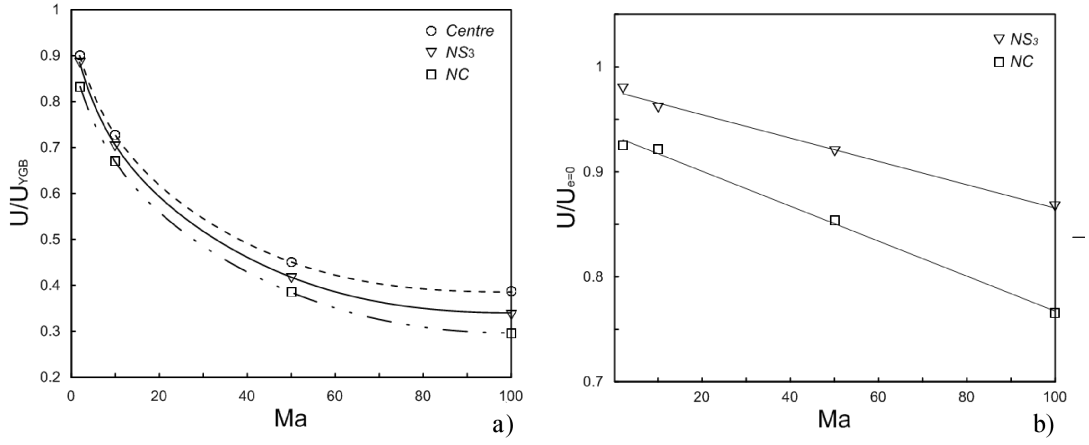
Figure 4.7: Effect of the Marangoni number on the scaled migration velocity for $e = 0$ (centre) and $e = 0.73$ ("NS_3" and "NC"): a) migration velocity normalised with the Young limit, and b) migration velocity normalised with its counterpart for $e = 0$, for different Marangoni numbers ($Ma = 2, 10, 50, 100$).

information in these figures is the evidence they give about the enhanced droplet "slow down" effect when the droplet "feels" the presence of two distinct (adjacent) walls. Such behaviour can be justified considering the wall-induced distortion of the temperature field (as explained in Sect. 4.2.1). As a consequence the droplet experiences a lift force, which "pulls" it away from the boundary with a certain velocity. In this case, part of the available "driving force" is used to displace the droplet from the wall (instead of accelerating it in the direction of the imposed temperature difference). This interpretation is further confirmed in
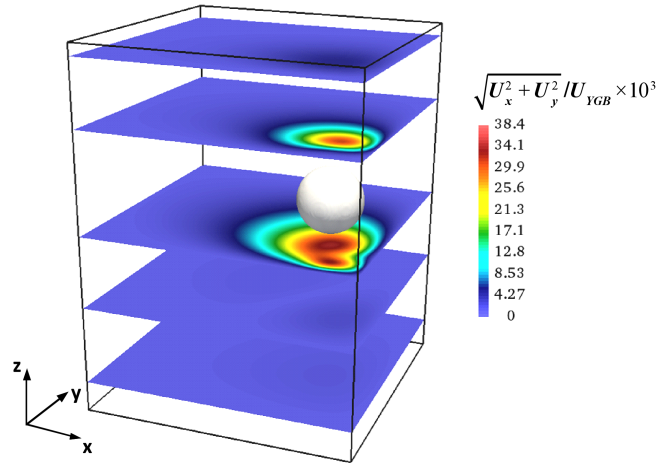
Figure 4.8: 3D view of $\sqrt{U_x^2 + U_y^2}/U_{YGB}$ for 5 different xy-planes taken at ~ 1.2 cm intervals for the "NC" configuration for $Ma = 100$.

100

Fig. 4.7 where the asymptotic migration velocity of the droplet-near-corner case ("NC", $e = 0.73$), normalised by its counterpart at $e = 0$ has been reported as a function of the Marangoni number. It can be noticed that the distance between the two trends (segments shown in Fig. 4.7b) attains a minimum for $Ma = 2$ (where the decrease in the velocity can be ascribed only to viscous effects) and increases with the Marangoni number due to the aforementioned thermal effect. A 3D view of the scaled velocity magnitude $\sqrt{U_x^2 + U_y^2}/U_{YGB}$ (considering the velocity components in a plane perpendicular to the temperature gradient) for $Ma = 100$ is shown in Fig. 4.8.

4.2.3 Effect of the thermal boundary conditions: adiabatic vs conductive walls

In Sect. 4.2.1 we considered the migration of the droplet near a wall assuming perfectly adiabatic conditions. In order to assess the role potentially played by the thermal boundary condition assumed at the walls, additional simulations (here, we considered only the "NS_3" configuration) have been performed replacing the adiabatic conditions with an alternative condition valid in the opposite limit in which the boundaries behave as purely conducting walls (while from an experimental standpoint, adiabatic conditions would be maintained only by an exceptionally insulating material, conducting conditions can be easily implemented in experiments by using walls made of a metal). To study such an effect, we have imposed a constant linear temperature distribution on the boundaries (in practice, the same linear profile established at the beginning of the calculation) and performed new simulations for the case at $Ma = 2$ and $Ma = 100$.

Figures 4.9a and 4.9b show the normalised droplet velocity and normalised distance from the wall relative to that evaluated at the initial time for both the "adiabatic" and "conducting" cases). As evident in these figures, when the convective transport of energy is negligible ($Ma = 2$), the difference between the two cases is limited to a quantitative modification of the droplet velocity. In both situations the droplet moves further away from the wall with a velocity that is roughly constant, thus the droplet describes a linear trajectory. However, the

velocity component that "pulls" the droplet away from the wall is smaller than that for the adiabatic-wall case (as witnessed by the different terminal velocity and the different inclination of the related trajectory in Figure 4.9a and in the trajectories illustrated in Fig. 4.10 (left)). The differences become much more
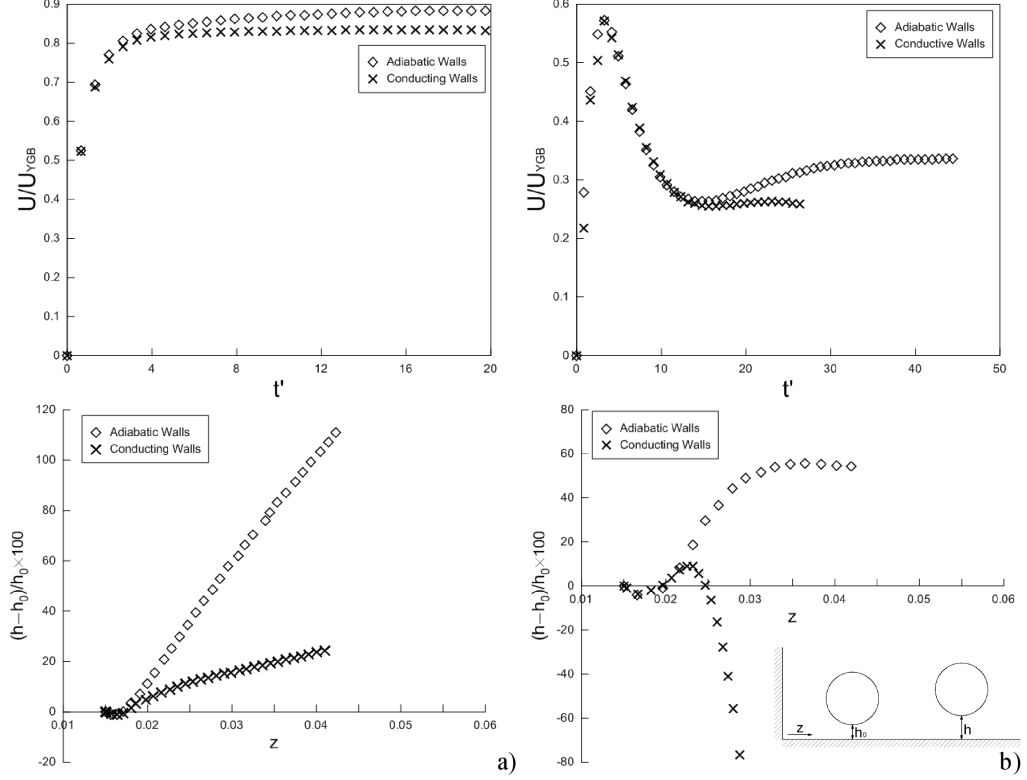
Figure 4.9: Normalised droplet velocity (top) and distance from the wall relative to the initial drop position (bottom) considering both "adiabatic" and "conductive" walls at $Ma = 2$ (a) and $Ma = 100$ (b) for the configuration "NS_3".

striking for $Ma = 100$, with the dynamics exhibiting different trends according to the thermal boundary condition considered. For the adiabatic wall, the droplet initially follows a linear trajectory that is qualitatively similar to the one observed for the case $Ma = 2$, then the normal velocity component vanishes and the trajectory becomes roughly parallel to the wall. By contrast, in the conducting-wall case, the droplet initially moves away from the side, but at a certain stage the velocity component perpendicular to the boundary reverses its sign. When this happens, the droplet starts to move very quickly towards the wall until the collision is observed. These behaviours are driven by the prevailing temperature gradient across the droplet and related distribution of thermocapillary stresses.

102

This gradient has two distinct components, namely an axial component (causing the droplet to migrate from the cold wall to the hot wall) and a "perpendicular" component induced by the droplet interaction with the wall and related thermal conditions. As revealed by the simulations, for $Re \to 0$, i.e., $Ma = 2$, a change in the nature of the thermal boundary conditions does not lead to qualitative modifications in the behaviour of the droplet (indeed, for such conditions the departure of the temperature field from linear diffusive conditions is almost negligible regardless of the thermal conditions at the wall). Nevertheless, for $Ma = 100$, the assumption of conducting wall causes a sign reversal in the component of the temperature gradient perpendicular to the solid boundary.

Such behaviour can be clarified by observing the distribution of the isotherms (that in turn affect the thermocapillary stresses) shown in Fig. 4.10 (top). When the wall is adiabatic, the isotherms are symmetrically distributed around the axis ξ of the drop and consequently the Marangoni stresses are also roughly symmetric and the resulting integral is a vector that points toward the direction of the axis of symmetry of the droplet (cf. the vector $\boldsymbol{F}_{MS}$ at the bottom of the same figure). In the presence of a conductive wall, on the contrary, the thermocapillary stresses are no longer symmetrically distributed because the temperature field in the area near the wall is different from that established on the opposite side. In particular, we can imagine to subdivide the droplet in three different regions: an "upper" area, away from the wall (region I as shown in Fig.4.10), and two "bottom" areas near the wall (region II and III). We notice that in the upper part the temperature field is similar to that established in the case with adiabatic conditions. The lower parts, however, are considerably different. In region II the isotherms tend to "embrace" the surface of the droplet as a consequence of the temperature of the wall being imposed. Consequently, in that area the temperature gradient is mainly directed perpendicularly to the interface and has a strong component perpendicular to the solid wall as well. This gradient obviously gives only a small contribution in terms of thermocapillary stresses. On the contrary, in region III the isotherms are distributed roughly normally to the interface, therefore their contribution to the thermocapillary stresses is maximised (in this case the tem-
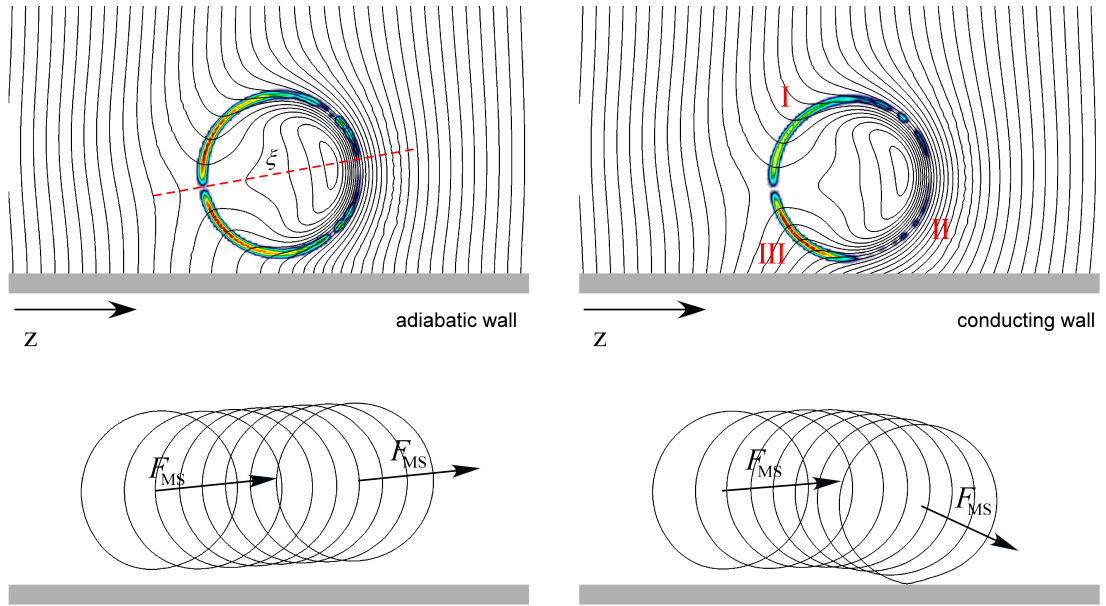
Figure 4.10: Comparison between the thermal field with superimposed thermocapillary stresses around the droplet (top) and trajectories (bottom) in the "NS_3" configuration and $Ma = 100$ in the case of adiabatic and non-adiabatic walls.

perature gradient is mainly directed tangentially to the interface). This uneven stress distribution is responsible to the occurrence of a net force with a component directed toward the surface (see the vector $\boldsymbol{F}_{MS}$ depicted in the bottom figure) that eventually causes the droplet to approach the boundary.

In the case of an actual experiment, where the side walls are expected to behave intermediately between the two ideal conditions considered here, one may expect the droplet to behave in a manner somehow intermediate, depending on the effective thermal flux established between the fluid and the external environment and the relative droplet-wall distance.

4.3   Effect of domain configuration: converging and diverging geometries

In this section, we consider a set-up similar to the previous parallelepipedic container, but with the widths of the square cross-section decreasing (converging case) or increasing (diverging case) linearly along the domain from the cooled to the heated wall. Accordingly, we define the average container width $\bar{w}$ as
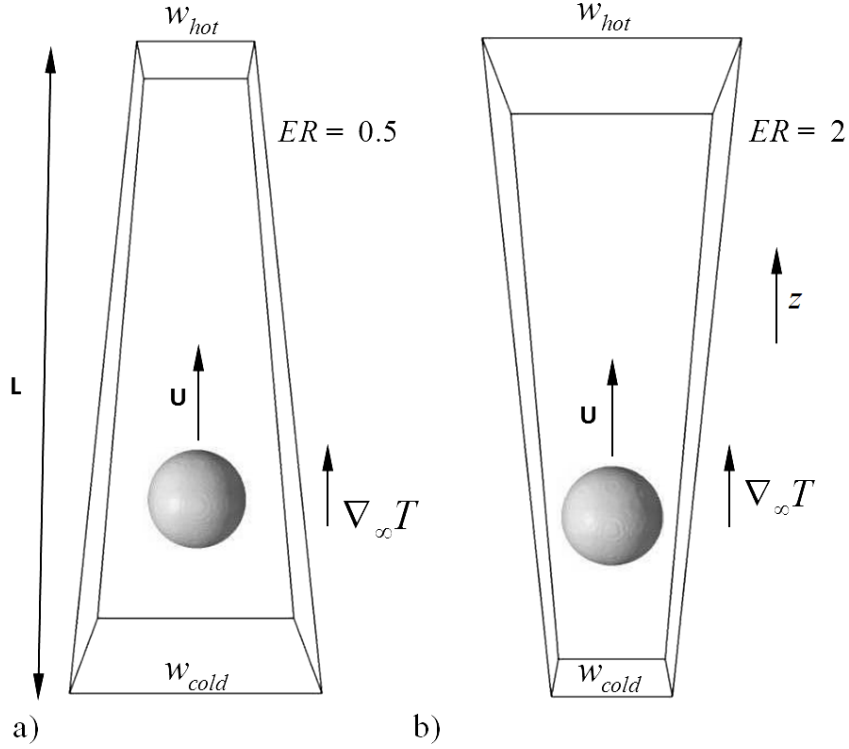
Figure 4.11: Schematics of the container with converging a) and diverging b) adiabatic side-walls.

$\bar{w} = (w_{hot} + w_{cold})/2$ where w_{hot} and w_{cold} are the dimensional widths of the hot and cold side, respectively. The overall system aspect ratio (AR), in turn, is introduced as its length-to-average-width ratio ($AR = L/\bar{w}$) (refer to Fig. 4.11). Another relevant characteristic geometrical parameter is the expansion ratio $ER = w_{hot}/w_{cold}$, which can be greater than 1 (diverging geometry) or smaller than 1 (converging geometry), while for $ER = 1$ one would recover the classical case with parallel boundaries considered in earlier sections. Such cases are of special interest because it might be argued in advance that for such containers the temperature field has to play a significant role even under creeping flow conditions. In such a context, before starting to deal with the droplet migration problem, it is instructive to consider the behaviour of the temperature field in the limit as $Re \to 0$. For such a case, indeed, an analytic solution can be found for the temperature field. Our interest in such an expression stems from a two-fold purpose. First, it can be used to show that the assumption of linear temperature increase along the vertical (z-axis) valid in the case of straight containers with

uniform cross-section, no longer holds. Second, such an analytical expression can be used as a relevant initial condition to accelerate the convergence of the algorithm relating to the numerical solution of the momentum and mass conservation equations in the more general case for which both Re and Ma have finite values and $ER \neq 1$.

Most conveniently, we start from the balance of energy cast in its simplest form, that is, the conservation of energy flux along the vertical direction:

$$w^*(z)\frac{dT^*}{dz^*} = c_1 \tag{4.2}$$

where $T^* = (T - T_{cold}) / (T_{hot} - T_{cold})$ in this context is the non-dimensional temperature , T is the dimensional temperature and $w^*(z^*)$ is the nondimensional extension (using the average width $\bar{w}$ as reference length) of the generic cross section, which in turn can be expressed as:

$$w^*(z^*) = w^*_{cold} + \left[\frac{w^*_{hot} - w^*_{cold}}{AR}\right] z^* = w^*_{cold}\left[1 + (ER - 1)\frac{z^*}{AR}\right] \tag{4.3}$$

Substituting Eq. (4.3) into Eq. (4.2) gives:

$$\frac{dT^*}{dz^*} = \frac{c_1}{w^*_{cold}\left[1 + (ER - 1)z^*/AR\right]} \tag{4.4}$$

which, once integrated, yields

$$T^*(z^*) = \frac{c_1 AR}{w^*_{cold}(ER - 1)} \ln\left[1 + (ER - 1)z^*/AR\right] + c_2 \tag{4.5}$$

The two constants c_1 and c_2 can be determined forcing Eq. (4.5) to satisfy the boundary conditions at the two sidewalls, namely

$$(z^* = 0, \ T^* = 0) \ \rightarrow \ c_2 = 0 \tag{4.6}$$

$$(z^* = AR, \ T^* = 1) \ \rightarrow \ c_1 = \frac{w^*_{cold}(ER - 1)}{AR\left[\ln(ER)\right]} \tag{4.7}$$

Accordingly, Eq.(4.5) can be cast in compact form as

$$T^*(z^*) = \frac{\ln\left[1 + (ER - 1)\, z^*/AR\right]}{\ln(ER)} \tag{4.8}$$

where, obviously

$$\lim_{ER \to 1} \frac{\ln\left[1 + (ER - 1)\, z^*/AR\right]}{\ln(ER)} = \frac{z^*}{AR} \tag{4.9}$$

The temperature profiles obtained from Eq. (4.8) (see Fig. 4.12) for different
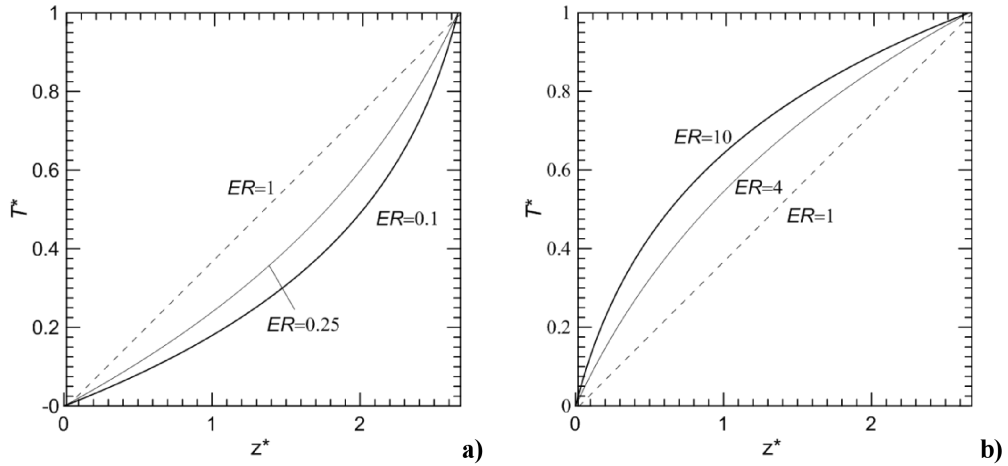
Figure 4.12: Exact solution for the temperature profile for $AR = 2.66$ and $Re = 0$ (a dashed line is used for the corresponding ideal linear temperature profile obtained for $ER = 1$): a) $ER < 1$ (converging walls); b) $ER > 1$ (diverging walls).

values of the parameter ER clearly show a departure from the purely linear distribution of the temperature profile theoretically established for $ER = 1$. The resulting profile is concave or convex for $ER < 1$ or $ER > 1$ respectively.

Fig. 4.13a shows the numerical results in the case of creeping flow (vanishingly small Marangoni and Reynolds numbers) for a converging and a diverging geometry with aspect ratio $AR = 2.66$ together with the related results for the corresponding straight geometry ($ER = 1$ to be used for comparison). The latter is considered for three different values of the confinement parameter: $\theta = 0.286$ (which corresponds to the geometry used in the experiments by Hadland et al., (1999)), $\theta = 0.42$ and $\theta = 0.8$. For both converging and diverging geometries, the parameter θ, evaluated using the larger side as a reference is assumed to be $\theta = 0.8$. The interpretation of the results shown in Fig. 4.13 is not as straight-

107
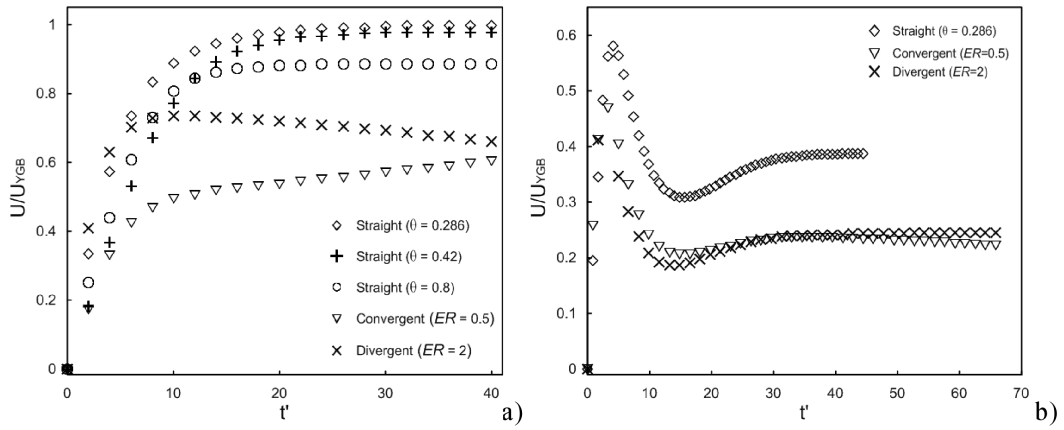
Figure 4.13: Time evolution of the scaled droplet migration velocity for converging and diverging geometries (aspect ratio $AR = 2.66$): a) in the limiting case of creeping flow (the flow conditions are the same as those considered in Sect. 3.5.1) compared to the droplet velocity for a "straight" geometry and different confinements; b) for $Ma = 100$ compared to the "straight" geometry used in the experiments of Hadland et al. (1999).

forward as first expected. On the basis of purely kinematic considerations, in the limit as $Re \to 0$, one would expect the droplet to undergo deceleration in the converging channel case, and vice versa for the diverging channel, due to the frictional increased or reduced influence of walls, respectively.

Fig. 4.13a shows just the opposite trend: droplet velocity increasing for a contracting geometry and decreasing when there is an expansion of the cross section (later, the droplets converge to a similar speed). Such a counterintuitive scenario, however, can be justified on the basis of the arguments provided earlier about the behaviour of the temperature field in such geometries in the case $Re < O(1)$. In such circumstances, the initial diffusive temperature profile is not significantly modified or disturbed by the migration of the droplet. As the temperature profile is convex for $ER > 1$, the gradient is initially larger than that established in the case with $ER < 1$ (see Fig. 4.12b) and this makes the droplet velocity (at least in an initial stage) higher than the corresponding migration velocity of the droplet in the geometry with converging walls (Fig. 4.13a). Since for this case the temperature gradient decreases as the droplet moves through the channel, its velocity progressively decreases accordingly. These trends are reversed for the case with converging walls (concave temperature profile, Fig. 4.12a). The temperature gradient is initially relatively small and it then increases as the droplet
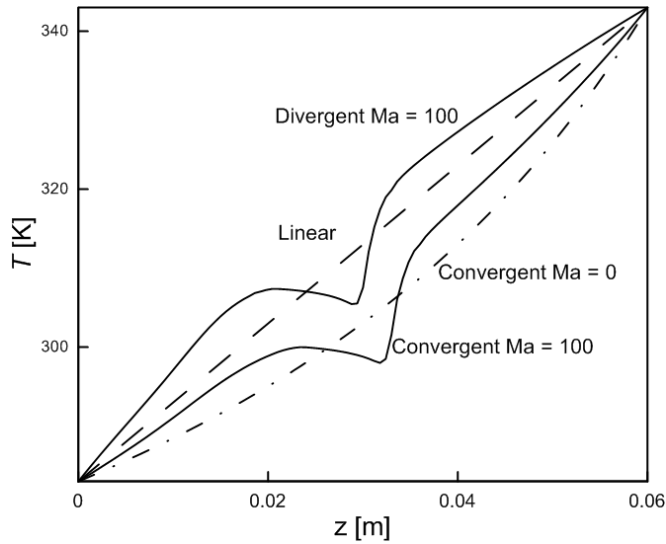
Figure 4.14: Dimensional temperature profile along a line crossing the geometry in the middle of the channel for the converging ($ER = 0.5$) and diverging ($ER = 2$) geometries at $Ma = 100$ (solid lines), and temperature distribution for the convergent and box-shaped domains at $Ma = Re = 0$ (dashed lines).

moves from the cold wall towards the hot one. This causes an acceleration of the droplet (Fig. 4.13a) (curve at $Ma = 0$ for the case $ER = 0.5$). A considerable different behaviour occurs when the convective transport of energy becomes more important. Figure 4.13b shows the temporal evolution of the migration velocity for the two geometrical configurations under discussion when $Ma = 100$ (in the same plot we have also included the results about the straight channel for comparison). It can be seen that the two trends are qualitatively similar up to a dimensionless time $t' = 40$ (even though in the case $ER = 0.5$ the velocity is always slightly higher). Most notably, after this instant the velocity of the droplet which is migrating within the converging channel starts to decrease at a constant rate (vice versa it was increasing in the case $Re < O(1)$).

This behaviour can be explained by observing that, while for $Re < O(1)$ the temperature gradients were the main "drivers" determining the droplet behaviour, we are now in the presence of several distinct effects. Along these lines, it is instructive to begin the related discussion by examining Fig. 4.14, which shows the temperature distribution on a segment passing through the centre of the domain for the two cases under discussion (in addition the "undisturbed" linear profile in the case of the straight channel and the profile for the converging channel

109

when $Re \rightarrow 0$ are also included). It can be seen that the temperature gradients in front of the drop for the case $ER = 0.5$ are higher than those established in the case $ER = 2$, as it was observed for $Re < O(1)$; it can be noticed as well, however, that the temperature profiles are no longer logarithmic, and the differences in the gradients are much less pronounced than those seen for $Re < O(1)$. This is also witnessed by the temperature fields shown in Fig. 4.15a (taken at the corresponding dimensionless time $t' = 40$). Although the isotherms tend to be more condensed near the front of the drop in the case of converging geometry (which means that they give rise to larger Marangoni stresses), the related patterns for the converging and diverging geometries are qualitatively similar.

These mechanisms, however, are not the only at play in the considered dynamics. For the case $ER = 0.5$, as the droplet is forced to move through a converging geometry, at a certain stage it will feel an increasing effect of blockage due to the presence of the approaching walls. On the contrary, the scenario in the diverging channel is exactly the opposite: while the thermocapillary stresses are smaller because of the smaller temperature gradients, the droplet moves through a channel that offers a decreasing effect of blockage. In light of these arguments, the similar trends of the migration velocity visible in the central part of the channel in Fig. 4.13b can be ascribed to these two compensating effects (in the second portion of the domain the two influential factors still "counteract": in the converging arrangement the propulsive temperature gradient and the blockage effect become increasingly larger while in the diverging geometry the opposite applies). To further clarify these aspects, Fig 4.15b shows the temperature gradient profiles along z. Near the interface (corresponding to the vertical dashed lines shown in Fig. 15b) the temperature gradients are fairly similar because of the development of a thermal boundary layer in the front region and a thermal "wake" in the rear region; analogous considerations apply in the rest of the interface. It can be seen how the main thermal convection affects the temperature gradients at the droplet surface to make it less dependent on the value of the parameter ER relative to the scenario seen for $Re \rightarrow 0$. The differences between the temperature gradients for
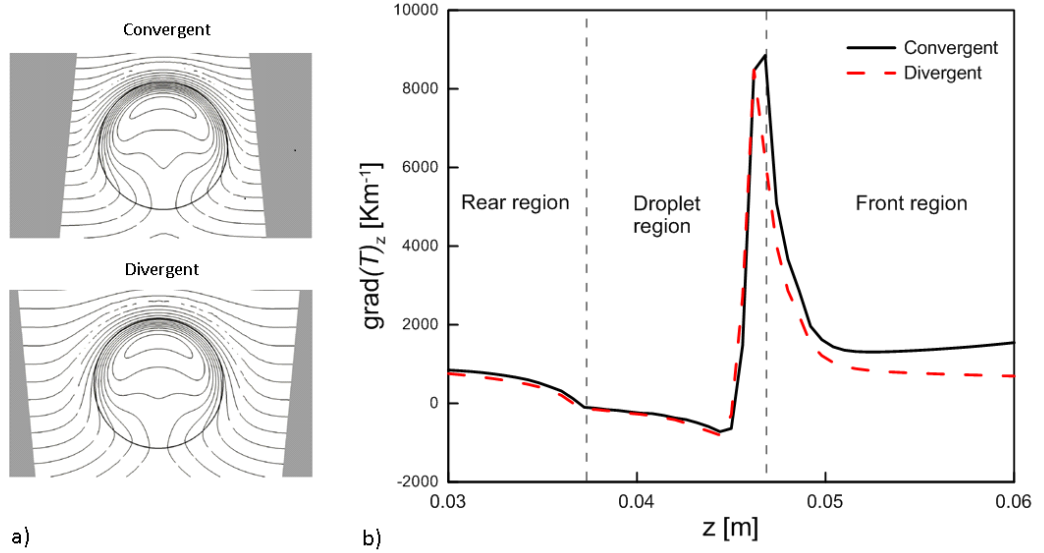
Figure 4.15: a) Temperature distribution near the region of the droplet for the diverging and converging channels when $Ma = 100$ at $t' \sim 65$, b) Temperature gradient component evaluated along the line crossing the channel through its centreline.

$ER < 1$ and $ER > 1$ are now less pronounced and, accordingly, the velocity evolutions are relatively similar in the central region of the channel. After a certain stage, however, the effect of blockage in the case $ER = 2$ becomes predominant and the droplet velocity inevitably starts to decrease.

In summary, while for $Ma = O(1)$ $(Re < O(1))$ the difference between the straight geometry and the two cases with $ER \neq 1$ have to be ascribed essentially to thermal effects, in the case $Ma = O(100)$ $(Re = O(1))$, the effects of a non-linear temperature distribution are partially mitigated by the presence of thermal convection, which results in a similar temperature distribution around the droplet regardless of the value of ER, thereby making blockage effects more influential in determining the velocity evolution.

4.4 Conclusions

The effect of the wall-droplet interaction and domain shape on the thermal Marangoni migration of droplets has been analysed in three-dimensional geometries using a coupled LS-VOF approach implemented in the framework of the OpenFOAM computational platform. We have studied several geometrical con-

figurations, for different Marangoni numbers: droplet released in the proximity of a single adiabatic or purely conducting wall ("NS" configuration) and droplet released in proximity of two adjacent adiabatic walls (i.e., close to a corner, "NC" configuration). Moreover, the effect of the geometry shape has been accounted for considering the motion of the droplet in converging and diverging containers. All the computations have been performed allowing the Marangoni number to span a relatively wide range, with the extremes of such an interval corresponding to the situation of "creeping flow" (in which thermal effects are expected to play a negligible role) and a situation in which $Re \geq O(1)$ (Ma up to 100 for which significant distortions in the temperature field are expected).

In the case of the wall-droplet interaction for adiabatic conditions, the results show that for both configurations ("NS" and "NC") the migration speed decreases with the Marangoni number when compared to the velocity one would observe for the droplet migrating in the centre of the channel. In addition, we have also noticed the presence of a velocity component directed along the direction perpendicular to the wall, which tends to "pull" the droplet away from the wall. We infer that such a velocity component is the result of wall-induced distortions present in the temperature field with increasing magnitude as the Marangoni number is increased (such distortions being weak or negligible when Re < O(1) where the only mechanism responsible for the droplet slowdown is of a viscous nature).

In the case of the interaction with a conducting wall ("NS_3" configuration), the results have revealed that the migration process is strongly sensitive to the value of the Marangoni number. More specifically, for $Ma = 2$ the scenario remains substantially unchanged with respect to the case with adiabatic walls, the main difference being related to a relatively small decrease in the velocity component that pulls the droplet away from the boundary. For $Ma = 100$ however, the distortion of the temperature field in the region between the droplet and the wall in the case of conducting sidewalls results in a uneven distribution of the thermocapillary stresses that is responsible for the occurrence of a net force with a component directed toward the surface (pulling the droplet towards the wall i.e.,

in the opposite direction with respect to that observed for adiabatic conditions).

With regard to the effect of the shape of the domain, our numerical experiments have revealed apparently counterintuitive results. For adiabatic sidewalls and $Re < O(1)$ the temperature profile is essentially logarithmic (in line with the analytic solutions that can be obtained integrating the energy equation in the absence of convection) and the droplet undergoes acceleration or deceleration depending on the concavity of such a profile for $ER \neq 1$. When $Re = O(1)$, however, the differences between the cases $ER < 1$ and $ER > 1$ in terms of temperature gradients are mitigated by the presence of strong thermal convection inside and around the droplet. Accordingly, the velocity displayed by the droplet in the two cases is relatively similar until blockage effects (due to the narrowing channel for the case $ER > 1$) start to play a dominant role in the dynamics.

Chapter 5

Thermocapillary motion of a Newtonian drop in dilute Viscoelastic fluids – A numerical approach

5.1 Introduction

All the simulations presented so far have been carried out considering Newtonian phases. Nevertheless, many fluids encountered in engineering and scientific applications may show non-Newtonian behaviour. There is indeed a large body of literature dedicated to the study of the motion of bubbles and drops in the presence of non-Newtonian fluids (see, e.g., Chhabra, 2006 for a detailed review), owing to its relevance for engineering applications (often, the manipulation of different fluid phases for industrial purposes involve non-Newtonian fluids), and to the variety of unexpected, and, in some cases, not yet fully understood features that viscoelastic effects might confer to the motion and shape of deformable fluid particles. Among the diversity of non-Newtonian effects that might be encountered, viscoelasticity is arguably one of the most interesting.

The first documented experimental investigation on the motion of bubbles in viscoelastic fluids can be attributed to Philippoff (1937) who investigated the motion of air bubbles rising through elastic solutions made of rubber dissolved in organic solvents. The experiments revealed that the bubbles assumed a characteristic tear-like shape with the presence of a trailing cusp which was observed to become more pronounced when the relaxation time of the fluid was increased. For such reason, the behaviour was attributed to the presence of time-dependent effects. Subsequently, similar problems have been investigated by a number of other

authors (see, e.g., Warshay et al. 1959, Mhatre and Kintner, 1959, Astarita and Apuzzo, 1965, Calderbank, 1967, Calderbank et al. 1970, Zana and Leal, 1978 and Hassager, 1979). In particular, Hassager (1979) was the first to realise that the cusp might not be axisymmetric even though the flow conditions were such that there was no apparent motivation to predict such asymmetry. Later, Liu et al. (1995) conducted systematic experiments considering air bubbles rising through viscoelastic solutions in containers having different cross-sections (i.e., rounded, squared and rectangular) and discovered that the trailing cusp might actually assume a variety of different shapes. Another interesting phenomenon that can be observed on the motion of both solid and fluid particles translating in a viscoelastic liquid, is the presence of a "negative wake" (Hassager, 1979) (cf. Fig. 5.1). The term 'negative' originates from the fact that although very close to the rear stagnation point the velocity is in the direction of the particle motion, immediately further away from the trailing end the flow reverts direction. When the continuous phase is Newtonian, on the contrary, the velocity in the wake is everywhere in the same direction of the motion of the particle.
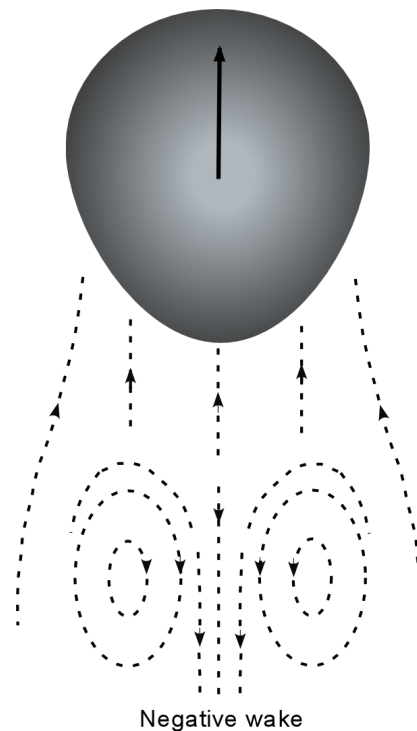
Negative wake

Figure 5.1: Illustration of the negative wake behind a bubble moving in the upward direction.

Lastly, it is worth mentioning another interesting phenomenon which has at-

tracted the attention of a number of scientists throughout the past decades and that is still not yet entirely understood. It is well documented that when the volume of a bubble surrounded by a viscoelastic fluid exceeds a certain critical value, the rising velocity might increase abruptly (Astarita and Apuzzo, 1965). A similar phenomenon can also be encountered for Newtonian fluids, but the typical velocity jump is less steep and is attributable to the transition from "no-slip" conditions (when the bubble is very small) to shear-free conditions (see, e.g., Chhabra, 2006). In the presence of a non-Newtonian phase however, the sudden jump seems to be ascribed to a number of concomitant phenomena (in addition to the above mentioned transition from no-slip to shear-free regime) such as shear thinning effects (Zana and Leal, 1978), shape deformations (Liu et al. 1995, Pillapakkam et al, 2007) and possible presence of surfactants. Furthermore, Herrera-Velarde et al. (2003) observed that the phenomenon is associated to the presence of the negative wake, which seems to appear only after the bubble has reached the critical volume. Although there is a certain consensus on attributing the phenomenon under discussion to all these mechanisms discussed before, to date it is not yet possible to predict a priori the extent of the velocity increment or whether such a discontinuity will occur or not in a new experiment.

Despite the fact the mechanism responsible for the particle motion considered in this thesis is considerably different from the one mentioned before, it is reasonable to assume that in the presence of a viscoelastic continuous phase and under certain flow conditions, similar non-Newtonian behaviour can also be expected for the thermal migrations of a bubble or a drop. Although there is a relevant amount of literature dedicated to the study of thermocapillary flows of fluid layers in the presence of viscoelastic fluids (see, e.g., Getachew and Rosenblat, 1985; Martinez-Mardones and Perez-Garcia, 1990; Parmentier et al. 2000; Hu et al. 2018), the non-Newtonian thermocapillary problem for bubbles and drops seems to be relatively unexplored. The analytical solution of Jiménez-Fernández and Crespo (2002) mentioned in the introductory chapter appears to be the only work known to the author of this thesis which add some details that are relevant for the present work.

With the intent to investigate the role potentially played by the presence of elasticity on the thermocapillary motion of drops, in this chapter we present numerical computations obtained assuming absence of convective phenomena, i.e., for vanishingly small Re and Ma, considering a Newtonian drop embedded in a viscoelastic continuous fluid. In order to avoid further complications that might arise from the presence of shear thinning effects, the problem has been tackled adopting two different constant viscosity models (i.e., Oldroyd-B and FENE-CR models) which have been adopted for different ranges of Deborah numbers due to the limitations on solving the Oldroyd-B model (cf. Sect. 2.3.1) imposed by the presence of a straining flow localised next to the rear stagnation region of the drop.

5.2   Statement of the problem

We consider here the thermocapillary incompressible flow of a Newtonian droplet surrounded by an unbounded immiscible viscoelastic liquid assuming negligible convective transport and absence of gravitational effects. The droplet is deformable and is assumed to have the same volume of an equivalent sphere of radius R. The outer viscoelastic phase is characterised by a constant zero-shear viscosity, $\eta_{0,m} = \eta_{s,m} + \eta_{p,m}$, given as the sum of a Newtonian (solvent) contribution, $\eta_{s,m}$, and a viscoelastic (polymer) contribution, $\eta_{p,m}$. The droplet viscosity is indicated with the symbol, η_d. Similarly to the cases discussed so far, a constant temperature gradient, $\nabla_{\infty}T$, is maintained by external means. Assuming that the interfacial tension, σ, decreases with the temperature with a rate of change $\sigma_T = d\sigma/dT < 0$ (assumed constant in the present study), the droplet will translate along the positive direction of the imposed thermal gradient.

Using the same considerations discussed in Sect. 3.2 (i.e., by labelling the variables with the subscripts "m" and "d" to distinguish the two phases) one can obtain a set of dimensionless parameters formally identical to the one introduced in Sect 2.4, i.e., the Reynolds number, $Re = \rho R U_T / \eta_{0,m}$, the Marangoni number, $Ma = \rho c_{p,m} R U_T / \kappa_m$, the Capillary number, $Ca = \eta_{0,m} U_T / \sigma$, and the thermal

Deborah number, $De_T = \lambda U_T/R$ (notice that no subscript has been added to the relaxation time, λ, since it is understood that this quantity is thereafter defined only for the continuous phase).

Under such assumptions, the complete dimensionless set of governing equation required for the description of the thermocapillary viscoelastic problem considered here can be written as

$$\rho_r Re \frac{D\mathbf{u}}{Dt} = -\nabla p + \nabla \cdot [(1-c)\eta_{0,r}\mathbf{D} + \boldsymbol{\tau}] + \frac{1}{Ca}k\mathbf{n}\delta_S + (\mathbf{I} - \mathbf{nn})\nabla T\delta_S \quad (5.1)$$

$$\rho_r c_{p,r} Ma \frac{D\mathbf{u}}{Dt} = \nabla \cdot (\kappa_r \nabla T) \quad (5.2)$$

$$\hat{d}\mathbf{A} = -\frac{1}{\lambda_r De_T}f\left(\mathrm{tr}\left(\mathbf{A}\right)\right)\left(\mathbf{A} - \mathbf{I}\right) \quad (5.3)$$

$$\boldsymbol{\tau} = \frac{c\eta_{r,0}}{\lambda_r De_T}f\left(\mathrm{tr}\left(\mathbf{A}\right)\right)\left(\mathbf{A} - \mathbf{I}\right) \quad (5.4)$$

Notice that, similarly to the problems discussed in Chapter 3 and 4, we neglect the capillary force arising from the variation of the interfacial tension. Furthermore, we adopted the polymer concentration parameter, $c = 1 - \beta$, rather than β for convenience in the subsequent discussions.

For the solution of the viscoelastic models, we adopted a multiphase version of the *viscoelasticFluidFoam* solver of Favero et al. (2010), kindly provided by the author in a private conversation. To the best of our knowledge, the two-phase adaptation of their code has never been released officially. The original library is based on a stress tensor formulation of the constitutive models, however for our purposes we required the re-formulation of the equations in terms of the conformation tensor, $\mathbf{A}$. The solution procedure of the viscoelastic model remains identical to the one adopted in the original solver of Favero et al. (2010), with the only substantial difference lying on the introduction of Eq. 5.4, which serves to update the stress tensor before solving the momentum equations.

Due to the lack of experimental works devoted to the study of the thermocapillary motion of droplets in non-Newtonian fluids, we assess under which particular circumstances elasticity is likely to play a role.

We consider as an ideal candidate for our viscoelastic phase a Boger fluid

having a relaxation time and total viscosity (both measured in SI units) such that $\lambda/\eta_{0,m} = O(1)$ (notice that these conditions can be achieved experimentally using ad hoc recipes for the preparation of viscoelastic solutions (see, for instance the fluids adopted in the experiment reported in Rothstein and McKinley, 2001)). On the basis of the data available from previous experimental measurements with Newtonian fluids, it is reasonable to assume that the interfacial tension coefficient, σ_T, might vary in a range $\left[10^{-5}, 10^{-4}\right]$ N/mK (for instance, Ross, 1950 reported $\sigma_T = -9.89 \times 10^{-5}$N/mK for the surface tension coefficient of glycerol, while Hadland et al., reported $\sigma_T = -3.6 \times 10^{-5}$N/mK for the interfacial tension between silicone oil and fluorinert). Furthermore, typical values of the temperature gradient $\nabla_\infty T$ range between $O(10^3)$ and $O(10^4)$ K/m (larger values are expected for small scales applications), thus, De_T is expected to be in the range between $O(10^{-2})$ and $O(1)$.

Additionally, although the hypothesis that material properties do not change significantly with the temperature usually holds fairly well for Newtonian fluids (see, e.g., Yin et al. 2012), in the presence of a polymer solution caution should be exercised. In fact, viscosity and relaxation time of a polymer solution changes with temperature following the equation (see, e.g., Rothstein and McKinley, 2001)

$$a_T\left(T, T_0\right) = \frac{\eta_{p,m}\left(T\right)}{\eta_{p,m}\left(T_0\right)} = \frac{\lambda\left(T\right) T}{\lambda\left(T_0\right) T_0} \tag{5.5}$$

where a_T is an exponentially decreasing function which depends on the temperature known as "shift factor". This quantity is usually modelled adopting the so-called WLF equation (Williams et al., 1955) or adopting an Arrhenius-type law (see, e.g., Rothstein and McKinley, 2001)). Due to the exponential nature of a_T, decrements of the relaxation time can be significant in the range of variation of temperature that can be typically encountered in usual experiments (e.g., in the experiments of Hadland, 1999, $\Delta T \simeq 60$ K), therefore the Deborah number can decrease in a significant manner. On the contrary, if we think about microfluidic experiments, large temperature gradient can be established with small temperature differences, and the above mentioned issue should not constitute a

real problem.

5.3   Viscoelastic solver validation

To test the capability of our implementation of the multiphase viscoelastic solver, we analyse the deformation of a two-dimensional droplet subjected to a shearing, inertialess motion either in presence of one, or both viscoelastic phases (see, for instance, the cases discussed in Pillapakkam and Singh, 2001 and in Chinyoka et al., 2005). Here, we compare our results with the numerical findings of Chinyoka et al. (2005).

A circular droplet of radius R is placed at the centre of a domain of height h and width πh (cf. Fig. 5.2) delimited by two parallel walls moving in opposite directions along the x-axis direction with a constant velocity U_0. At the moving walls, we imposed no-slip and no-through flow boundary conditions for the velocity, while the pressure is extrapolated by assigning their values calculated at the neighbour cells centre. At the two lateral boundaries, periodic conditions have been applied. The flow field is initialised by imposing fully developed uniform shear flow in the whole domain (including also the interior of the droplet) and zero viscoelastic stresses (i.e., $\mathbf{A} = \mathbf{I}$). Even though the initial condition for the stresses is not consistent with the imposed velocity field, this does not impact the steady state solution as long as the Capillary number is low enough to guarantee relatively moderate droplet deformations (for more details about this assumption, see Chinyoka et al. 2005). In all the simulations a uniformly spaced mesh having resolution $2R/\Delta x = 50$ has been employed.

The effect of the elasticity on the droplet deformation is studied adopting the Oldroyd-B viscoelastic model. Four different flow configurations have been considered: Newtonian droplet in a Newtonian phase (N-N), viscoelastic droplet and Newtonian matrix phase (V-N) and the other two possible configurations, N-V and V-V. The flow conditions are such that, $Re = \rho_m \dot\gamma R^2 / \eta_{0,m} = 3 \times 10^{-4}$, $Ca = \eta_{0,m} \dot\gamma R / \sigma = 0.24$, $De_i = \lambda_i \dot\gamma = 0.4$, $\beta = \eta_{s,i} / \eta_{0,i} = 0.5$ (the subscript "i" stands for "m" or "d" depending on the flow configuration, i.e., whether the
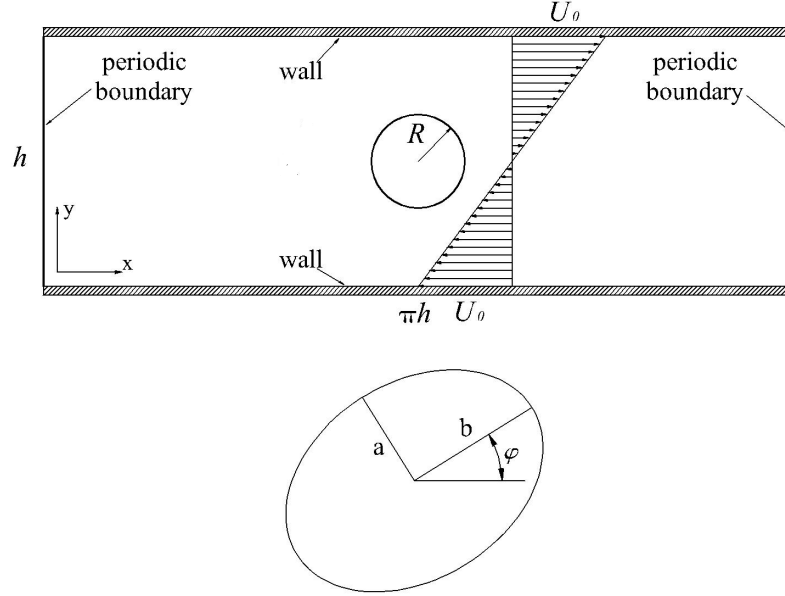
Figure 5.2: Schematic of the domain and initial flow conditions (top) considered for the shear flow test case. Steady state deformed droplet shape (bottom), showing the major and minor axes and the orientation angle φ.

viscoelastic phase is the matrix or the droplet one), where $\dot{\gamma} = 2U_0/h$ is the imposed shear rate. The two fluids are assumed to have the same density and same viscosity (i.e. $\eta_{0,d}/\eta_{0,m} = 1$ and $\rho_d/\rho_m = 1$), while the geometric confinement is set to $R/h = 0.125$, as in Chinyoka et al. (2005).

Fig.5.3 shows the deformation parameter $D = (a - b)/(a + b)$, with a and b being the major and minor axes as indicated in Fig. 5.2, as a function of the dimensionless time, $t' = \dot{\gamma}t$. We compare the results of our simulations (open diamonds) with those of Chinyoka et al. (2005) (open triangles). Apart from a slightly different transient, at the steady state the two set of results are in good agreement with maximum percentage difference about 4%, as shown in Table 5.1. Table 5.1 also highlights the good agreement between the two sets of computations also in terms of the orientation angle φ.
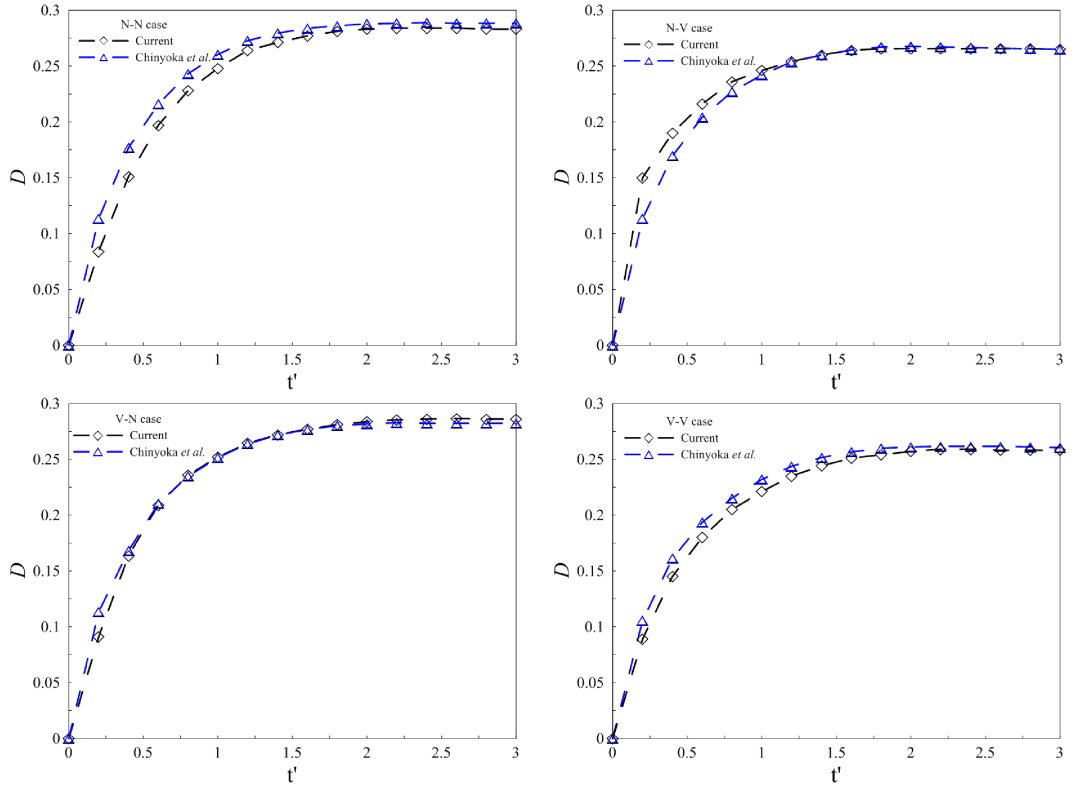
Figure 5.3: Time evolution of the deformation parameter for the different cases considered adopting the Oldryd-B model for the viscoelastic phase. The blue triangles represent the results of Chinyoka et al. (2005), while the current findings are represented by the black diamonds.

Table 5.1: Comparison between pur results and those of Chinyoka et al. (2005) in terms of deformation and orientation angle. Values are taken at steady state.

	Chinyoka et al. (2005)		Current results		Deviation %	
	D	φ [deg]	D	φ [deg]	D	φ
N-N	0.288	32.3	0.283	31.8	< 2	< 2
V-N	0.282	31.2	0.271	31.9	< 4	≈ 2
N-V	0.265	28.2	0.265	28.2	< 1	≈ 0
V-V	0.260	28.2	0.258	29.2	< 1	< 4

5.4 Numerical set-up

In the present work we aim to investigate the role potentially played by elastic effects on the thermocapillary motion of droplet in absence of gravity. In order to accomplish our goal, we ran a series of three-dimensional simulations for a

single Newtonian drop translating in an otherwise stagnant viscoelastic fluid. To investigate a broad range of Deborah numbers, the computations have been carried out by modelling the viscoelastic phase by adopting: a) the Oldroyd-B model, for relatively small Deborah numbers (up to $De_T = 3.75$), b) and the FENE-CR model, for $De_T \geq 3.75$. The reason for this twofold choice is dictated by the presence of a singularity on the solution of the Oldroyd-B model in extensional flows, which in this specific case develops at the rear stagnation point of the drop. Apart from the mesh independency study (see, Sect. 5.4.1), which was performed using 2D grids, all simulations are three-dimensional and have been carried out considering the parallelepipedic computational domain considered for the Newtonian cases discussed in the previous Chapters (i.e., using the same geometric configuration adopted in the experiments of Hadland et al. 1999). We adopt also the same flow conditions as in Sect. 3.5.1, with the only difference that now we account for the elasticity of the continuous phase.

5.4.1 Effect of the grid resolution and time-step

In Chapter 3, it has been seen that in VOF based methods integration in time of the advection equation for the volume fraction using explicit time schemes might impose severe restriction on the maximum Courant number. Additionally, as noted in Sect. 3.4.1, in OpenFOAM the solution of Eq. 3.8 is handled with the MULES method, which is explicit in time. In such an approach, the above mentioned restriction can be partially mitigated by using a time step sub-cycling technique, which essentially allows to split the solution of the advection equation for the volume fraction in a number of user-defined sub-cycles. Roughly speaking, the effective time step employed at each sub-iteration is given by the actual time step divided by the number of prescribed sub-cycles. In addition, the possible occurrence of spurious velocities at the interface should also be taken into account when $Ca \ll 1$. The spurious velocities decrease, in general, by lowering the time integration step, but tend to become larger when the resolution of the grid is increased. Clearly, these issues can impose strict limitations on the time integration step which might drastically increase the overall time of calculation.

In the remainder of this section we will show the effect of the spatial resolution and time step on our computations, and we shall see that the smoothed LS-VOF method employed here allows us to achieve mesh independent accurate results. The time step limitation has been found to be very restrictive as the droplet shape seems to be extremely sensitive to this specification. By setting a sufficiently small maximum Courant number however, the algorithm guaranteed an acceptable prediction of the droplet shape.

Although the adoption of the dynamic grid refinement reduces considerably the computational effort, the mesh and time step study we are about to show would require months of calculation (in comparison to the several days required for a 2D study) to be carried out using the most refined three-dimensional mesh and the smallest time step adopted here. For this reason, the present study was necessarily carried out with an "equivalent" (we set the same geometric constrains in terms of confinement adopted for the 3D geometry of Hadland et al. 1999) two-dimensional configuration. The results then are used to determine the appropriate geometric (mesh size) and time step settings to be employed for the three-dimensional calculations.

The effect of the grid spacing has been assessed for three different mesh resolutions, namely M_1, M_2 and M_3 (as indicated in Table 5.2) considering the Newtonian configuration and setting the maximum Courant number, $Co_{Max} = 0.02$. The time step is already very restrictive, but this was deemed necessary to guarantee acceptable droplet shapes (as discussed below). The results summarised in Table 5.2 show the good convergence of the results in terms of migration velocity. In particular, the relative difference between the cases M_1 and M_3 is already less than 1%, while between M_3 and M_2 is about 0.2%.

The effect of the time integration step has been investigated adopting mesh M_2. We ran different simulations by considering four different values of the maximum Courant number, namely, $Co_{Max} = 0.1$, 0.04, 0.02, 0.01 for both a Newtonian-Newtonian system and a viscoelastic-Newtonian configuration using the Oldroyd-B constitutive equation to model the continuous phase (the parameters adopted for this case are summarised in Table 5.3). As pointed out previously,

124

Table 5.2: Characteristics of the 2D meshes used for the mesh-independence assessment study. The velocity difference is evaluated relatively to the case M_3.

	M_1	M_2	M_3
Nr of cells per droplet diameter	37	56	84
Grid spacing ($\Delta x = \Delta y$)	0.000268	0.0001786	0.0001191
Relative velocity difference at $t' = 40$ [%]	0.437	0.175	

we observed a dependence of the droplet shape on the time step. In order to quantify the magnitude of the deformation relative to the circular shape, we define the droplet aspect ratio, D_a, as the ratio between the droplet major and minor axes, D_1 and D_2 (unlike the case for the shear flow discussed before, where the droplet assumes ellipsoidal shapes, a Newtonian droplet migrating in a viscoelastic fluid can be affected by loss of fore-and-aft symmetry, therefore we found advisable to describe the droplet deformation adopting different quantities), respectively. Table 5.3 shows the values of D_a and the terminal droplet velocity for the four Courant numbers considered. We notice that the departure from the reference circular shape ($D_a = 1$) decreases by decreasing the maximum time step allowable for the simulation. In particular, for $Co_{Max} = 0.1$ the relative percentage deviation from the circular shape is 6.4%, while reaches a minimum value of 0.8% for the smallest Co_{Max}. Additionally, we tested the effect of the grid spacing and noticed that by using a finer mesh, keeping the same maximum Courant number, does not have appreciable influence on the droplet shape. For completeness, we did the same tests also for the viscoelastic configuration. The results indicate a good convergence both in terms of deformation and the terminal velocity, when the time step is decreased (cf. Table 5.2).

In light of these results, we run all the subsequent three-dimensional simulations adopting the mesh M_2 and setting $Co_{Max} = 0.02$, keeping in mind that the shapes we are about to show might be affected by a small (on the order of 1% or less) error. It is also worth mentioning that the effect of the time step used to integrate Eq. 3.8 has also been investigated. In particular, we considered the configuration mesh M_2 and $Co_{Max} = 0.02$ by changing systematically the

number of sub-cycles (in a number of 2, 5 and 10), but no appreciable differences on the shape have been observed, providing the evidence that the droplet shape is insensitive to the time step adopted for the integration of Eq. 3.8.

As an additional remark, it should be reminded that in our implementation we neglected the capillary force term that includes temperature effects. It is reasonable to suppose that this can have an impact on the drop deformation, since the Capillary number adopted here is not exceedingly small (refer to Sect. 6.4.1 for the definition of the criterion necessary to neglect the capillary term under discussion). Nevertheless, the result for the mesh M_3 reported in Table 5.3 is in support of our hypothesis that neglecting such term does not bring to excessively wrong shapes (in such a case, the relative difference with respect to the circular shape is less than 1%).

Table 5.3: Effect of the time integration step on the droplet aspect ratio and terminal velocity. We consider a two-dimensional droplet for a Newtonian case and a viscoelastic case using the Oldroyd-B model. All the simulations have been carried out by employing mesh M_2. The relative difference has been evaluated considering the results obtained for $Co_{Max} = 0.01$ as a reference. *The prolate shape is consistent with the presence of the viscoelastic stresses that acts to deform the droplet along the direction of the motion.

	$Co_{Max} = 0.1$	$Co_{Max} = 0.04$	$Co_{Max} = 0.02$	$Co_{Max} = 0.01$
Newtonian				
Droplet aspect ratio D_a	0.936	0.973	0.986	0.992
Relative aspect ratio difference [%]	5.60	1.90	**0.60**	
Terminal velocity [mm/s]	2.223	2.284	2.288	2.296
Relative velocity difference [%]	3.18	0.52	**0.35**	
Viscoelastic ($De_T = 3.75$, $c = 0.5$)				
Droplet aspect ratio D_a	0.967	0.997	1.008*	1.014*
Relative aspect ratio difference [%]	7.70	4.00	**0.60**	
Terminal velocity [mm/s]	2.040	2.079	2.113	2.132
Relative velocity difference [%]	4.30	2.49	**0.89**	

5.5 Thermocapillary motion of a Newtonian droplet in a dilute viscoelastic fluid

For the time step and mesh independence study presented in the previous section we considered the thermocapillary migration of a two-dimensional Newtonian droplet surrounded by a viscoelastic Oldroyd-B fluid for one specific value of the thermal Deborah number, De_T, and the parameter c. We have observed that the presence of the viscoelastic stresses acts to slow down the droplet speed and also deform its shape (cf. Tab. 5.3).

In this section we present a systematic study aimed to reveal the effect of the various dimensionless parameters involved in the problem (i.e. De_T, c and L^2) for three-dimensional configuration when the surrounding viscoelastic phase is modelled using either the Oldroyd-B ($L^2 \to \infty$) or the FENE-CR models.

5.5.1 Oldroyd-B matrix fluid

5.5.1.1 Infinitely diluted solution

Firstly, we consider the case of the Oldroyd-B fluid ($L^2 \to \infty$) in the limiting condition in which the concentration of polymer molecules present in the solution is infinitely small, i.e., $c \to 0$ (in practice, we set $c = 0$ in our simulation). In such conditions, we can still compute the configuration tensor evolution by solving Eq. 5.3. However, in this case no viscoelastic stresses are produced and the flow field evolves in a Newtonian-like manner. The advantage of considering an "infinitely diluted" viscoelastic phase consists on the fact that we can analyse the polymer molecules deformation and orientation as they flow around the droplet, without having to take into account the presence of viscoelastic stresses that would modify the flow field and the droplet shape. In Sect 5.5.1.2 we shall repeat the analysis for finite values of the concentration parameter and same De_T, and we will see that the presence of visocoelastic stresses alters the deformation in a significant manner.

Fig. 5.4a shows the temporal evolution of the scaled droplet velocity for $c = 0$ and $De_T = 3.75$. After a relatively short transient, the droplet velocity
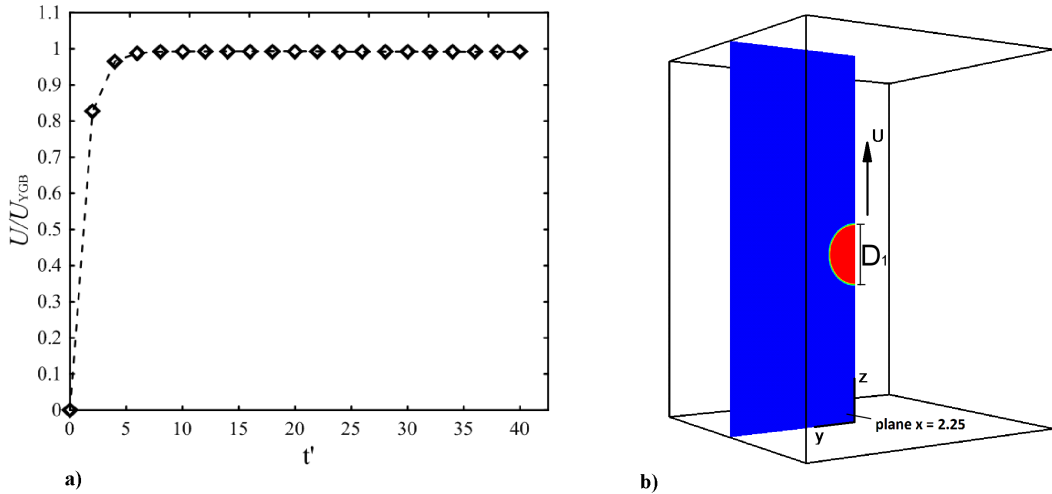
Figure 5.4: (a) Scaled droplet migration velocity for the case $De_T = 3.75$ and $c = 0$ as a function of the dimensionless time adopting the Oldroyd-B model. (b) Flow domain and contour of the level set function showing half of the droplet in the $x = 2.25$ plane.

approaches the theoretical (Newtonian) value described by Eq. (2.65). In this case the shape was found to be nearly spherical (the small departure from the exact shape has to be ascribed to the issues discussed in the previous section). To analyse the distribution of the configuration tensor around the droplet, we consider the $x = 2.25$ plane passing through the centre of the drop, as shown in Fig. 5.4b.

In Fig. 5.5 we show the three components of the conformation tensor on such plane. The xx-component was not considered in the present analysis since it was observed to remain nearly constant throughout the drop surface. Moreover, it is worth pointing out that the if we would repeat the analysis for any other plane passing through the axis of the drop, qualitatively similar results would be expected; the only (small) quantitative differences should be ascribed to the presence of the boundaries of the domain characterised by a square cross-sectional area. We stress the fact that the adoption of the geometry considered in the experiment of Hadland et al. (1999) is dictated by the fact that we have used it in all previous investigations, allowing us to make a direct comparison with the Newtonian results presented in the previous chapter. To provide a direct visual representation of the deformation and orientation of the polymer molecule as it flows around the droplet, in Fig. 5.5a we have also represented the configuration
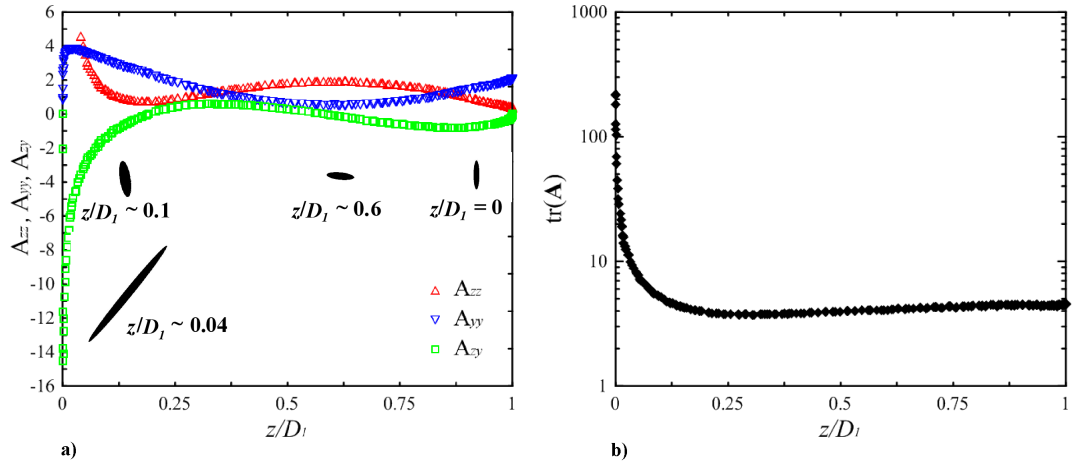
Figure 5.5: Normal and shear components of the configuration tensor, A_{zz}, A_{yy}, A_{zy} for the case $De_T = 3.75$ and $c = 0$ (a) and its trace in the region of the droplet surface (b) in the plane $x = 2.25$. All the results have been obtained adopting the Oldroyd-B model. In the inset of plot (a) the conformation tensor has been represented at four different locations by drawing ellipses that have major and minor axes parallel to the eigenvectors of $\mathbf{A}$ and lengths proportional to the corresponding eigenvalues. The abscissa z/D_1 is representative of the droplet extension along the direction of the motion, z, normalized by D_1. The origin of the axes is taken in a way that $z/D_1 = 0$ corresponds to the rear stagnation point, and $z/D_1 = 1$ to the front stagnation point. The component A_{zz} has been cut off in correspondence of the origin of the axes to make the representation more intelligible, since its maximum value is far larger than the maximum value of the other components.

tensor including ellipses having axes parallel to the principal axes defined by the eigenvectors of $\mathbf{A}$, while the extensions are proportional to the corresponding eigenvalues (see, e.g. Harlen, 2002).

By analysing the distribution of the components of $\mathbf{A}$ in an orthogonal Cartesian coordinates system positioned at the centre of the "cold side", and axes parallel to the sides of the domain, we notice that as the polymer chain approaches the front stagnation point, it initially experiences a bi-axial extension along the y-direction while being compressed along the other direction (cf. the ellipsoid shown at $z/D_1 = 0$). Subsequently, when the molecule moves further toward the rear of the drop, A_{yy} gradually decreases and reaches a minimum until the deformation becomes "compressive" $(A_{yy} < 1)$. On the other hand, A_{zz} follows the opposite trend: gradually increases, becomes extensional and reaches a peak (approximately at the same location where the other component assumes its minimum value. i.e., at $z/D_1 \approx 0.6$). As the molecule moves further downward, it keeps extending along the y-direction, with A_{yy} reaching a maximum and finally

vanishing as it approaches the rear stagnation point. On the other hand, A_{zz} initially decreases and reaches a minimum (here $A_{zz} \approx 1$, indicating a nearly relaxed state along the z-direction). Subsequently, the deformation suddenly increases and eventually assumes its largest value when z/D_1 is almost zero. The values assumed for small z/D_1 are not shown in the present plot for sake of representation (cf. the caption in Fig. 5.5). Regarding the shear component, A_{zy}, it is worth to notice its sudden decrease near the rear region, which is responsible for the change of the orientation of the molecule along the z-direction. If we in fact observe the ellipse depicted in correspondence of such area (at $z/D_1 \sim 0.04$), although the polymer filament is relatively close to the rear region, its orientation is still far from being aligned with the z-axis. The large shear component will guarantee that the molecule will be oriented with the direction of motion when it reaches the rear stagnation point.

Fig. 5.5b shows the evolution of the trace of the configuration tensor, $\mathrm{tr}(\mathbf{A})$ providing an indication of the degree of stretching of the molecule. We notice that the largest deformation occurs in a narrow region near the rear stagnation point, where the flow field is essentially a uniaxial straining flow. The fact that the largest molecule stretching (and so the largest viscoelastic stresses, if we would consider a finite dilution) occurs at the rear of the droplet, is qualitatively similar to what can be observed for the analogous case of the buoyant flow of a Newtonian drop in a viscoelastic liquid, where the drop assumes a tear-drop shape with a characteristic pointed tail (see e.g., the collection of experimental images available in Chhabra, 2006, or the numerical results of Pillapakkam et al. 2007). In such cases, in fact, the viscoelastic stresses tend to concentrate in a small area around the rear of the drop, with significant consequences on the morphological evolution of the droplet and distribution of the velocity field immediately downward the rear stagnation point.

5.5.1.2 Effect of the polymer concentration

In this section we focus on the effect of finite, non vanishingly small polymer concentrations on the motion of the drop. In contrast to the case studied in the

previous section, the molecule deformation associated with the flow field generates viscoelastic stresses, which are proportional to the amount of polymer molecules present in the viscoelastic phase.

Fig. 5.6a shows the comparison between the normal components of the configuration tensor for three different values of the polymer concentration parameter, $c = 0$, $c = 0.5$, $c = 0.89$, and for a fixed value of the Deborah number, $De_T = 3.75$. We notice that, irrespective of the value of c, the trends for A_{zz} remain qualitatively similar, with the main quantitative difference being a small increment of the peak observed in the region of the front half of the droplet ($0.5 < z/D_1 < 1$) as the concentration is increased. On the contrary, A_{yy} remains substantially unvaried in the front half, then, as the polymer molecule move towards the rear region, the trends appear remarkably different. In particular, we note that for $c = 0$, the maximum extent of the elongation along the y-direction appears just before the rear stagnation point. As the polymer concentration parameter is increased, the maximum is gradually shifted towards higher values of z/D_1.

Fig. 5.6b shows the trace of $\mathbf{A}$ for the same three values of c. As the molecules approach the rear of the drop, $\mathrm{tr}(\mathbf{A})$ decreases substantially as the concentration parameter is increased (at the stagnation point, the value of $\mathrm{tr}(\mathbf{A})$ for $c = 0.89$ is about four times smaller than that for the case $c = 0$), showing that the maximum elongation decreases when the concentration of polymer is increased. Such result does not have a straightforward and simple explanation due to a number of factors influencing the flow field downstream the droplet. First, we should consider that in all the simulations considered the total viscosity is always the same, thus the introduction of a certain amount of polymer results in a reduced solvent viscosity ($\eta_s = (1 - c)\,\eta_0$) which corresponds to a reduction of the Newtonian contribution to the total stress. Simultaneously, the presence of polymers generates viscoelastic stresses, which are mainly concentrated in a small area near the rear stagnation point where they are essentially purely extensional. These stresses "pull back" the droplet interface and, if they are large enough to overcome the capillary force, they can contribute to increase the local interface curvature. This circumstance in turn results in a localised increment of the pressure jump across the droplet

132

surface affecting the flow conditions immediately downstream the droplet.

In Sect. 5.4.1 we have anticipated that the presence of the viscoelastic stresses affects the droplet velocity. Fig. 5.7a shows the scaled droplet speed as a function of the dimensionless time for different values of the polymer concentration parameter, c (also in this analysis, we consider $De_T = 3.75$). Initially, the droplet speed increases rapidly, exhibiting an overshoot before reaching steady state conditions. We notice that the magnitude of the velocity peak depends on the parameter c, becoming larger when c is increased. Such behaviour can be explained considering that the viscoelastic stresses need a certain amount of time to develop, and thus initially the stresses at the interface are mainly of a "Newtonian nature". In other words, since the concentration parameter is given by the ratio of the polymer viscosity to the total viscosity, having assumed the latter property constant for each simulation, a larger value of c implies a smaller solvent viscosity, thus the Newtonian stresses prevailing at the first stage of the transient determine the observed behaviour. Fig. 5.7b shows the steady state velocity for the same cases
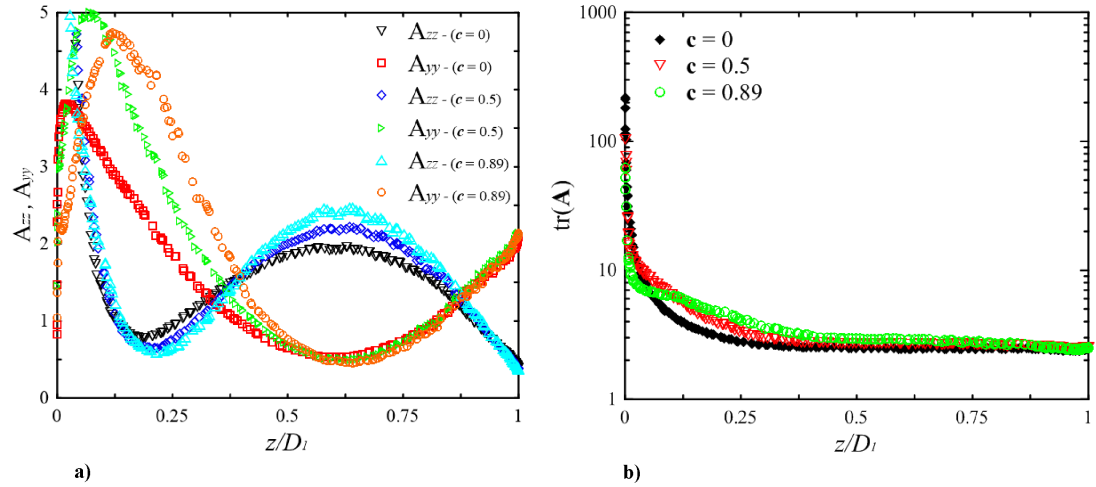
Figure 5.6: Normal components of the configuration tensor, A_{zz}, A_{yy} (a) and trace of the conformation tensor **A** in the region of the droplet surface in the plane $x = 2.25$ (b) for three different polymer molecule concentration parameters ($c = 0, 0.5, 0.89$) and for $De_T = 3.75$

under discussion. The simulations have shown that when the amount of polymer is increased, the droplet speed decreases monotonically and two different trends can be recognized. Initially, when c is small, the droplet velocity decrease is relatively steep, then, by further increasing the amount of polymer, the velocity

decreases less abruptly and follows a linear trend.
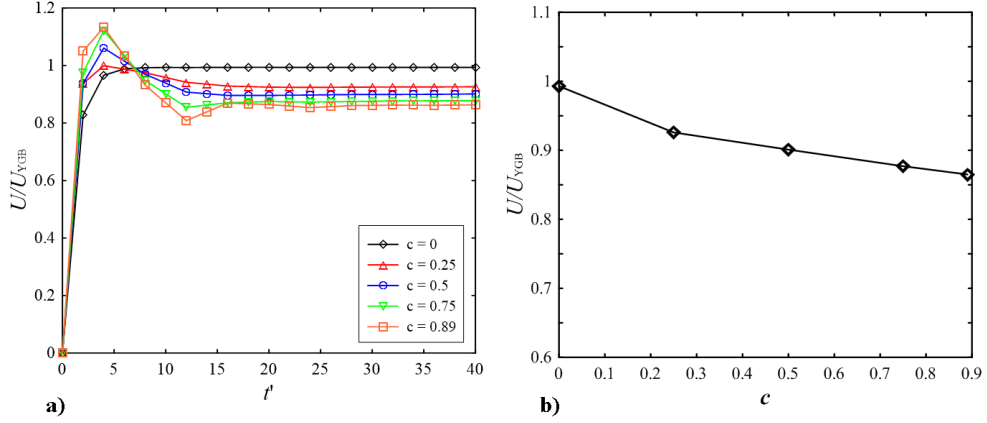
Figure 5.7: Time evolution of the scaled droplet speed for different polymer concentration parameters (a) and scaled steady state velocity as a function of the concentration parameter c (b). In both cases the Oldoyd-B model has been used considering $De_T = 3.75$.

As a concluding remark, it is worth noticing that despite the fact that in VOF based methods the interface is "sharp" in a sense that the volume fraction changes abruptly between the phases, the area occupied by the interface itself lies in a finite region where $0 < \alpha_k < 1$. The actual interface however, should be ideally represented by the contour $\alpha_k = 0.5$, thus the analyses presented so far have been conducted adopting this value. It is worth to note that similar analysis conducted adopting any other value of the volume fraction representative of the interface, would provide qualitatively similar, but quantitatively different results. In light of this, it is easy to realise that if we would compute the viscoelastic stresses distribution around the drop adopting the field **A** evaluated for a certain value of $0 < \alpha_k < 1$, the stress field obtained would be different from that over the actual drop boundary since the polymer viscosity and the relaxation time are interpolated through the interface by means of Eq. (2.75).

5.5.1.3 Effect of the Deborah number

Fig. 5.8a shows the steady state droplet velocity as a function of De_T for two different values of the polymer concentration parameter, $c = 0.5$ and $c = 0.89$. The plot indicates that in both cases the droplet velocity decreases with De_T and the two trends can be well approximated by a quadratic polynomial, $U/U_{YGB} \approx 1 - k_1 \times De_T - k_2 \times De_T^2$, with k_1 and k_2 being two constants that

134

depend on the value of c. In Fig. 5.8b we show some of the steady state droplet shapes obtained for different values of De_T and c. As anticipated previously, in the presence of a viscoelastic surrounding phase, the droplet tends to be stretched along the direction of the motion. For $De_T = 1.5$ the droplet is nearly spherical, while for the largest value of De_T, on the contrary, a loss of fore-and-aft symmetry is evident, with the droplet exhibiting a "pointed end" (similarly to the gravity-driven motion discussed in the introduction of the chapter) generated by the large viscoelastic stresses localized at the rear stagnation point. The effect of the concentration on the shapes is only minimal under those conditions (even though for larger concentrations, slightly larger deformations are observed). The effect of the thermal Deborah number, on the other hand, is more pronounced.

It is finally worth showing the comparison between the Newtonian flow field and some representative viscoelastic cases. Fig 5.9 shows the streamlines for the Newtonian case (a) and for different values of De_T (b, c and d) in the diagonal plane passing though to opposite corners of the domain. In the absence of elasticity, a large portion of the flow field is occupied by two main recirculations passing through the droplet, while a second pair of minor rolls is established next to the "cold" wall. When De_T is increased, the latter two recirculations tend to shrink and two new rolls become visible in the opposite wall. Finally, for the largest

a)

b)
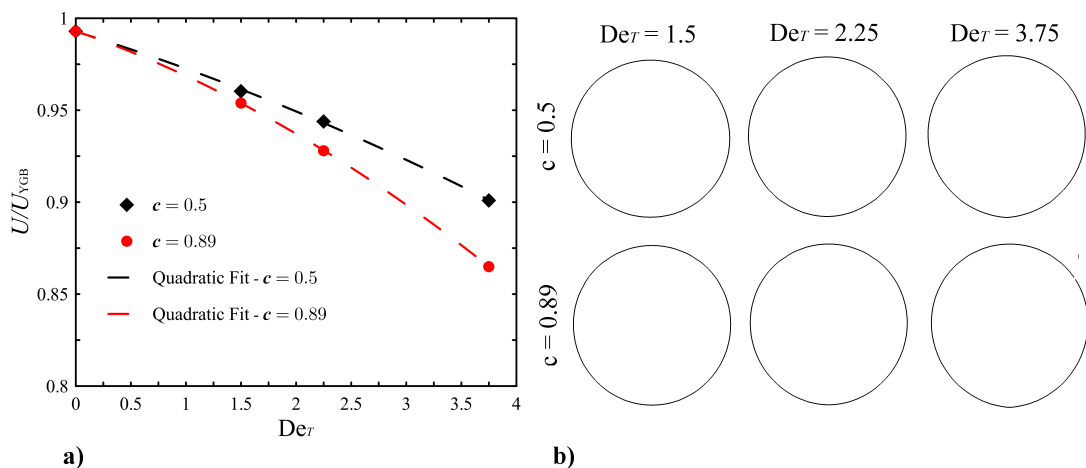
Figure 5.8: (a) Scaled migration velocity for a droplet surrounded by the Oldroyd-B fluid as a function of the Deborah number. (b) Droplet shapes for different values of the thermal Deborah for $c = 0.5$ (top), and for $c = 0.89$ (bottom) (b). Note the presence of a "pointed end" for the largest values of the Deborah number.
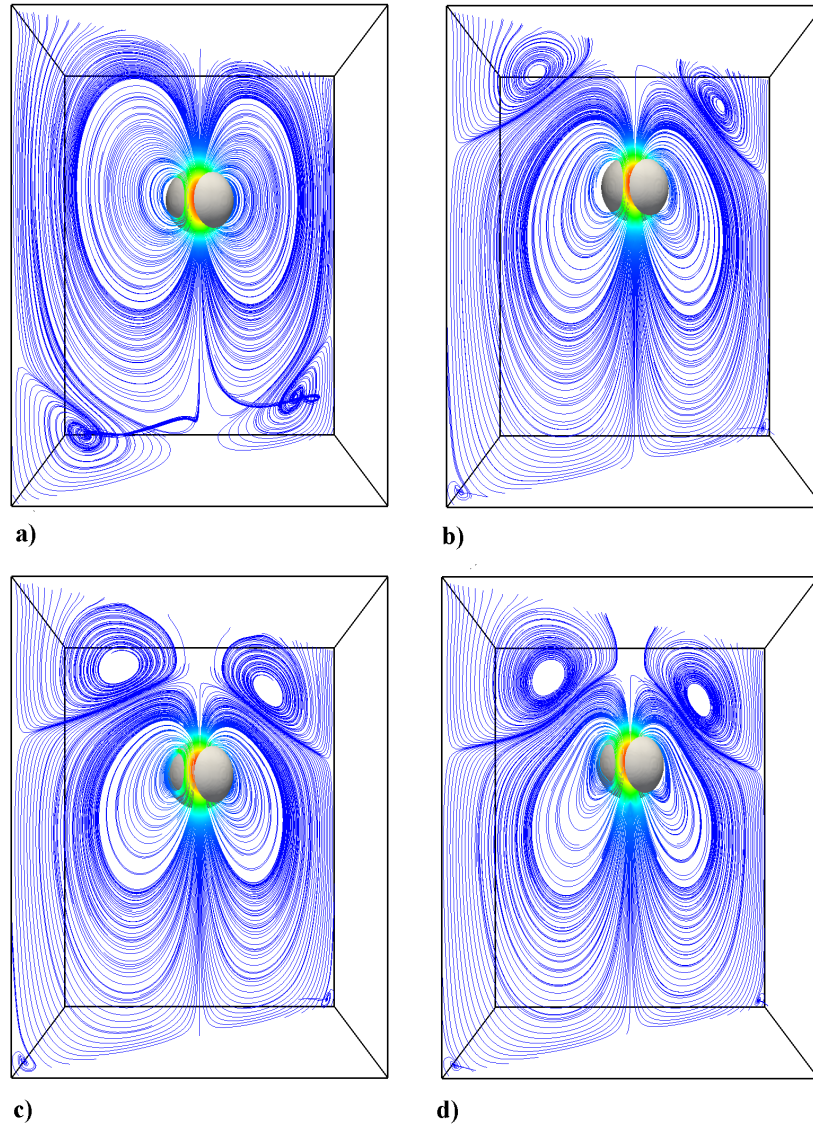
Figure 5.9: Streamlines in the plane passing through two opposite corners of the domain for three different conditions: a) Newtonian, b) $De_T = 1.5$, $c = 0.5$, c) $De_T = 2.25$, $c = 0.5$ and d) $De_T = 3.75$, $c = 0.5$. The droplets are moving upward.

De_T considered, the region covered by the new vortices embrace the whole area adjacent to the "hot" wall.

5.5.2 FENE-CR matrix fluid

As discussed in Sect. 2.3.1 the Oldroyd-B model imposes severe restriction on the maximum value of the Deborah number allowable because of the singular nature of its solution when the flow field is extensional. For such reason, the simulation shown in the previous section were limited to a maximum value of

the thermal Deborah of 3.75. To be able to study the impact of larger Deborah numbers, we ran a series of simulations adopting the FENE-CR model. This constitutive law bounds the maximum elongation of the polymer chain through the extensibility parameter, L^2, allowing the investigation of flows at significantly higher Deborah numbers.

Fig. 5.10a shows the scaled migration velocity as a function of De_T for $L^2 = 100$ and two values of the concentration parameter: $c = 0.5$ and $c = 0.89$. Similarly to what has been observed for the case of the Oldroyd-B model, the steady-state droplet velocity decreases monotonically with increasing De_T, and to larger values of the polymer concentrations parameter correspond smaller terminal velocities. For the smallest Deborah considered ($De_T = 3.75$), no substantial differences have been observed between the results shown here for the FENE-CR model with $L^2 = 100$ and those obtained for $L^2 \to \infty$ (Fig. 5.8) obtained with the Oldroyd-B model. In fact, the relative velocity difference between these two case is about 1%. Such result suggests that, for relatively small Deborah number, the maximum extensibility of the molecule does not affect the migration velocity significantly. The main qualitative difference in the trends shown in Fig. 5.8 for low De_T and in Fig. 5.9 for higher De_T is the different concavity of the curve. Contrarily to the low$-De_T$ regime, in the present situation the droplet speed initially decreases with De_T in a relatively steep manner, with the decrease becoming less pronounced and tending to a plateau region as the Deborah number is further increased.

In order to investigate the influence of the extensibility parameter, we ran a series of simulations for some representative values of L^2, considering $De_T = 7.5$ and $c = 0.5$. Fig. 5.10b shows how the terminal migration velocity decreases monotonically as the maximum allowable molecule extension is increased. It is interesting to notice that the for $L^2 = 400$, the velocity reduction relative to the YGB limit is about 20%, while for $L^2 = 10$, the relative velocity decrease is about 10%, highlighting the large impact of the extensibility parameter on the migration velocity.

Fig. 5.11 shows the contours of the trace of the conformation tensor for differ-

ent values of the extensibility parameter, showing, as expected, that the normal stresses increase as the extensibility parameter L^2 is increased. Additionally, appears evident how the configuration tensor distribution around the droplet surface is largely affected by the value of L^2. In particular, for $L^2 = 10$ (Fig. 5.11a), we notice that the region of the interface characterised by larger values of $\text{tr}\,(\mathbf{A})$ occupy a wide portion of the rear of the droplet. As L^2 is increased, the maximum values of $\text{tr}\,(\mathbf{A})$ tend to be localised in a narrower region. Arguably, this have direct consequences on the deformation of the droplet surface, and we can infer that the mechanism of formation of the cusp is strongly affected by the maximum molecule elongation allowable.

a)   b)
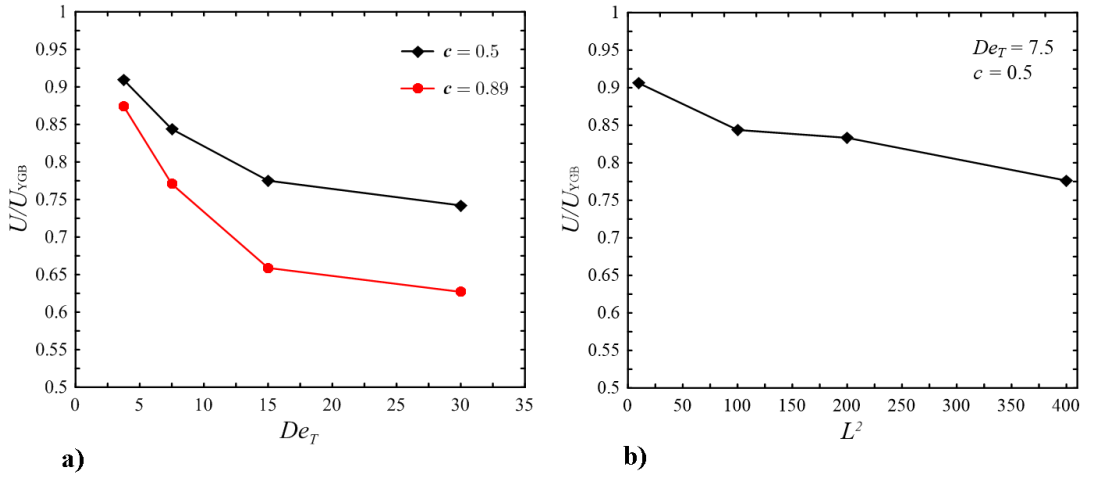
Figure 5.10: Scaled steady state migration velocity obtained with the FENE-CR model as a function of De_T for two values of the polymer concentration parameter, c, and $L^2 = 100$ (a), and as a function of the extensibility parameter, L^2, for $De_T = 7.5$ and $c = 0.5$ (b).

Fig. 5.12 shows the droplet shape evolution for the cases $c = 0.5$ (a) and $c = 0.89$ (b) for $De_T = 30$ and $L^2 = 100$, showing the different transients experienced by the drop, both in terms of migration velocity and morphological evolution. Initially (instant t_1), the drop is not yet affected by a large deformation, and its shape is a prolate ellipsoid. Afterwards (instant t_2), the viscoelastic stresses, which are mainly developing around the second half of the droplet (the conformation tensor distribution was found to be qualitatively similar to that observed for the case of the Oldroyd-B model, thus, for the sake of brevity we do not repeat the analysis shown before) are responsible for the loss of fore-and-aft symmetry, but the pointed end is not yet visible. It is worth to notice that at
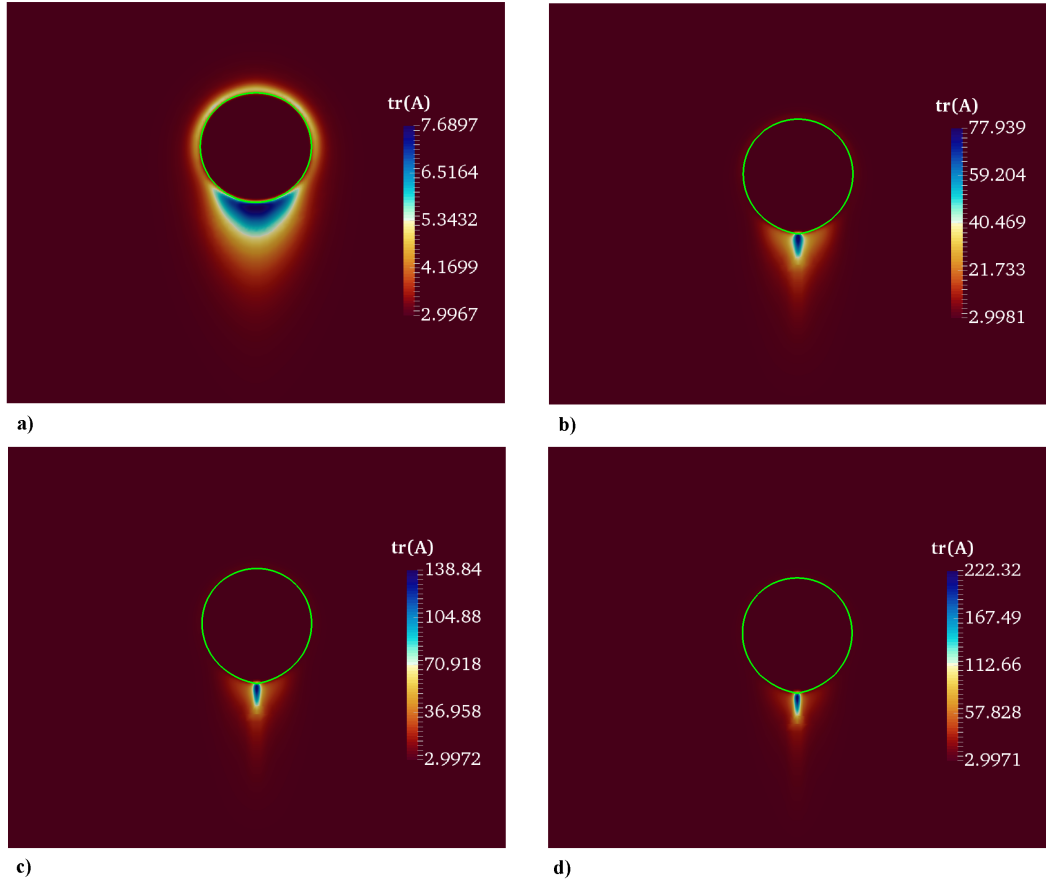
Figure 5.11: Contours of the trace of the conformation tensor, $\mathbf{A}$, at steady state for $De_T = 7.5$ and $c = 0.5$ for: (a) $L^2 = 10$, (b) $L^2 = 100$, (c) $L^2 = 200$ and (d) $L^2 = 400$

this stage the rear of the drop is more flattened for the case $c = 0.89$ than for the case for $c = 0.5$, suggesting that during the transient the viscoelastic stresses tend to be distributed differently depending on the value of the parameter c. At the instant t_3, for the case $c = 0.5$ we notice the presence of a pointed end, which is not yet visible for the higher concentration parameter $c = 0.89$. Finally, the last stage (instant t_4) shows the steady state configuration assumed by the droplets, in which the presence of the pointed end can also be noticed for the larger value of c. Despite the terminal velocities being larger for smaller values of c, it is interesting to notice that between instants t_1 and t_2 the droplet has travelled for a longer distance in the case $c = 0.89$ rather than in the case $c = 0.5$. Such difference has to be ascribed to the the fact that the viscoelastic stresses require a certain amount of time to develop. Initially, in fact, the contribution to the hydrodynamic resistance is mainly due to the presence of viscous stresses which are proportional

139

to the solvent viscosity, $\eta_{s,m}$, therefore, since for the case $c = 0.89$, $\eta_{s,m}$ (i.e., the magnitude of the viscous stress tensor) is lower than that for the case $c = 0.5$, the velocity is initially larger.
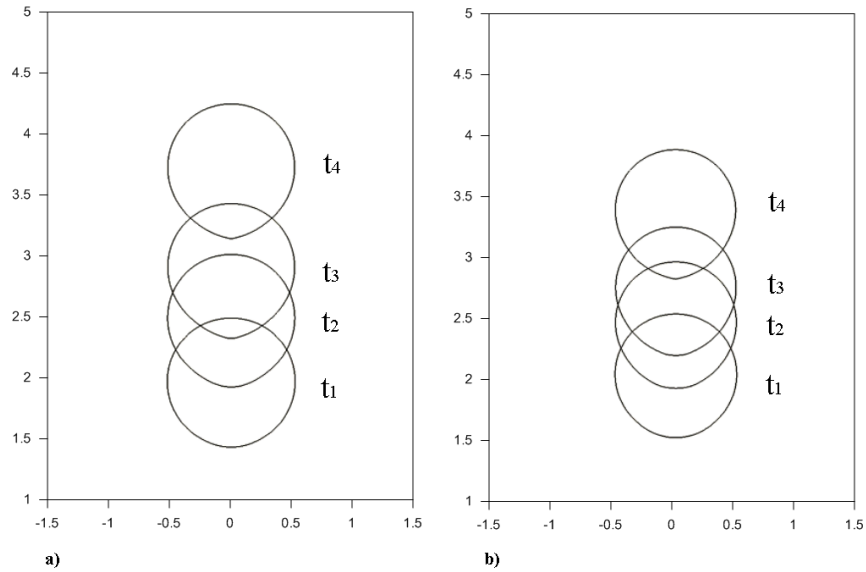
Figure 5.12: Droplet shape temporal evolution for $De_T = 30$ and $L^2 = 100$, for $c = 0.5$ (a), and for $c = 0.89$ (b). The time frames are the same for the two pictures, evidencing the different droplet transient velocity evolution.

5.6   Conclusions

In this chapter we focused on the numerical investigation of the thermocapillary motion of a Newtonian deformable droplet surrounded by a viscoelastic immiscible liquid. The impact of viscoelasticity on the droplet velocity and shape has been analysed in different viscoelastic flow conditions adopting two separate viscoelastic constitutive laws. The Oldroyd-B model has been used for relatively small values of the thermal Deborah number, while for the flow regimes where the latter model was no longer successfully applicable, the viscoelastic behaviour was modelled with the FENE-CR model.

In the first case, two distinct flow conditions have been considered, namely the case of an "infinitely diluted" solution, which allows us to analyse the deformation history of the polymer molecule flowing in a Newtonian flow field i.e., in absence of viscoelastic stresses, and the case of a finite, non-vanishingly small dilution, where the coupling between the viscoelastic stresses and the flow field was expected to

modify the process and the extent of the deformation as they flow around the drop. The numerical experiments have shown that regardless of the polymer concentration, quantified by the parameter c, the viscoelastic stresses always tend to be concentrated in proximity of the rear stagnation point, where the extensional nature of the flow determines the larger polymer molecule deformation. On the contrary, the value of the parameter c was found to be influential on the maximum dumbbell elongation, which was found to decrease for increasing values of the concentration.

For finite values of the parameter c, it has been observed a remarkable influence of the viscoelastic stresses on both the migration velocity and droplet shape. In particular, the numerical results have shown that the droplet speed decreases in a quadratic manner by increasing the relaxation time of the viscoelastic phase, and to larger values of the polymer concentration parameter correspond larger decrement of the migration velocity. In terms of shape, as the Deborah number increases, the droplet initially becomes a prolate ellipsoid, then, for subsequent increments of the relaxation time, a certain degree of loss of fore-and-aft symmetry has been observed. Specifically, for the largest value of the thermal Deborah number considered with the Oldroyd-B model, the concentration of viscoelastic stresses near the rear stagnation point were found to be responsible of the development of a "pointed tail" (it is worth noticing however, that in a strict sense the shape depends on the product $CaDe_T$ rather than De_T alone, thus the actual local variation of the curvature is expected to be sensitive to variation of both these two parameters). A comparison between different values of the parameter c for constant values of De_T, has shown that the droplet velocity decreases monotonically also for increments of this latter parameter. On the other hand, only little differences on the steady state droplet shape can be observed when the parameter c is changed.

The FENE-CR model has been adopted for De_T up to the maximum value of 30. No remarkable phenomenological differences in comparison to the previous cases have been encountered. In particular, the viscoelastic stresses have shown the same tendency to be localized next to the rear stagnation point, bringing to

141

similar consequences on the droplet shape. The velocity of the droplet has been found to be a monotonic decreasing function of De_T also in this case, however the trend observed is qualitatively different from the one seen for the case of the Oldroiyd-B model. Seems reasonable to hypothesise however, that the different behaviour should be ascribed to the fact that the two flow regimes are substantially different, rather than attribute it to the adoption of different models.

Finally, the effect of the extensibility parameter on the terminal velocity has been investigated for some selected cases. The results have shown that the steady state droplet speed decreases monotonically for increasing values of L^2.

Chapter 6

Thermocapillary motion of a Newtonian drop in a weakly viscoelastic Oldroyd-B fluid – Analytical solution

6.1 Introduction

In Chapter 5, the thermocapillary motion of a Newtonian droplet surrounded by a viscoelastic fluid was investigated numerically for a fairly large range of Deborah numbers adopting two different viscoelastic models. It was observed that for all the conditions considered, the droplet speed always decreases monotonically as De_T is increased. Additionally, the velocity decrease is larger for higher polymer concentrations c. Although the usefulness of a numerical approach is undeniable, since it allows one to investigate arbitrary values of Deborah number (within the limitations discussed in Sect. 2.3.1), an exhaustive parametric study that would account for the variation of each material parameter would be excessively time demanding. Additionally, it has been also pointed out that with the present methodology, it is not possible to simulate flows for arbitrary small Capillary number with a desired accuracy due to the increasing level of spurious velocities in surface tension-dominated flows (see. e.g., Galusinski and Vigneaux, 2008). For these reasons, together with the lack of experimental results, in the present chapter we seek an analytical solution to the problem for a Newtonian droplet surrounded by an unbounded viscoelastic fluid in the form of a perturbation expansion in De_T (i.e., assuming $De_T < 1$) in the limit of $(Re, Ma) \to 0$. Interface deformations are also allowed in some cases by considering finite, non

vanishingly small values of the Capillary number.

6.2   Governing equations

To describe the problem under discussion, we shall make use of the results obtained is Sect. 2.4. In particular, we consider the governing equations written in dimensionless form (Eqs. 2.55-2.62) bearing in mind that now the droplet phase (we recall that the following discussion is general, and pertains its validity also for the case of a gas bubble) is Newtonian, thus Eq. 2.62 simply yields $\tilde{\boldsymbol{\tau}} = \alpha \widetilde{\mathbf{D}}$. Using this result, the complete dimensionless system of equation reads

$$\nabla \cdot \mathbf{u} = 0 \tag{6.1}$$

$$Re\frac{D\mathbf{u}}{Dt} = -\nabla p + \nabla \cdot \boldsymbol{\tau} \tag{6.2}$$

$$Ma\frac{DT}{Dt} = \nabla^2 T \tag{6.3}$$

$$\boldsymbol{\tau} + De_T \hat{d}\boldsymbol{\tau} = \mathbf{D} + \beta De_T \hat{d}\mathbf{D} \tag{6.4}$$

$$\nabla \cdot \tilde{\mathbf{u}} = 0 \tag{6.5}$$

$$\delta Re\frac{D\tilde{\mathbf{u}}}{Dt} = -\nabla \tilde{p} + \alpha \nabla \cdot \widetilde{\mathbf{D}} \tag{6.6}$$

$$Ma\frac{D\widetilde{T}}{Dt} = \alpha_{th}\nabla^2 \widetilde{T} \tag{6.7}$$

In this work, we assume a steady-state and ignore convective transport of momentum and energy. In such case, the above system of equations becomes

$$\nabla \cdot \mathbf{u} = 0 \tag{6.8}$$

$$\nabla p = \nabla \cdot \boldsymbol{\tau} \tag{6.9}$$

$$\nabla^2 T = 0 \tag{6.10}$$

for the continuous phase, and

$$\nabla \cdot \tilde{\mathbf{u}} = 0 \tag{6.11}$$

$$\nabla \tilde{p} = \alpha \nabla \cdot \widetilde{\mathbf{D}} \tag{6.12}$$

$$\nabla^2 \widetilde{T} = 0 \tag{6.13}$$

for the droplet phase. The viscoelastic model has been momentarily left out of the discussion since it will be treated in a special manner, as it will appear clear in Sect. 6.2.1. Solution of Eqs. (6.8-6.13) requires the adoption of suitable boundary conditions. Since the continuous phase is unbounded, in a spherical coordinate system moving with the translating drop (cf. Fig. 2.1), the boundary conditions for the velocity and temperature fields at infinity read, respectively

$$u|_{r=\infty} \to U \tag{6.14}$$

$$T|_{r=\infty} \to r \cos \theta \tag{6.15}$$

while at the drop surface we have (cf. the conditions introduced in Section 2.4)

$$u_r = \tilde{u}_r = 0 \tag{6.16}$$

$$u_\theta = \tilde{u}_\theta \tag{6.17}$$

$$T = \widetilde{T} \tag{6.18}$$

$$\frac{\partial T}{\partial r} = \gamma \frac{\partial \widetilde{T}}{\partial r} \tag{6.19}$$

$$\tilde{p} - p + \mathbf{n} \cdot (\boldsymbol{\tau} - \alpha \, \tilde{\boldsymbol{\tau}}) \cdot \mathbf{n} = \frac{1}{Ca} \left(1 - CaT \right) \nabla \cdot \mathbf{n} \tag{6.20}$$

$$\mathbf{n} \cdot (\boldsymbol{\tau} - \alpha \, \tilde{\boldsymbol{\tau}}) \cdot \mathbf{t} = \frac{\partial T}{\partial \theta} \tag{6.21}$$

where $\gamma = \tilde{\kappa}/\kappa$. Finally, to characterise the problem completely, we need to include two additional constrains at the centre of the drop for the velocity and

temperature field, namely

$$\tilde{u}|_{r=0} < \infty \tag{6.22}$$

$$\widetilde{T}\Big|_{r=0} < \infty \tag{6.23}$$

In writing the normal stress condition (6.20), we have taken into account the fact that the interfacial tension depends on the temperature following the law given by Eq. (3.5) (see e.g., Subramanian and Balasubramanian, 2001), providing two separate contributions, as already observed in Sect. 3.2.

The solution of the problem is made difficult by the fact that the position of the interface is generally not known, and it should be found as a part of the solution. Nevertheless, for the class of problems considered here, the usual strategy is to seek a solution by assuming that the shape of the interface is known a priori by replacing the condition (6.20) with another suitable constrain, as explained further below. Once the flow field is known, we verify a posteriori whether the choice made for the shape is consistent by assessing whether the normal stress balance condition, Eq. (6.20) is satisfied. If a mismatch is found, a correction to the droplet shape is found from the linearised version of Eq. (6.20), as explained in the following.

An axisymmetric droplet shape can be conveniently represented in a dimensionless manner as (Taylor and Acrivos, 1965)

$$r = 1 + \zeta(\theta) \tag{6.24}$$

where $\zeta(\theta)$ is an unknown function to be determined as a part of the solution ($\zeta(\theta) = 0$ being the case of a the spherical particle). In such a case then, the normal stress balance (6.20) can be linearised in the following manner (Landau and Lifshitz, 1959)

$$\tilde{p} - p + \mathbf{n} \cdot (\boldsymbol{\tau} - \alpha\,\tilde{\boldsymbol{\tau}}) \cdot \mathbf{n} =$$
$$\frac{1}{Ca}\left(1 - CaT(s)|_{r=1}\right)\left\{2 - 2\zeta - \frac{d}{ds}\left[\left(1 - s^2\right)\frac{d\zeta}{ds}\right]\right\} \tag{6.25}$$

where $s = \cos\theta$. Once the pressure and stresses are known, Eq.(6.25) becomes a simple ODE for the shape function ζ. Unfortunately, its analytical solution is made problematic by the presence of the temperature-dependent contribution, which in turn depends on the variable s. In Sect. 6.2.4 we shall illustrate under which particular conditions this term can be safely neglected.

6.2.1 Asymptotic expansion

In the present mathematical treatment we are concerned with a viscoelastic fluid that is only slightly non-Newtonian. In this case, we seek the solution by adopting a perturbation scheme, expanding all the relevant variables around the small parameter $De_T < 1$. In the present work, we expanded up to the second order in De_T, nevertheless one can in principle apply the methodology up to any order. Also, the radius of convergence of perturbation expansions, like the one we use here, is typically low, thus higher order terms are rather useless. For these reasons, the usual practice is to truncate the expansion at the first few contributions.

To second order, the expansion for the velocity, pressure and stress fields are given by

$$\mathbf{u} = \mathbf{u}_0 + De_T \mathbf{u}_1 + De_T^2 \mathbf{u}_2 + O\left(De_T^3\right) \tag{6.26}$$

$$p = p_0 + De_T p_1 + De_T^2 p_2 + O\left(De_T^3\right) \tag{6.27}$$

$$\boldsymbol{\tau} = \boldsymbol{\tau}_0 + De_T \boldsymbol{\tau}_1 + De_T^2 \boldsymbol{\tau}_2 + O\left(De_T^3\right) \tag{6.28}$$

Similarly, observing that the operator $\hat{d}\left(\cdot\right)$ also depends on the velocity, we define

$$\hat{d}_j\left(\cdot\right) = \mathbf{u}_j \cdot \nabla\left(\cdot\right) - \left\{\nabla \mathbf{u}_j^T \cdot \left(\cdot\right) + \left(\cdot\right) \cdot \nabla \mathbf{u}_j\right\} \tag{6.29}$$

where $j = 0,1,2$; here, we neglected the time derivative since we are considering steady-state conditions, as noted before. Substituting the above expressions for the velocity and the stress tensor into the Oldroyd-B viscoelastic model (Eq. 6.4) and using equation (6.29), we obtain the following expressions for the stress

147

tensor at each order

$$\boldsymbol{\tau}_0 = \mathbf{D}_0 \tag{6.30}$$

$$\boldsymbol{\tau}_1 = \mathbf{D}_1 - (1 - \beta)\,\hat{d}_0\mathbf{D}_0 \tag{6.31}$$

$$\boldsymbol{\tau}_2 = \mathbf{D}_2 - (1 - \beta)\left[\hat{d}_0\mathbf{D}_1 + \hat{d}_1\mathbf{D}_0 - \hat{d}_0^2\mathbf{D}_0\right] \tag{6.32}$$

Finally, for the migration velocity we have

$$U = U_0 + De_T U_1 + De_T^2 U_2 + O\left(De_T^3\right) \tag{6.33}$$

Recalling that the non-Newtonian flow perturbation does not affect the temperature field, one realises that the variable T should not be perturbed (in other terms, the solution of the energy equation is required only at order zero in De_T). Since the viscoelastic exterior flow field will affect the interior through the boundaries, similar expansions (cf. Eqs. 6.26-6.27) apply also for the droplet phase. Using these results, the system of governing equation at order zero for the continuous phase becomes

$$\nabla \cdot \mathbf{u}_0 = 0 \tag{6.34}$$

$$\nabla p_0 = \nabla^2\mathbf{u}_0 \tag{6.35}$$

$$\nabla^2 T = 0 \tag{6.36}$$

whilst, at first order

$$\nabla \cdot \mathbf{u}_1 = 0 \tag{6.37}$$

$$\nabla p_1 = \nabla^2\mathbf{u}_1 + \boldsymbol{f}_1\left(\mathbf{u}_0\right) \tag{6.38}$$

and finally, for the second order

$$\nabla \cdot \mathbf{u}_2 = 0 \tag{6.39}$$

$$\nabla p_2 = \nabla^2\mathbf{u}_2 + \boldsymbol{f}_2\left(\mathbf{u}_0, \mathbf{u}_1\right) \tag{6.40}$$

where the functions $\boldsymbol{f}_1\left(\mathbf{u}_0\right)$, $\boldsymbol{f}_2\left(\mathbf{u}_0, \mathbf{u}_1\right)$ are given by

$$\boldsymbol{f}_1\left(\mathbf{u}_0\right) = -\left(1 - \beta\right) \nabla \cdot \left(\hat{d}_0 \mathbf{D}_0\right) \tag{6.41}$$

$$\boldsymbol{f}_2\left(\mathbf{u}_0, \mathbf{u}_1\right) = -\left(1 - \beta\right) \left[\nabla \cdot \left(\hat{d}_0 \mathbf{D}_1 + \hat{d}_1 \mathbf{D}_0\right) - \hat{d}_0^2 \mathbf{D}_0\right] \tag{6.42}$$

Finally for the droplet phase, we have

$$\nabla \cdot \tilde{\mathbf{u}}_i = 0 \tag{6.43}$$

$$\nabla \tilde{p}_i = \nabla^2 \tilde{\mathbf{u}}_i \tag{6.44}$$

$$\nabla \widetilde{T}_i = 0 \tag{6.45}$$

being $T_1 = T_2 = 0$ for the reasons explained above.

6.2.2 Streamfunction formulation

Since the flow is incompressible and axisymmetric, it is convenient to re-formulate the problem adopting the Stokes streamfunction. The continuity equation in spherical coordinates reads

$$\nabla \cdot \mathbf{u} = \frac{1}{r^2} \frac{\partial}{\partial r}\left(r^2 u_r\right) + \frac{1}{r \sin \theta} \frac{\partial}{\partial \theta}\left(u_\theta \sin \theta\right) \tag{6.46}$$

From a direct inspection of Eq. (6.46), it is easy to see that the velocity fields defined as

$$u_r = -\frac{1}{r^2 \sin \theta} \frac{\partial \psi}{\partial \theta}, \quad u_\theta = \frac{1}{r \sin \theta} \frac{\partial \psi}{\partial r} \tag{6.47}$$

where $\psi\left(r, \theta\right)$ is an arbitrary function, automatically satisfy the incompressibility condition. In the present context (three-dimensional and axisymmetric flow) $\psi\left(r, \theta\right)$ takes the name of Stokes streamfunction, and has the property to be constant along each streamline (see, e.g., Leal 2007). Using the above results, the

system of equation at order zero in De_T becomes (see, Bird et al. 1987)

$$E^4\psi_0 = 0, \quad \nabla^2 T = 0 \tag{6.48}$$

$$E^4\widetilde{\psi}_0 = 0, \quad \nabla^2\widetilde{T} = 0 \tag{6.49}$$

having introduced the bi-harmonic operator

$$E^2 = \left(\frac{\partial^2}{\partial r^2} + \frac{\sin\theta}{r^2}\frac{\partial}{\partial\theta}\left(\frac{1}{\sin\theta}\frac{\partial}{\partial\theta}\right)\right) \tag{6.50}$$

such that $E^2 E^2 \psi \equiv E^4 \psi$. Analogously, for the other two expansions it is possible to eliminate pressure in a similar fashion, providing

$$E^4\psi_1 - [\nabla \times \boldsymbol{f}_1(\mathbf{u}_0)]\, r\sin\theta \cdot \hat{\boldsymbol{e}}_\phi = 0 \tag{6.51}$$

$$E^4\widetilde{\psi}_1 = 0 \tag{6.52}$$

at first order, whilst at second order

$$E^4\psi_2 - [\nabla \times \boldsymbol{f}_2(\mathbf{u}_0, \mathbf{u}_1)]\, r\sin\theta \cdot \hat{\boldsymbol{e}}_\phi = 0 \tag{6.53}$$

$$E^4\widetilde{\psi}_2 = 0 \tag{6.54}$$

where $\hat{\boldsymbol{e}}_\phi$ is the unit vector in the azimuthal direction.

6.2.3 Solution techniques for the streamfunction and temperature differential equations

The solution of the equation for the streamfunction, written in a general form as $E^4\psi(r,s) = g(r,s)$ is given by the sum of the solution for the homogeneous problem (i.e., $E^4\psi(r,s) = 0$) (Happel and Brenner, 1983) and a particular solution, $\psi_p(r,s)$, $viz.$

$$\psi(r,s) = \sum_{n=2}^{\infty} \left[\left(A_n r^n + B_n r^{-n+1} + C_n r^{n+2} + D_n r^{-n+3}\right)G_n^{-1/2}(s)\right] + \psi_p \tag{6.55}$$

where A_n, B_n, C_n, D_n are the constants to be determined according to the boundary conditions adopted for the specific problem, and $G_n^{-1/2}(s)$ are Gegenbauer functions of the first kind and degree $-1/2$. The general form of the Gegenbauer polynomials is provided by the formula reported below (see, eg., Djordjević and Milovanović, 2014)

$$G_n^\lambda(s) = \sum_{\ell=0}^{n/2} (-1)^\ell \frac{\Gamma(n-\ell+\lambda)}{\Gamma(\lambda)\,\ell!\,(n-2\ell)!} (2s)^{n-2\ell} \tag{6.56}$$

with the starting values $G_0^\lambda(s) = 1$ and $G_1^\lambda(s) = 2\lambda s$ and Γ being the gamma function.

The solution of the Laplace equation in spherical coordinates is also straightforward (see, e.g., Subramanian and Balasubramanian, 2001)

$$T(r,s) = \sum_{k=0}^{\infty} \left(A_k r^k + B_k r^{-k-1}\right) \left[P_k(s) + C_k H_k(s)\right] \tag{6.57}$$

where A_k, B_k, C_k, are constants and $P_k(s)$, $H_k(s)$ are Legendre functions of the first and second kind, respectively. Similarly to Gegenbauer polynomials, the functions $P_k(s)$ can be defined as

$$P_k(s) = \sum_{\ell=0}^{k/2} (-1)^\ell \frac{(2k-2\ell-1)!!}{2^{k-\ell}\ell!\,(k-2\ell)!} (2s)^{k-2\ell} \tag{6.58}$$

Gegenbauer and Legendre function of first kind are related, since it can be verified from Eqs. (6.56 and 6.58) that the following relationship holds

$$P_n(s) = G_n^{1/2}(s) \tag{6.59}$$

Legendre functions of second kind, $H_k(s)$, are singular for $s = \pm 1$, that is, at the two stagnation points at the droplet surface in the present case (so that, for $\theta = 0, \pi$). For this reason, the constant C_k will be immediately set to zero when solving the temperature equations appearing in Eqs. (6.48-6.49).

6.3   Newtonian solution

Before addressing the viscoelastic problem, we need to obtain the Newtonian flow field required to calculate the stress tensor at first order (Eq. 6.31). The solution of the present problem is well known (Young et al. 1959), and here we limit ourselves to describing the general procedure and report the main findings.

The problem under examination is described by Eqs. (6.48-6.49) with the boundary conditions (6.14-6.23) specialised for the Newtonian field. The first step is to calculate the temperature which in turn will serve to define the thermo-capillary stresses appearing in the tangential stress condition (6.21). By direct application of Eq. (6.55) with the conditions (6.15, 6.18, 6.19 and 6.23) it can be shown that the temperature field outside and inside the drop are given by (see, Subramanian and Balasubramanian, 2001)

$$T\left(r,s\right) = \left(r + \frac{1-\gamma}{2+\gamma}\frac{1}{r^2}\right)P_1\left(s\right) \tag{6.60}$$

$$\widetilde{T}\left(r,s\right) = \frac{3r}{2+\gamma}P_1\left(s\right) \tag{6.61}$$

(note that $P_1\left(s\right) = s = \cos\theta$), therefore at the droplet surface we have $T\left(1,s\right) = \widetilde{T}\left(1,s\right) = \frac{3}{2+\gamma}\cos\theta$, thus Eq. (6.21) becomes

$$\mathbf{n}\cdot\left(\mathbf{D}_0 - \alpha\,\widetilde{\mathbf{D}}_0\right)\Big|_{r=1}\cdot\mathbf{t} = \mathrm{D}_{0,r\theta} - \alpha\widetilde{\mathrm{D}}_{0,r\theta}\Big|_{r=1} = \frac{3}{2+\gamma}\sin\theta \tag{6.62}$$

To solve for the streamfunction, we use Eq. (6.55) with the remaining boundary conditions. However, before it has been stated that the droplet shape is supposed to be already known at this stage. In such case, i.e., when the interface shape is inferred a priori, the ability to satisfy the normal stress condition (6.20) is lost (Levan and Newman, 1976), therefore in order to calculate the droplet velocity we must include another condition. We require that at the steady-state the total force applied to the droplet by the fluid is equal to the external force acting on it

$$F_{0,z} = \int_0^\pi \left[\left(-p_0 + \tau_{0,rr}\right)\big|_{r=1}\cos\theta - \tau_{0,r\theta}\big|_{r=1}\sin\theta\right]\sin\theta d\theta \tag{6.63}$$

In the present case, $F_{0,z} = 0$ because we are considering a neutrally buoyant flow and no external forces are applied to the drop. The solution for the two streamfunctions can then be shown to be given by

$$\psi_0 = 2A \left(r^2 - \frac{1}{r} \right) G_2^{-1/2} (s) \tag{6.64}$$

$$\widetilde{\psi}_0 = 3A \left(r^4 - r^2 \right) G_2^{-1/2} (s) \tag{6.65}$$

where we introduced $A = 1/[(2 + 3\alpha)(2 + \gamma)]$ for convenience. The velocity components are then obtained from Eqs. (6.47)

$$u_{0,r} = -2A \left(1 - \frac{1}{r^3} \right) \cos\theta, \quad u_{0,\theta} = 2A \left(1 + \frac{1}{2r^3} \right) \sin\theta \tag{6.66}$$

$$\tilde{u}_{0,r} = 3A \left(1 - r^2 \right) \cos\theta, \qquad \tilde{u}_{0,\theta} = -3A \left(1 - 2r^2 \right) \sin\theta \tag{6.67}$$

and the dimensionless droplet migration velocity is found to be $U_0 = 2A$. Finally, the pressure is obtained by integrating the equations of motion (Eqs. 6.35 and 6.44)

$$p = p_\infty \tag{6.68}$$

$$\tilde{p} = k_1 - 30\alpha A r \cos\theta \tag{6.69}$$

where p_∞ is the pressure at infinity and k_1 is a constant that at this stage is still unknown. By taking advantage of the above solution, it is straightforward to verify that for the prescribed conditions, i.e., in absence of inertial effects, the spherical boundary identically satisfies the normal stress balance (6.20) and the constant in Eq. (6.69) can be verified to be, $k_1 = p_\infty + 2/Ca$.

6.4 First-order perturbation solution

The problem to be solved at first order is given by Eqs. (6.61-6.62). Taking advantage of the solution for the Newtonian velocity, we can evaluate the term $\boldsymbol{f}_1 (\mathbf{u}_0) = -(1 - \beta) \nabla \cdot \left(\hat{d}_0 \mathbf{D}_0 \right)$ and apply the solution strategy for the

streamfunction differential equation provided at the end of Sect. 6.2.3 with the application of the relevant boundary conditions. Also at this stage, we shall initially assume that the spherical shape is a configuration of equilibrium for the droplet, therefore we cannot rely on the normal stress balance, instead we shall make use of the macroscopic force balance (6.63) written for the specific case under consideration. Additionally, by recalling that the viscoelastic stresses do not affect the thermocapillary process, the tangential stresses must be continuous at the interface, i.e.,

$$\boldsymbol{\tau}_{1,r\theta}|_{r=1} - \alpha \, \tilde{\boldsymbol{\tau}}_{1,r\theta}|_{r=1} = 0 \tag{6.70}$$

We find that $\boldsymbol{f}_1(\mathbf{u}_0) = 0$, and the problem is formally identical to the one solved in the previous section, with the only difference that now there are viscoelastic stresses that will affect the tangential stress through the boundary condition (6.70). The calculations required to arrive to the final solution are straightforward but rather lengthy and will be omitted here (the expression of each relevant term can be found in the appendix). The final result for the streamfunctions is found to be

$$\psi_1 = \frac{108(1-\beta)A^2}{5(\alpha+1)} \left(1 - \frac{1}{r^2}\right) G_3^{-1/2}(s) \tag{6.71}$$

$$\widetilde{\psi}_1 = \frac{216A^2(1-\beta)}{10(\alpha+1)} \left(r^5 - r^3\right) G_3^{-1/2}(s) \tag{6.72}$$

which can be used to evaluate the velocity and pressure field corrections. Despite the presence of viscoelastic stresses that affect the flow, it is interesting to note that they do not have any impact on the migration velocity of the drop, *viz.* $U_1 = 0$.

6.4.1 Account for the departure from the spherical shape on the migration velocity

Until now we have assumed that the droplet shape remains spherical. We have seen that this is verified for the Newtonian case as long as the inertial

effects are neglected. In the present context, however, the presence of viscoelastic stresses acts to deform the drop and the assumption of spherical configuration is reasonable only in the limit of vanishingly small Capillary numbers. The shape function ζ should ideally be obtained by solving Eq. (6.25); however, previously we have pointed out that its mathematical treatment is made difficult by the presence of an additional contribution proportional to $CaT(r = 1, s)$. We shall now illustrate under which conditions this term can be neglected. From the expression of the temperature at the interface provided in Sect. 6.3 it is easy to verify that the additional contribution to the normal stress balance can be safely neglected provided that the condition $1/Ca \gg 3s/(2+\gamma)$ holds. The right hand side of the previous inequality is bounded, $\max\{3s/(2+\gamma)\} = 3/2$, therefore we simply require that the Capillary number is sufficiently small to assume that the previous assumption is verified, but large enough to allow deformations. Under these assumptions, Eq. (6.25) becomes

$$\tilde{p} - p + \mathbf{n} \cdot (\boldsymbol{\tau} - \alpha\,\tilde{\boldsymbol{\tau}}) \cdot \mathbf{n} = \frac{1}{Ca}\left\{2 - 2\zeta - \frac{d}{ds}\left[\left(1 - s^2\right)\frac{d\zeta}{ds}\right]\right\} \tag{6.73}$$

which can be solved considering that ζ must satisfy the conditions

$$\int_{-1}^{1}\zeta ds = 0, \quad \int_{-1}^{1} s\zeta ds = 0 \tag{6.74}$$

These equations are the linearisation of the conditions that the droplet volume must be constant because of incompressibility, and that the centre of mass of the drop has to coincide with the origin of the coordinate system, respectively. Solution of Eq. (6.73) with the conditions (6.74) is straightforward, provided that the right hand side of equation (6.73) can be written as a sum of Legendre polynomials (Brignell, 1973). That is, if

$$\tilde{p} - p + \mathbf{n} \cdot (\boldsymbol{\tau} - \alpha\,\tilde{\boldsymbol{\tau}}) \cdot \mathbf{n} = \varphi_0 + \sum_{n=1}^{\infty}\varphi_n P_n(s) \tag{6.75}$$

the solution of Eq. (6.73) is given by

$$\zeta = \alpha_1 P_1\left(s\right) + \alpha_2\left[\frac{1}{2}s\,log\left(\frac{1+s}{1-s}\right) - 1\right] - \frac{\varphi_0}{2} + \frac{\varphi_1}{6}s\,log\left(1-s^2\right)$$
$$- \sum_{n=2}^{\infty}\frac{\varphi_n P_n\left(s\right)}{\left(2+n\right)\left(1-n\right)} \quad (6.76)$$

By application of the conditions (6.74), it can be verified that the constants α_1, α_2, φ_0 and φ_1 must be identically zero, thus

$$\zeta = -\sum_{n=2}^{\infty}\frac{\varphi_n P_n\left(s\right)}{\left(2+n\right)\left(1-n\right)} \quad (6.77)$$

At the terminal velocity of the drop $(U_0 = 2A)$ we found

$$6\left(\beta - 1\right)A^2 De_T + 4\varphi_2 De_T P_2\left(s\right) = \frac{1}{Ca}\left\{2 - 2\zeta - \frac{d}{ds}\left[\left(1-s^2\right)\frac{d\zeta}{ds}\right]\right\} \quad (6.78)$$

where $\varphi_2 = \frac{3A^2(1-\beta)(13\alpha+22)}{5(\alpha+1)}$. Using this result and applying Eq. (6.77), the expression for the drop radius (Eq. 6.24) gives

$$r = 1 + \varphi_2 Ca De_T P_2\left(s\right). \quad (6.79)$$

As we shall see, this is an equation of a prolate spheroid by virtue of the fact that $\beta < 1$ and all the other terms in the expression for φ_2 are positive.

Now we adopt a domain perturbation scheme (Joseph and Fosdick, 1972) to obtain the migration velocity correction for the deformed drop. We consider the previous flow field obtained around the spherical drop and perturb it around the small parameter $Ca De_T$

$$\mathbf{u} = \mathbf{u}^{(0)} + Ca De_T \mathbf{u}^{(1)} \quad (6.80)$$
$$\tilde{\mathbf{u}} = \tilde{\mathbf{u}}^{(0)} + Ca De_T \tilde{\mathbf{u}}^{(1)} \quad (6.81)$$

The adoption of the product $Ca De_T$ as a perturbation parameter is consistent with the fact that the function ζ goes to zero either when $De_T \rightarrow 0$, for any

156

arbitrary finite value of the Capillary number (Newtonian case), or when $Ca \to 0$, for any arbitrary finite value of the Deborah number. Therefore, the product $CaDe_T$ represents the appropriate choice for the perturbation parameter. The new correction fields, $\mathbf{u}^{(1)}$, $\tilde{\mathbf{u}}^{(1)}$ will satisfy the Stokes equations

$$E^4 \psi^{(1)} = 0 \tag{6.82}$$

$$E^4 \widetilde{\psi}^{(1)} = 0 \tag{6.83}$$

The boundary conditions should now be satisfied at $r(\theta) = 1 + \zeta(\theta)$. To first order in $CaDe_T$ they read

$$u_r^{(1)} - \varphi_2 P_2 (\cos\theta) \frac{\partial u_{0,r}}{\partial r} - 3\varphi_2 \cos\theta \sin\theta u_{0,\theta} = 0 \tag{6.84}$$

$$\tilde{u}_r^{(1)} - \varphi_2 P_2 (\cos\theta) \frac{\partial \tilde{u}_{0,r}}{\partial r} - 3\varphi_2 \cos\theta \sin\theta \tilde{u}_{0,\theta} = 0 \tag{6.85}$$

$$u_\theta^{(1)} - \varphi_2 P_2 (\cos\theta) \frac{\partial u_{0,\theta}}{\partial r} + 3\varphi_2 \cos\theta \sin\theta u_{0,r} =$$
$$= \alpha \left(\tilde{u}_\theta^{(1)} - \varphi_2 P_2 (\cos\theta) \frac{\partial \tilde{u}_{0,\theta}}{\partial r} + 3\varphi_2 \cos\theta \sin\theta \tilde{u}_{0,r} \right) \tag{6.86}$$

$$\tau_{r\theta}^{(1)} - \varphi_2 P_2 (\cos\theta) \frac{\partial \tau_{0,r\theta}}{\partial r} + 3\varphi_2 \cos\theta \sin\theta \left(\tau_{0,rr} - \tau_{0,\theta\theta} \right) =$$
$$= \alpha \left(\tilde{\tau}_{r\theta}^{(1)} - \varphi_2 P_2 (\cos\theta) \frac{\partial \tilde{\tau}_{0,r\theta}}{\partial r} + 3\varphi_2 \cos\theta \sin\theta \left(\tilde{\tau}_{0,rr} - \tilde{\tau}_{0,\theta\theta} \right) \right) \tag{6.87}$$

where these expansions are evaluated at $r = 1$ (see, e.g., Leal, 2007). By solving equations (6.82-6.83) with the above boundary conditions, we obtain the following expressions for the streamfunction

$$\psi^{(1)} = \frac{6A^3(\beta - 1)(21\alpha r^3 - 16r^3 - 30\alpha + 10)(13\alpha + 22)}{25(\alpha + 1)(3\alpha + 2)r} G_2^{-1/2}(s)$$
$$+ \frac{54A^3(\beta - 1)(13\alpha + 22)(13\alpha r^2 + 10r^2 + \alpha + 4)}{175(\alpha + 1)^2 r^3} G_4^{-1/2}(s) \tag{6.88}$$

157

$$\widetilde{\psi}^{(1)} = \frac{18A^3(\beta - 1)(13\alpha + 22)(15\alpha r^2 - 20r^2 - 21\alpha + 16)r^2}{(150\alpha^2 + 250\alpha + 100)}G_2^{-1/2}(s)$$

$$- \frac{351A^3(\beta - 1)(\alpha r^2 + 4r^2 - 15\alpha - 18)(13\alpha + 22)r^4}{1225(\alpha + 1)^2}G_4^{-1/2}(s) \quad (6.89)$$

Unlike the previous cases, now the contribution to the migration velocity is different from zero, and is found to be

$$U^{(1)} = -\frac{6A^3(1 - \beta)(13\alpha + 22)(21\alpha - 16)}{25(\alpha + 1)(3\alpha + 2)} \quad (6.90)$$

From inspection of Eq. (6.90), we realise that the correction to the droplet speed can either be positive or negative depending on the value assumed by the viscosity ratio, α, since $\beta < 1$ and the remaining terms are positive.

This correction field will further contribute to the deformation of the boundary, therefore we need to add the stresses $\boldsymbol{\tau}^{(1)}$ and $\tilde{\boldsymbol{\tau}}^{(1)}$ to the normal stress condition (6.20). The adoption of the domain perturbation technique then provides

$$\mathbf{n} \cdot \left(\boldsymbol{\tau}^{(1)} - \alpha\tilde{\boldsymbol{\tau}}^{(1)}\right)\big|_{r=1} \cdot \mathbf{n} = \tau_{rr}^{(1)} - \varphi_2 P_2\left(\cos\theta\right)\frac{\partial\tau_{0,rr}}{\partial r} - 6\varphi_2\tau_{0,r\theta}\cos\theta\sin\theta$$

$$- \alpha\left(\tilde{\tau}_{rr}^{(1)} - \varphi_2 P_2\left(\cos\theta\right)\frac{\partial\tilde{\tau}_{0,rr}}{\partial r} - 6\varphi_2\tilde{\tau}_{0,r\theta}\cos\theta\sin\theta\right) \quad (6.91)$$

We shall make use of this expression in the evaluation of the droplet shape at $O\left(CaDe_T^2\right)$.

6.5 Second-order perturbation solution

The procedure for finding the solution at $O\left(De_T^2\right)$ closely resembles the method applied in the previous case at $O\left(De_T\right)$ (i.e., also in this case, we are initially assuming $Ca \to 0$). The equations of motion are provided by Eqs. (6.53-6.54), which will be solved adopting the relevant boundary conditions (formally, the same conditions used for the first order correction specialised for the present expansion order). The solution to the problem for the two streamfunctions is given

by

$$\psi_2 = h_2\left(r, \theta\right) G_2^{-1/2}\left(s\right) + h_4\left(r, \theta\right) G_4^{-1/2}\left(s\right) + \psi_2^{part} \tag{6.92}$$

$$\widetilde{\psi}_2 = \widetilde{h}_2\left(r, \theta\right) G_2^{-1/2}\left(s\right) + \widetilde{h}_4\left(r, \theta\right) G_4^{-1/2}\left(s\right) \tag{6.93}$$

where

$$h_2 = \frac{324A^3\left(1 - \beta\right)}{25r\left(\alpha + 1\right)\left(3\alpha + 2\right)} \times$$
$$\left\{\left(\frac{-965r^3}{858} + \frac{145}{78}\right)\alpha^2 + \left[\left(\frac{-651}{286} + \beta\right)r^3 - 2\beta + \frac{9}{2}\right]\alpha \right.$$
$$\left. + \left(\frac{2}{3}\beta - \frac{9}{11}\right)r^3 - \frac{4}{3}\beta + \frac{77}{39}\right\} \tag{6.94}$$

$$h_4 = \frac{972A^3(1 - \beta)}{25(\alpha + 1)^2 r^3} \times$$
$$\left\{\left(\frac{-5r^2}{39} + \frac{245}{1053}\right)\alpha^2 + \left[\left(\beta - \frac{2008}{273}\right)r^2 - 3\beta + \frac{70498}{7371}\right]\alpha \right.$$
$$\left. + \left(-\frac{58}{7}\beta + \frac{562}{273}\right)r^2 + \frac{44}{7}\beta + \frac{26}{567}\right\} \tag{6.95}$$

$$\psi_2^{part} = \Phi_0\left(r\right)\left[\Phi_1\left(r\right)\cos^2\theta + \Phi_2\left(r\right)\right] G_2^{-1/2}\left(s\right) \tag{6.96}$$

with

$$\Phi_0 = \frac{243\left(1 - \beta\right)A^3}{5r^9\left(\alpha + 1\right)} \tag{6.97}$$

$$\Phi_1 = \left(\beta - 1\right)r^5 - \frac{5}{81}\left(\alpha + 1\right)r^3 + \frac{10}{1053}\left(\alpha + 1\right) \tag{6.98}$$

$$\Phi_2 = \frac{1}{9}\left(1 - \beta\right)r^5 - \frac{5}{81}\left(\alpha + 1\right)r^3 + \frac{80}{11583}\left(\alpha + 1\right) \tag{6.99}$$

whilst

$$\widetilde{h}_2 = \frac{756A^3\left(1 - \beta\right)r^2\left(r^2 - 1\right)}{195\alpha + 130} \tag{6.100}$$

$$\widetilde{h}_4 = \frac{972\left(\beta - 1\right)A^3\left(169\beta + 111\alpha - 58\right)\left(r + 1\right)r^4\left(r - 1\right)}{455(\alpha + 1)^2} \tag{6.101}$$

Finally, by enforcing the force balance condition, the correction to the migration velocity at this order is found to be

$$U_2 = -\frac{108A^3 \left(1 - \beta\right) \left(965\alpha^2 - 858\alpha\beta + 1953\alpha - 572\beta + 702\right)}{3575 \left(3\alpha^2 + 5\alpha + 2\right)} \tag{6.102}$$

Unlike the first order field, even in absence of deformation the above result indicates that the viscoelastic stresses at this order have an impact on the droplet speed. In particular, contrarily to the previous correction, it can be shown that, regardless the other parameters, the droplet always slows down for increasing values of the Deborah number.

6.6 Higher-order drop deformation

Taking into account the values of the streamfunctions calculated in Sect. 6.4, expression (6.91) for the normal stresses at $O(CaDe_T)$, and having already neglected all the terms that do not contribute to the deformation, for the reasons explained in Sect. 6.4.1, the normal stress balance (Eq. 6.73) can finally be written for all the contributions calculated so far as

$$4\varphi_2 De_T P_2 \left(s\right) + 10\varphi_3^{(1)} CaDe_T P_3 \left(s\right) + 10\varphi_3 De_T{}^2 P_3 \left(s\right) =$$
$$\frac{1}{Ca} \left\{ 2 - 2\zeta - \frac{d}{ds} \left[\left(1 - s^2\right) \frac{d\zeta}{ds} \right] \right\} \tag{6.103}$$

where

$$\varphi_3^{(1)} = \frac{A^3 \left(1 - \beta\right) \left(2592\alpha^2 + 4122\alpha + 1476\right) \left(13\alpha + 22\right)}{70(\alpha + 1)^2} P_3 \left(s\right) \tag{6.104}$$

$$\varphi_3 = \frac{54A^3 \left(1 - \beta\right) \left(4481\alpha^2 + 4017\alpha\beta + 5944\alpha + 5538\beta - 58\right)}{455(\alpha + 1)^2} P_3 \left(s\right) \tag{6.105}$$

while the expression for φ_2 was provided in Sect. 6.4.1. The equation describing the droplet shape finally is

$$r = 1 + \varphi_2 CaDe_T P_2 \left(s\right) - \varphi_3^{(1)} Ca^2 De_T P_3 \left(s\right) - \varphi_3 CaDe_T^2 P_3 \left(s\right) \tag{6.106}$$

Before going through the discussion of the results, it is useful to rewrite the droplet speed normalised with respect to the velocity $U_0 \equiv 2A$, in a similar fashion as in the discussion made in Chapter 5 (we recall that $2A = U_{YGB}/U_T$), *viz.*

$$\bar{U} \equiv \frac{U}{U_0} = 1 + De_T \bar{U}_1 + Ca De_T \bar{U}^{(1)} + De_T{}^2 \bar{U}_2 \qquad (6.107)$$

where

$$\bar{U}_1 = 0, \qquad (6.108)$$

$$\bar{U}^{(1)} = -\frac{3A^2(1-\beta)(13\alpha + 22)(21\alpha - 16)}{(75\alpha^2 + 125\alpha + 50)} \qquad (6.109)$$

$$\bar{U}_2 = -\frac{54A^2 (1-\beta) (965\alpha^2 - 858\alpha\beta + 1953\alpha - 572\beta + 702)}{3575 (3\alpha^2 + 5\alpha + 2)} \qquad (6.110)$$

6.7 Discussion

In the previous sections, analytical solutions for the thermocapillary viscoelastic problem have been obtained for both the spherical and for the deformed drop assuming negligible convective transport in the limit of weak viscoelastic effects adopting a perturbation approach. In particular, it has been seen that by including terms up to second order in De_T, the viscoelastic correction to the drop speed comprises two separate terms, as it is summarised by Eqs. (6.108-6.110). In order to discern between the two contributions, we first analyse the results for the spherical configuration, then we shall include the second correction in order to highlight the differences produced by shape deformations. Finally, we shall compare the analytical solution with the outcomes of the numerical computations presented in the previous chapter and other simulations specifically performed for the present purpose.

6.7.1 Viscoelastic correction for the case of a spherical drop

Before addressing the discussion of the results, it is useful to show the explicit dependence of the normalised velocity (Eq. 6.107) on the fluid parameters. Since

the quantity A depends on the viscosity and thermal conductivity ratios, α and γ respectively, we have

$$\bar{U} = \bar{U}\left(\alpha, \beta, \gamma\right) \tag{6.111}$$

Each of these parameters represents a degree of freedom for the problem, hence the subsequent discussion should be ideally carried out considering them separately. Nevertheless, due to the restrictions reported below, it is convenient to limit the discussion for selected classes of fluids.

First, we consider the case of an arbitrarily small viscosity ratio, $\alpha \to 0$, which can be achieved either when the drop phase is characterised by a finite value of the viscosity, while the continuous phase viscosity is infinitely large, or when the latter is finite and the viscosity of the droplet is close zero. Although from a mathematical stand point the two situations are equivalent, the first situation can be seen as the idealisation of the case of a liquid drop entrapped in a solid matrix. On the other side, the latter example can be seen as representative of a gas bubble embedded in a viscous or, as in the present case viscoelastic continuous phase. Extending the analysis to the thermal conductivity, we notice that $\gamma \to 0$ either when $\tilde{\kappa} \to 0$ and κ is finite, or for $\kappa \to \infty$ and finite values of $\tilde{\kappa}$. The latter condition should be regarded as the case of an exceptionally conductive continuous phase (e.g., a liquid metal) surrounding a viscous drop, while the former can be seen as representative of the case of a gas bubble surrounded by a viscous or viscoelastic liquid. Since liquid metals in usual conditions can be regarded as Newtonian (see, e.g., Lappa and Ferialdi, 2017) in the subsequent discussions the situation $(\alpha, \gamma) \to 0$ will be considered representative of the case of a gas bubble migrating in a viscoelastic fluid phase.

The opposite case, $\alpha \to \infty$, is obtained when the viscosity of the continuous phase should approaches zero, assuming a finite drop viscosity, or in the presence of a solid particle surrounded by a viscous or viscoelastic fluid. In the latter situation, no particle motion would be observed, while the other condition was shown to be inadmissible since the the analytical solution of Young et al. (1959)

seems to fail the prediction, as explained in Sect. 2.4.1. As for the thermal conductivity, although in principle the condition $\gamma \to \infty$ can be achieved assuming for the droplet phase a very large thermal conductivity, again, for example with the adoption of liquid metals, the physical problem would be rather "anomalous". Alternatively, the same condition could be obtained with a perfectly insulating continuous phase, which cannot obtained in this context for obvious motivations. For these reasons, the case $(\alpha, \gamma) \to \infty$ will not be discussed in the present context. All the remaining situations lie somewhere between the limiting cases discussed above and their behaviour will be analysed for some selected cases.

Fig. 6.1 shows the migration velocity, $\bar{U}$, when the correction term $\bar{U}^{(1)}$ is absent (i.e., in the limit of $Ca \to 0$) as a function of the Deborah number for different values of the parameter β and $\alpha = \gamma = 1$. We note that for each
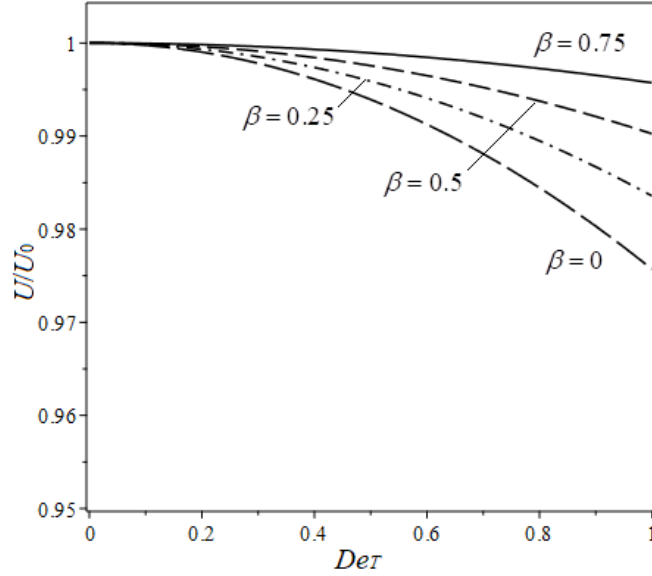
Figure 6.1: Normalised migration velocity as a function of De_T for $\alpha = 1$ and $Ca = 0$ and different values of β

value of β shown in the figure, the migration velocity decreases monotonically quadratically for increasing values of the Deborah number. We observed that smaller values of β correspond to larger velocity decrements, analogously to what was observed in Chapter 5 for a broader range of Deborah numbers and for a deformable drop. As explained before, this behaviour might be ascribed to the fact that the viscoelastic stresses, which are acting against the drop motion,

increase when the polymer contribution to the total viscosity becomes larger, assuming fixed the total viscosity. The trivial Newtonian case $\beta = 1$ is not shown.

Fig. 6.2 shows the normalised velocity for a fixed value of β for various combinations of the parameters α and γ (apart from the case of the gas bubble, γ is set to unity for the sake of simplicity). The results indicate that for the case
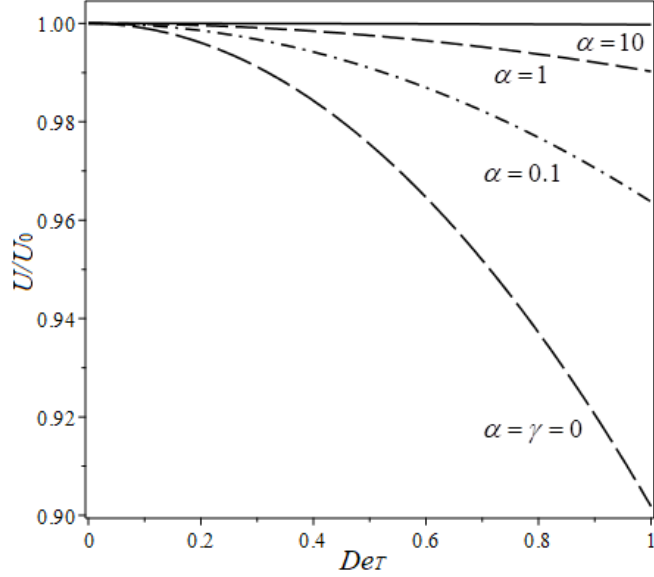
Figure 6.2: Normalised migration velocity as a function of De_T for $\beta = 0.5$ and $Ca = 0$ and different values of α

of the gas bubble, the droplet speed decreases up to a maximum of about 10% with respect to it initial value for $De_T = 0$. On the other hand, as the viscosity ratio is increased, the drop slow down in a less steep manner and, in the limit of large viscosity ratios, the Newtonian behaviour is recovered (notice that for $\alpha = 10$, the curve is already approximately flat) for the simple reason that the migration velocity approaches zero when the continuous phase viscosity becomes predominant. The simple mathematical explanation of such behaviour is due to the presence of the term A^2 appearing in Eq. (6.110), which is maximised when the viscosity and thermal conductivity ratio are equal to zero. The opposite happens when these two quantities tend to infinity. Therefore, we can infer that the elastic effects are proportional to the product ADe_T rather than De_T alone, suggesting the possibility to represent the results in an alternative manner

adopting a "reduced" Deborah number, $\bar{D}e_T = ADe_T$, which would be equivalent to consider U_{YGB} as a scaling velocity instead of U_T.

Fig. 6.3 shows the comparison between the streamlines for three different cases drawn in a frame of reference attached to the moving drop. The Newtonian flow pattern is shown on the left, while the remaining two are for $De_T = 0.9$ and $\beta = 0.1$ but different values of the viscosity ratio: $\alpha = 1$ at the center, and $\alpha = 0.25$ on the right. As expected, the Newtonian flow field is fore-and-aft symmetric since
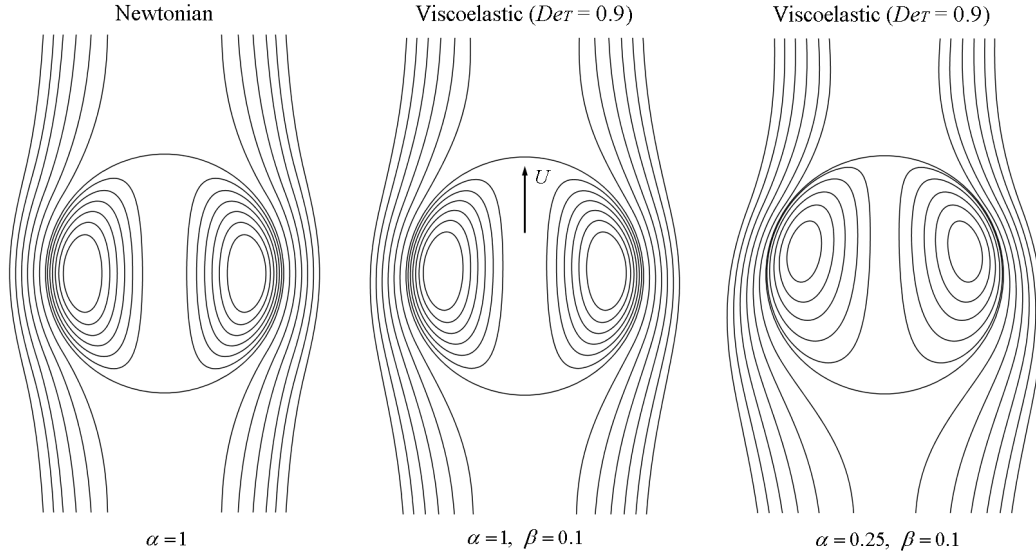
Figure 6.3: Images of the streamlines in the region of the drop for (a) the Newtonian case, (b) $\alpha = 1$ and $\beta = 0.1$ and (c) $\alpha = 0.25$ and $\beta = 0.1$. For both viscoelastic cases, $De_T = 0.9$

we are considering the idealised situation in which convective transport is exactly absent (i.e., $Re = Ma = 0$), thus the flow must be time-reversible, meaning that one would not be able to infer the direction of the motion (i.e., whether the drop is moving upward or downward, in the specific case) by inspecting the streamlines alone. On the contrary, when viscoelastic effects are considered, the streamlines are no longer symmetric. Although for both viscoelastic cases we are considering the same value of Deborah and β, it is interesting to notice the large impact played by the viscosity ratio, α. We notice, in fact, that for the first case the differences with respect to the Newtonian flow field are minimal, while as the viscosity of the drop is decreased, the streamlines are profoundly modified both inside and outside the drop. In particular, if we look at the flow field in the continuous phase

in the region behind the drop, the streamlines appear to be "compressed", while as we move further downward, the flow field tends to become more "thinned out". This behaviour might be ascribed to memory effects played by elasticity, because the polymer molecules deformation is affected by their past flow history as they move around the drop with direct consequences on the normal stress distribution around the drop. As explained before, the large difference obtained when the same Deborah and same β are assumed, is due to the presence of the term A in the equations of the streamfunction (Eqs. 6.71-6.72 at first order, and Eqs. 6.92-6.93 at second order in De_T).

6.7.2   Account for the departure from the spherical shape

In the present section we include into the analysis the correction to the migration velocity which depends on the product $CaDe_T$ (expression 6.109), thus shape deformations are allowed as long as the Capillary number is not zero.
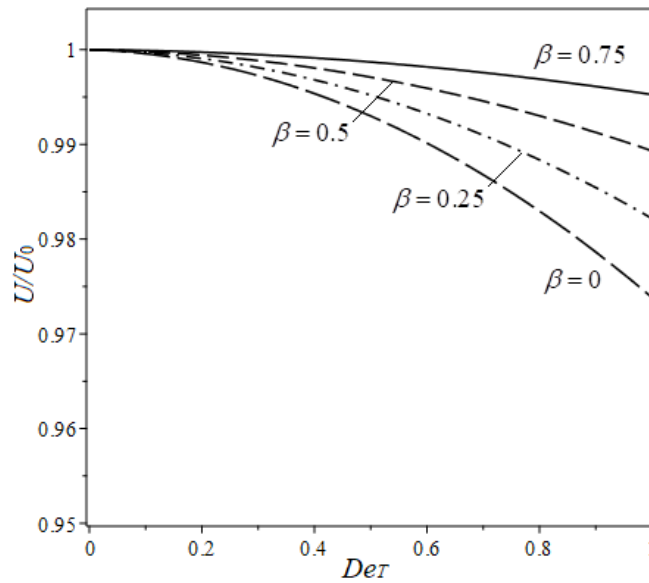
Figure 6.4: Normalised migration velocity as a function of De_T for $\alpha = 1$ and $Ca = 0.2$ and different values of β

Fig. 6.4 shows the normalised migration velocity as a function of the Deborah number for $\alpha = \gamma = 1$, $Ca = 0.2$ and different values of β. From a direct comparison with Fig. 6.1, we do not notice substantial differences. Also in this case, the velocity decreases monotonically as De_T^2 (although now the correction comprises

166

the linear term in De_T which accounts for the departure from the spherical shape through the presence of Ca) and to smaller values of β correspond larger velocity variations. In particular, it was found that the relative difference between the two conditions for the case of the maximum relative velocity decrement (i.e., for $\beta = 0$ and $De_T = 1$) is about 0.2%, showing that when the two phases have similar viscosities and thermal conductivities, the effect of the deformation on the migration velocity is negligible. In fact, the small difference is essentially due to the fact that for those conditions, the departure of the droplet's shape from spherical are hindered by the presence of the terms dependent on A appearing in the equation for the shape function (6.106) through the functions φ_i. Contrarily, when we look
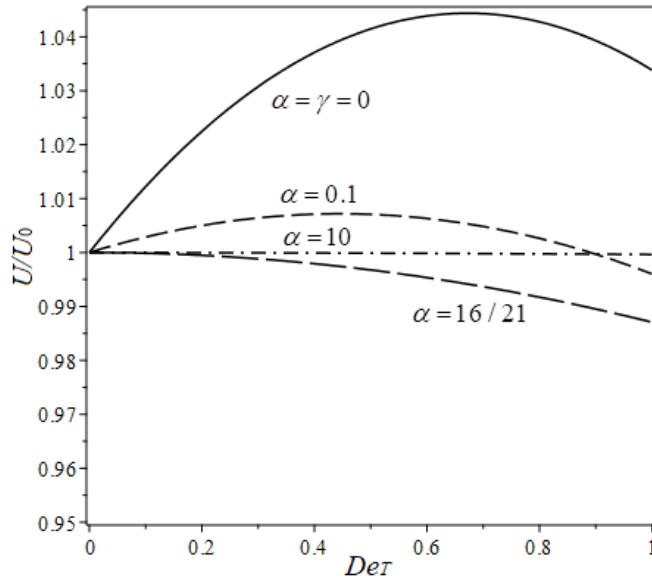
Figure 6.5: Normalised migration velocity as a function of De_T for $\beta = 0.5$ and $Ca = 0.2$ for different values of α

at the trends for fixed β (equal to 0.5 in the present example) considering α as a parameter (see, Fig. 6.5), the difference with respect to the previous case in absence of deformations becomes striking. We notice, in fact, that for these particular values of the viscosity ratio, the velocity migration initially increases with respect to the limit given by the velocity provided by Eq. (2.65), reaches a maximum and then decreases. From a mathematical point of view, such behaviour is due to the presence of the term $(21\alpha - 16)$ appearing in Eq. (6.109). Since the sign of the other terms is fixed regardless the values assumed by each variable,

this term obviously reverts its sign depending on the value of the viscosity ratio. From a physical point of view however, the justification of this behaviour seems to be quite involved. In the following we propose a possible interpretation of this unexpected behaviour. In Sect. 6.7.1 we highlighted the remarkable influence played by the normal stresses on the flow pattern, especially when the viscosity ratio becomes relatively small. In the previous examples no deformations were allowed, thus the only effect of the normal stress distribution was to modify the exterior flow field and consequently the interior one through the stresses exerted around the drop boundary. In the present case, however, the distribution of the normal stresses acts to modify both the flow field and the droplet shape with the direct consequences for the hydrodynamic resistance to the particle's motion. We have observed that the first order shape function always provides prolate ellipsoid particle shapes. Furthermore, from the inspection of the term φ_2 appearing in Eq. (6.79), the drop becomes more elongated for smaller values of α through the term proportional to A. Therefore, we might infer that after a certain "critical" viscosity ratio (specifically, for $\alpha < 16/21$), the resistance to the motion offered by the deformed droplet becomes smaller due to the reduced cross-sectional area of the drop, providing the initial velocity increment shown in Fig. 6.5. This hypothesis is further confirmed by the fact that the extent of the maximum increment decreases by increasing α and the relative maximum moves towards smaller De_T. Keeping α fixed, for further increments of De_T the subsequent droplet slow down can be justified by the increased contribution of the viscoelastic stresses that after a certain threshold starts to prevail against the above mentioned reduction of the hydrodynamic resistance.

6.7.3 Comparison with the numerical solutions

In this section we compare some of the results presented in the previous section with the numerical computations obtained for the conditions similar to those adopted in Chapter 5. In particular, we ran a series of additional simulations adopting the Oldroyd-B model for $Re = 10^{-4}$ and $Ma = 10^{-5}$ for an increased domain (both the horizontal and vertical dimensions have been increased by a

factor of 1.5 with respect to the case examined in Chapter 5) to reduce possible effects of the boundaries on the droplet motion. Additionally, as it has anticipated in the introductory part of this section, we shall make use of some of the previous calculations of Chapter 5 to make further comparisons.
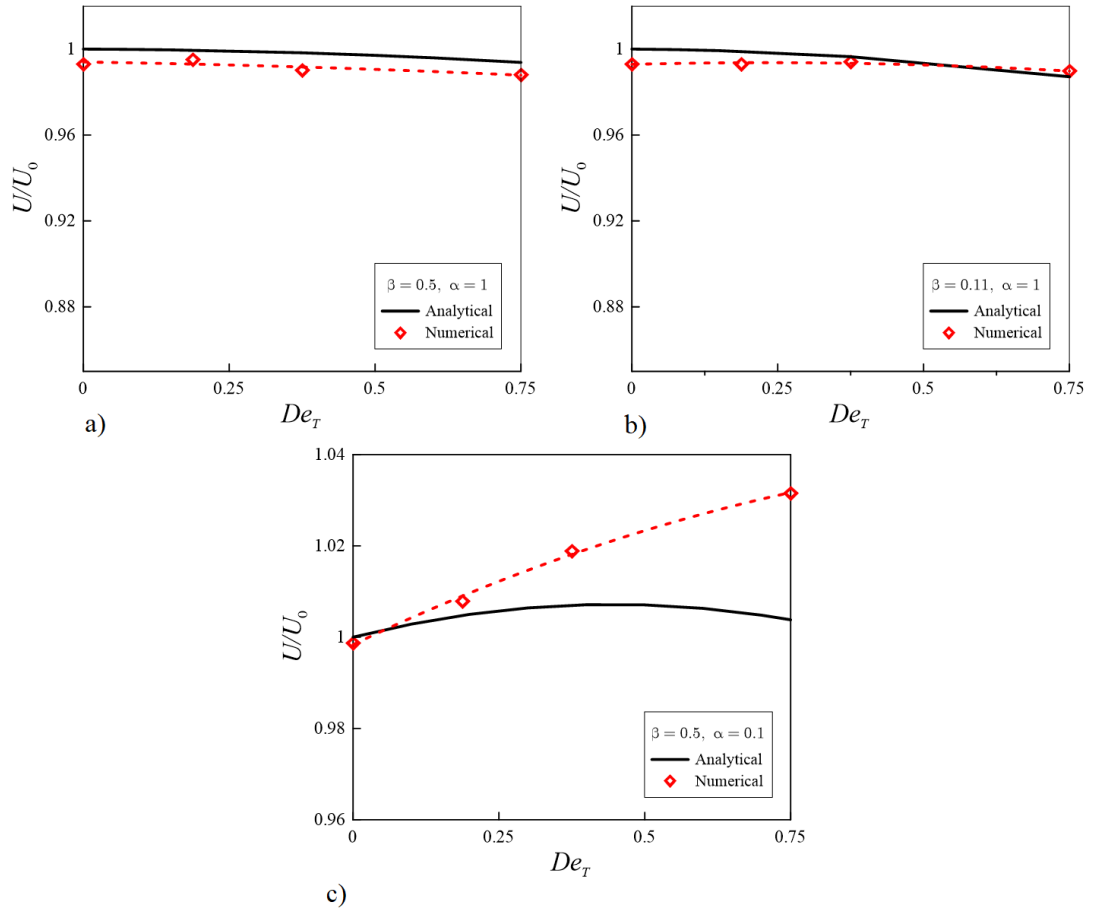
Figure 6.6: Comparison between the numerical simulations and the analytical solution in terms of normalised velocity as a function of the Deborah number, for the cases (a) $\alpha = \gamma = 1$ and $\beta = 0.5$, (b) $\alpha = \gamma = 1$ and $\beta = 0.11$, (c) $\alpha = 0.1$, $\gamma = 1$ and $\beta = 0.5$

Fig. 6.6 shows the comparison between the normalised migration velocity as a function of De_T for three selected cases. Figs. 6.6a,b show the normalised velocity as a function of the Deborah number for two different values of β, $\alpha = \gamma = 1$ and $Ca = 0.2$. Although the results of the numerical experiments are slightly scattered due to numerical errors (the dashed red lines represent fitting curves), the results show a fairly good agreement between the two approaches. In Fig. 6.6c, the comparison has been made for the case $\beta = 0.5$, $\alpha = 0.1$ and $\gamma = 1$ adopting the same Capillary number considered before. The results

indicate qualitative agreement, as witnessed by the fact that both the analytical and numerical solutions initially increase with De_T. Nevertheless, the numerical simulations seem to overestimate the trend provided by the analytical solution. Such discrepancy might be ascribed to the fact that, as explained in Chapter 5, the present numerical approach shows lack of accuracy in predicting the droplet shape even in the absence of viscoelastic effects (cf. the data shown in Table 5.3). Additionally, observing that the first order shape function depends on A^2 through the term φ_2 appearing in Eq. (6.79), the source of numerical error arising from the interpolation of the two viscosities through Eq. (2.75) can have a non-negligible impact on the migration velocity. When $\alpha = 1$, on the contrary, the deformations are limited and the source of error mentioned above is absent, as witnessed by the better agreement shown by the data in Figs. 6.6a,b.
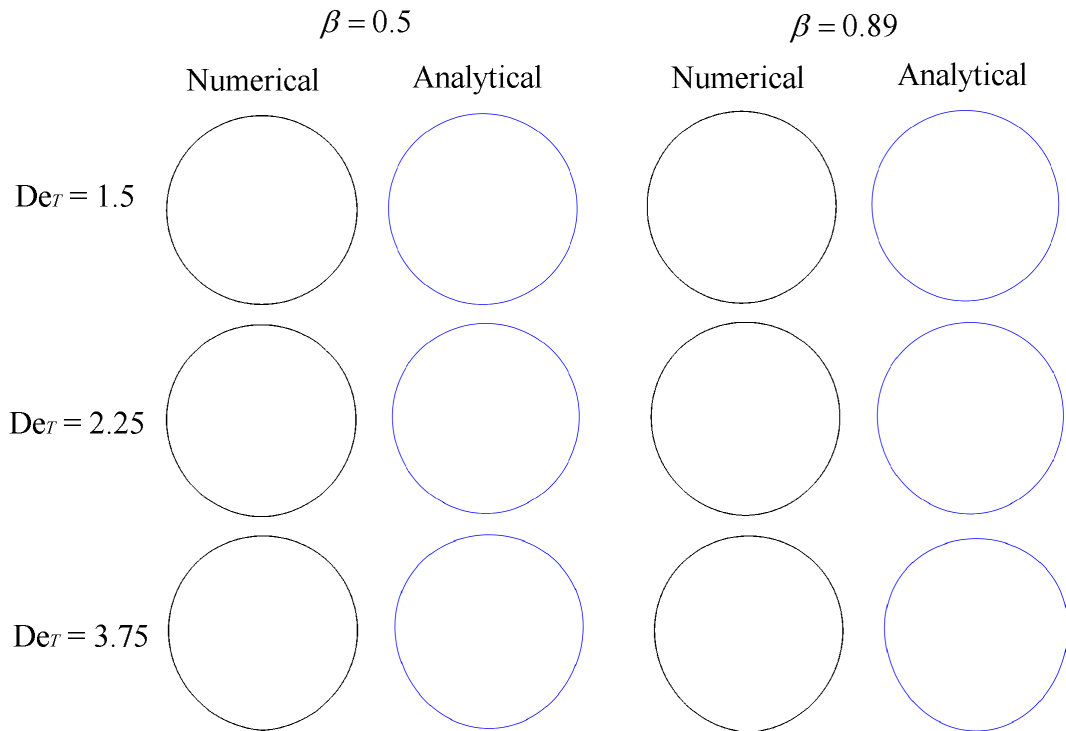
Figure 6.7: Comparison between the droplet shapes obtained from the simulations and those obtained with the analytical approach for $\beta = 0.5$ and $\beta = 0.89$ and three different Deborah numbers, $De_T = 1.5, 2.25, 3.75$.

Additionally, we present the comparison between the droplet shapes obtained from the simulations discussed in Chapter 5 for the case of the Oldroyd-B model, with the mathematical prediction provided by Eq. (6.106) (see, Fig. 6.7). From a

direct inspection of the shapes depicted in the figure, there appears to be a good agreement for the smallest Deborah number considered. For $De_T = 3.75$ however, the shapes obtained from the numerical computations show the characteristic "pointed tail", which is not present in the analytical solution. Nevertheless, the perturbation solution provided shapes that are not fore-and-aft symmetric, which is in qualitative agreement with the numerical experiments. It is worth emphasising though, that although the condition $CaDe_T < 1$ is verified for all the cases, the condition $De_T < 1$ is nonetheless violated, thus one would expect a certain discrepancy. Nevertheless, we have observed that the reduced Deborah number ADe_T represents a more appropriate choice (as confirmed by the dependence on the parameter $A < 1$). Thus, even though $De_T > 1$, for the case shown in Fig. 6.7, $ADe_T < 1$ and the perturbation method remains applicable.

6.8   Conclusions

The analytical treatment of the steady-state thermocapillary motion of a Newtonian droplet translating in an otherwise quiescent Oldroyd-B fluid has been conducted adopting perturbation techniques in the limit of small Deborah numbers. The analysis is carried out assuming the absence of any convective transport effects, ignoring inertia and decoupling the solution of the energy equations from the velocity field. Specific non-Newtonian correction formulae for the droplet migration velocity are obtained in the limit of $Ca \to 0$, i.e., assuming a spherical drop, as well as in the presence of small boundary deformations by allowing the Capillary number to be small, but finite. Equations describing the droplet shape are also provided. In the absence of deformation, the results show that the migration speed always decreases monotonically with De_T irrespective of the other parameters. In particular, it was shown that when the viscosity and thermal conductivity of the drop become much smaller than their values on the continuous phase, the effect of elasticity becomes increasingly more important and the migration velocity is significantly decreased. When the shape deviations are allowed, the velocity, evaluated as a function of the Deborah number, either

initially increases with respect to the Newtonian value or behave in a manner qualitatively similar to that observed for the spherical particle depending on the specific value of the viscosity ratio. The hypothesis that the reduction of the drop cross-sectional area induced by the reduction of the viscosity ratio might impact the hydrodynamic resistance to the extent that the velocity can become larger than U_{YGB} was proposed. Finally, we reported a comparison with some of the simulations performed in Chapter 5, as well as with other numerical experiments carried out adopting an increased domain. The analysis shows that when the two phases are characterised by the same viscosity, the droplet migration velocity obtained from the numerical computations are in good agreement with the analytical predictions. On the contrary, for smaller values of α, the numerical approach seems to overestimate the migration velocity, although qualitatively similar trends are observed. The comparison in terms of droplet shapes is carried out and qualitative agreement between the outcomes of the two approaches is observed.

Chapter 7

Conclusions and future directions

In the present work the study of the thermocapillary motion of deformable droplets in complex flow configurations for both Newtonian and viscoelastic fluids was assessed by means of numerical and analytical techniques. A solver based on a hybrid Level Set-Volume of Fluid methodology available in OpenFOAM was developed with the specific intention to investigate particular aspects of the thermal Marangoni migration phenomenon which were previously little understood or almost entirely unexplored. The code was first tested against the well-established analytical solution of Young et al. (1959), which holds for Newtonian fluids under the assumption of negligible convective transport and unbounded flow. Then, the capability of the solver on handling more challenging flow conditions (i.e., including the presence of convective transport phenomena) was evaluated considering the experimental observations obtained in microgravity conditions by Hadland et al. (1999). The results of the tests have highlighted the reliability of the code on handling the specific problems considered.

In the context of future work, it is worth emphasising that the current implementation is still susceptible to further improvements, which would enhance the efficiency and the accuracy of the solver and would allow the possibility to investigate flows in different configurations. In particular, throughout this thesis it was pointed out that on modelling the effect of the temperature on the interfacial tension, the term that takes into account the variation of the capillary force along the interface was not included in the numerical implementation. Although in certain flow conditions such simplification does not lead to inaccurate results, as

confirmed by the validations discussed in Chapter 3, in other situations it might be a source of non-negligible errors, as it was pointed out during the discussion of the results presented in Chapters 5 and 6. The implementation of the term under discussion would simultaneously lead to a better prediction of the droplet interface, which in turn would bring substantial improvements in the evaluation of the migration speed in all those problems where this latter quantity is strongly affected by interface deformations. Moreover, at this stage the solver cannot rely on the adaptive mesh refinement capability if used in parallel calculations. Since the possibility to use both features (adaptive meshing and parallel computation) arguably would contribute to reduce significantly the time of computation, this is a very interesting prospect for future work.

Finally, it is worth pointing out that the present hybrid LS-VOF implementation, as in the version of Yamamoto et al. (2016), was found to be inadequate to deal with problems involving interfaces in contact with solid boundaries. Indeed, a number of works on the thermocapillary motion of droplets nowadays is focused on problems involving contact angles, due to their potential to be exploited for applications on Earth (see, e.g., microfluidic applications). For such reason, it is highly desirable to fill this gap in order to increase the potential of the thermocapillary solver in the context of future lines of investigation.

In all the numerical investigation considered in this work, the same geometric constrains adopted by Hadland et al. (1999) were used, with the only exception of the problems discussed in the last section of Chapter 4, where converging and diverging channels were considered. The effect of the solid boundaries on the migration phenomenon was investigated in different off-centre conditions. The problem was analysed using different configurations, to consider the effect of wall proximity, by releasing the drop in positions progressively closer to a single wall and next to a corner for a broad range of Marangoni numbers. Both adiabatic and conductive walls were adopted to assess the impact of the presence of possible wall heat fluxes on the dynamics of the droplet. In the absence of wall heat fluxes and for relatively small Reynolds and Marangoni numbers, the temperature profile remains quasi-linear for all the off-centred configurations. Consequently,

the thermocapillary stresses tend to be symmetrically distributed around the surface of the drop, and the resulting driving force is mainly in the direction of the applied temperature gradient. For larger values of Ma, the migration speed was found to decrease relatively to case where the drop was released exactly at the centre of the channel. The results have shown that the migration velocity comprises two separate contributions. In addition to the component generated by the mean temperature gradient, i.e., directed from the cold side to the hot side, another component arising from the distortion of the temperature field around the drop that "pulls" the particle toward the centre of the channel was observed. The additional contribution was found to be related to the distortion of the thermal field established between the drop and the adjacent wall, which in turn generates a component of the thermocapillary force directed from the wall toward the center of the channel. For the case of the conductive wall, the migration phenomenon was found to be very sensitive to the value of the Marangoni number. For relatively small Ma, the behaviour of the drop is found to be essentially unvaried relative to the situation in which adiabatic boundaries were considered. For large Marangoni numbers, on the contrary, the distortion of the thermal field generates a thermocapillary component of the force that pulls the droplet toward the conductive wall, which eventually leads to the collision of the drop with the boundary.

Subsequently, we addressed the thermocapillary problem adopting converging and diverging containers for both small and moderately large Marangoni numbers. When convective effects are negligible, we observed that the velocity distribution along the extension of the channel is essentially logarithmic, and the drop accelerates or slows down relative to the case of a linear temperature profile depending on the concavity assumed by the temperature distribution, i.e., if the channel is converging or diverging, respectively. On the other hand, when convective transport is important, the temperature distribution established in the region of the thermal boundary layer, i.e., next to the drop interface, is dictated by the effect of convection rather than the distortion imposed by the geometric configuration of the domain. In such a case, the migration process is observed to be equivalent for

the two configurations until the blockage effect offered by the narrowing channel in the converging arrangement leads to an unavoidable velocity decrease.

In the second part of the thesis, viscoelastic effects were taken in consideration by modelling the continuous phase employing two different viscoelastic models. The problem was initially tackled numerically, then analytical solutions were derived for the steady-state axisymmetric flow assuming an unbounded domain. In both cases, negligible inertia and convective transport of energy were postulated. With regard to the numerical experiments, for relatively small Deborah numbers the viscoelastic phase was modelled adopting the Oldroyd-B constitutive law, while, for flow conditions where this model was found to be no longer applicable, the non-linear model (FENE-CR) of Chilcott and Rallison (1988) was employed. For the case of the Oldroyd-B model, two different flow configurations were investigated. First, the problem was solved assuming an infinitely dilute solution (i.e., $c \to 0$), which allowed to study the deformation of the polymer filament in a flow that essentially behaves in a Newtonian-like manner. Subsequently, the analysis was repeated for finite values of the polymer concentration, where viscoelastic stresses are produced. The numerical simulations have highlighted that regardless of the values of the concentration, larger molecule deformations always occur in a narrow region next to the rear stagnation point, where the flow is essentially a uniaxial straining flow. On the contrary, the value of concentration was observed to have non-negligible influence on the extent of the deformation, which was found to decrease as the parameter c is increased (i.e., the largest deformations occur when the viscoelastic stresses are vanishingly small). In terms of droplet velocity, the computations obtained for finite values of the polymer concentration have shown that the droplet slows down in a quadratic manner with De_T, and that to larger values of c correspond smaller velocities. Due to the presence of a singularity in the solution of the Odroyd-B model, the maximum Deborah number employed was limited to $De_T = 3.75$. For larger values of De_T, the viscoelastic behaviour was modelled with the FENE-CR model. Similarly to the previous situation, the droplet speed decreases monotonically for increments of the Deborah number. However, in such a case the trends observed

176

were qualitatively different from those obtained with the Oldroyd-B model. The different behaviour, however, should be ascribed to the different flow conditions, rather than to the adoption of different models. Finally, in terms of interface deformation, we observed that the droplet always deforms in a prolate manner independently of the values assumed for the various parameters and, for sufficiently large values of De_T it assumes a characteristic "tear-drop" shape with the presence of a pointed tail.

In the last chapter of the thesis, the viscoelastic problem was tackled by means of perturbation techniques in the limit of small Deborah numbers and absence of confinement. Corrective formulae for the migration speed were obtained assuming first a non-deformable spherical drop and then allowing for small deformations. For the spherical particle, it has been observed that the droplet speed always decreases with the square of the Deborah number regardless of the values assumed for all the material parameters, which were found to be influential only on the extent of the velocity decrease. Specifically, for the case of a gas bubble, i.e., the situation in which the particle viscosity and thermal conductivity are much smaller than those assumed by the continuous phase, the effect of elasticity is maximised and the particle migration velocity is largely reduced. In the presence of interface deformations, the migration velocity, plotted as a function of De_T, either initially speed up or slows down relative to the Newtonian situation depending on the value assumed by the viscosity ratio α. It was observed, in fact, the presence of a "critical" value of α which reverts the sign of the first order velocity correction. Such behaviour seems to be ascribed to the competition between viscoelasticity, that hinders the migration speed, and the reduced hydrodynamic resistance resulting from the reduction of the cross-sectional area of the prolate drop, which has been found to be inversely proportional to the viscosity ratio. Comparisons between the analytical solution and numerical computation showed that when the two fluids are characterised by the same viscosity and same thermal conductivity, the results of the computations are in good agreement with the analytical solution. On the contrary, for a specific computation obtained for a value of the viscosity ratio smaller than the critical one, the agreement is only

qualitative, the difference being ascribed to the limitation of the specific interface capturing methodology discussed in Chapter 5 and possible source of errors stemming form the presence of discontinuities in the material properties (i.e., viscosity and thermal conductivity) and from neglecting the dependence of the capillary force from the temperature. In terms of shape deformations, both approaches have shown that the drop initially assumes the configuration of a prolate ellipsoid, then, when the product $CaDe_T$ is further increased, a loss of fore-and-aft of symmetry was observed. The presence of the cusped tail was detected only in the results of the numerical simulations.

Performing experimental campaigns is suggested on future works to verify the accuracy of the proposed investigations, especially in the case of the migration in viscoelastic fluids. This is a challenging task, as it would ideally be performed in reduced gravity environments, which can be extremely complicated and expensive as they required specialised facilities not widely available. The possibility to resort to microfluidic applications appears to be a valid alternative to the above mentioned experiments in microgravity. New lines of inquiry are currently under consideration at the James Weir Fluid Laboratory to design and perform experiments in microfluidic chips involving non-Newtonian fluids.

Bibliography

Albadawi A., Donoghue D. B., Robinson A. J., Murray D. B., Delauré Y. M. C., (2013), Influence of surface tension implementation in volume of fluid and coupled Volume of Fluid with Level Set methods for bubble growth and detachment, International Journal of Multiphase Flow, 53, 11-28.

Arienti M. and Sussman M., (2017), A numerical study of the thermal transient in high-pressure diesel injection, International Journal of Multiphase Flow, 88, 205-221.

Astarita G and Apuzzo G., (1965), Motion of gas bubbles in non-Newtonian liquid, AIChE J., 11, 815-820.

Balasubramaniam R. and Chai A.-T., (1987), "Thermocapillary migration of droplets: An exact solution for small marangoni numbers", J. Colloid Interface Sci., 119, 531-538.

Balasubramaniam R. and Subramanian R. S, (2000), The migration of a drop in a uniform temperature gradient at large Marangoni numbers, Physics of Fluids, 12, 733-743.

Balasubramaniam R., Lacy C.E., Wozniak G., Subramanian R.S., (1996), Thermocapillary migration of bubbles and drops at moderate values of the Marangoni number in reduced gravity, Physics of Fluids, 8, 872-880.

Balasubramaniam R., Lacy, C. E., Woniak, G., and Subramanian R. S. (1996) Thermocapillary migration of bubbles and drops at moderate values of the Marangoni number in reduced gravity, Physics of Fluids. 8, 872-880.

Balcázar N., Rigola J., Castro J., Oliva A., (2016), A level-set model for thermocapillary motion of deformable fluid particles, International Journal of Heat and Fluid Flow, 62, 324-343.

Batchelor, G K. (1967) An introduction to fluid dynamics. Cambridge, England: Cambridge University Press, 615 p.

Berberović, van Hinsberg N. P., Jarkirlić S., Roisman L. V., Tropea C., (2009), Drop impact onto a liquid layer of finite thickness: Dynamics of the cavity evolution, Phyical. Review E, 79, 036306.

Bird R B, Armstrong R C and Hassager O. (1987), Dynamics of polymeric liquids. Volume 1. Fluid mechanics. New York: Wiley, 576 p.

Brackbill, J.U., Kothe, D. B., Zemach, C., (1992), A continuum method for modeling surface tension. Journal of Computational Physics, 100, 335-354.

Brady P. T., Hermann M., Lopez J. M., (2011), Confined thermocapillary motion of a three-dimensional deformable drop, Physics of Fluids, 23, 022101.

Braun, B., C. Ikier, H. Klein, (1993), Thermocapillary Migration of Droplets in a Binary Mixture with Miscibility Gap during Liquid, Liquid phase Separation under Reduced Gravity, J. Colloid Interface Sci., 159, 515.

Brignell A. S., (1973), The deformation of a liquid drop at small Reynolds number, Journal of Mechanics and Applied Mathematics, 26, 99–107.

Brunet P., Baudoin M., Bou Matar O., Zoueshtiagh F., (2010), Droplet displacement an doscillation induced by ultrasonic surface acoustic waves: A quantitative study, Physical Review E, 81, 036315.

Calderbank P.H., (1967), Gas absorption from bubbles, Chem. Eng., 45, 209 p.

Calderbank P.H., Johnson, D.S.L., and Loudon, J., (1970), Mechanics and mass transfer of single bubbles in free rise through some Newtonian and non-Newtonian liquids, Chem. Eng. Sci., 25, 235-256.

Chhabra RP (2006), Bubbles, drops and particles in non-Newtonian fluids. 2nd edn. CRS Press.

Chilcott, M. D. and Rallison, J. M., (1988) Creeping flow of dilute polymer solutions past cylinders and spheres. J Non-Newton Fluid Mech, 29, 381-432.

Chinyoka T., Renardy Y., Renardy M. and Khismatullin D.B., (2005), Two-dimensional study of drop deformation under simple shear for Oldroyd-B liquids, J. Non-Newtonian Fluid Mech., 130, 45–56.

Choi SK., Nam HY., Cho M., (1994), Systematic comparison of finite-volume calculation methods with staggered and nonstaggered grid arrangements. Numer Heat Transfer, Part B 25, 205–221

Choi SK., Nam HY., Cho M., (1994a), Use of staggered and nonstaggered grid arrangements for incompressible flow calculations on nonorthogonal grids. Numer Heat Transfer, Part B 25, 193–204.

Coelho P., Pereira J.C.F., and Carvalho M.G., (1991), Calculation of laminar recirculating flows using a local non-staggered grid refinement system, Int. J. Num. Meth. Fluid, 12(6):535-557.

Deshpande S. S., Anumolu L., Trujillo M. F., (2012), Evaluating the performance of the two-phase flow solver interFoam, Computational Science and Discovery, 5 014016.

Djordjević G. B. and Milovanović G. V., (2014), Special classes of polynomials. Leskovac, Serbia: University of Nis Faculty of Technology.

Favero J. L., Cardozo N. S., Secchi A. R. and Jasak H, (2010), Simulation of Free Surface Viscoelastic Fluid Flow Using the viscoelasticInterFoam

Solver," in 20th European Symposium on Computer Aided Process Engineering, pp. 31–36.

Fletcher C. A. J., (1991), Computational techniques for fluid-dynamics, (Springer Verlag, Berlin.

Furlani E. P, Price B. G., Hawkins G. and Lopez A., (2006), Thermally induced Marangoni instability of liquid microjets with application to continuous inkjet printing, Proc. NSTI Nanotechnol. 2, 534.

Fuster D., Bagué A., Boeck T., Le Moyne L., Leboissetier A., Popinet S., Ray P., Scardovelli R. and Zaleski S., (2009), Simulation of primary atomization with an octree adaptive mesh refinement and VOF method, International Journal of Multiphase Flow, 35, 550–565.

Galusinski C. and Vigneaux P., (2008), On stability condition for bifluid flows with surface tension: application to microfluidics. J. Comput. Phys. 227, 6140–64.

Getachew D. and Rosenblat S., (1985), Thermocapillary instability of a viscoelastic liquid layer, Acta Mechanica, 55, 137-149.

Gibbs J. W., (1878) On the equilibrium of heterogeneous substances. Am J Sci. Series 3, Vol. 16, 441-458.

Grant P. S., Cantor B., Rogers S. and Katgerman L., (1990), A Computer Model for Trajectories and Thermal Profiles of Atomised Droplets in Spray Forming, Cast Metals, 3(4): 227-232.

Gueyffier D., Li J. , Nadim A., Scardovelli S., Zaleski S., (1999), "Volume of Fluid interface tracking with smoothed surface stress methods for three-dimensional flows", J. Comput. Phys., 152, 423-456.

Guo Z. and Lin P., (2015), A thermodynamically consistent phase-field model for two-phase flows with thermcapillary effects, J. Fluid Mech., 766, 226-271.

Hadamard J. S. (1911) Mouvement permanent lent d'une sphere liquide et visqueuse dans un liquide visqueux. C. R. Acad. Sci. 152, 1735-1738.

Hadland P. H., Balasubramaniam, R., Wozniak, G., Subramanian R.S., (1999) Thermocapillary migration of bubbles and drops at moderate to large Marangoni number and moderate Reynolds number in reduced gravity. Experiments in Fluids, 26, 240-248.

Haj-Hariri H., Nadim A. and Borhan A., (1990), "Effect of inertia on the thermocapillary velocity of a drop", J. Colloid Interface Sci., 140(1): 277-286.

Haj-Hariri H., Shi Q., Borhan A., (1997), Thermocapillary motion of deformable drops at finite Reynolds and Marangoni numbers, Physics of Fluids 9 (4):845-855.

Han. C. D., (1981), Multiphase Flow in Polymer Processing, Academic Press, Technology & Engineering, 459 pages.

Happel J. and Brenner H., (1983), Low Reynolds Number Hydrodynamics, (Martinus Nijhoff, The Hague).

Harlen O. G., (2005), The negative wake behind a sphere sedimenting through a viscoelastic fluid, J. Non-Newtonian Fluid Mech., 108, 411-430.

Harper J.F. and Moore D.W., (1968), The motion of a spherical liquid drop at high Reynolds number, Journal of Fluid Mechanics, 32, 367–391.

Hassager, O., (1979), Negative wake behind bubbles in non-Newtonian liquids, Nature, 279, 402.

Hirt, C. W., Nichols, B. D., (1981) Volume of Fluid (VOF) method for the dynamics of free boundaries. J. Computaional Physics, 39, 201-225.

Hu K., He M., Chen Q., and Liu R., (2018), Effect of gravity on the stability of viscoelastic thermocapillary liquid layer, International Journal of Heat and Mass Transfer, 123, 776-786.

Jang D.S., Jetli R., Acharya S. (1986), Comparison of the PISO, SIMPLER and SIMPLEC algorithms for the treatment of the pressure-velocity coupling in steady flow problems. Numer Heat Transfer 10, 209–228.

Jeffreys H. (1929) The Earth (Cambridge University Press) p. 265.

Jiménez-Fernández, J. and Crespo, (2002), The thermocapillary migration of gas bubbles in a viscoelastic fluid. Microgravity Sci. Technol., 13, 33.

Joseph, D. D. and Fosdick, R. L., (1972), The free surface on a liquid between cylinders rotating at different speeds. Part 1. Arch. Rat. Mech. Anal. 49, 321–350.

Karbalaei, A., Rangananthan, K., Jin Cho, H. (2016) Thermocapillarity in microfluidics-A review. Micromachines. 7, 13.

Kittur M. G. and Huston R. L., (1989), Mesh refinement in finite element analysis by minimization of the stiffness matrix trace. NASA Contractor Report 185170, Technical Report 91-C-019.

Kramers, H. A.(1946) The behaviour of macromolecules in inhomogeneous flow, J. Chem. Phys. 14, 415–424.

Landau L. D. and Lifshitz E. M., (1959), Course of Theoretical Physics, vol. 6: Fluid Mechanics, Pergamon Press.

Lappa M., (2004), Fluids, Materials and Microgravity: Numerical Techniques and Insights into the Physics, 538 pages, Elsevier Science (2004, Oxford, England).

Lappa M., (2005), Coalescence and non-coalescence phenomena in multi-material problems and dispersed multiphase flows: Part 2, a critical review of CFD approaches, Fluid Dynamics & Materials Processing, 1, 213-234.

Lappa M., (2005a) Assessment of VOF Strategies for the analysis of Marangoni Migration, Collisional Coagulation of Droplets and Thermal

wake effects in Metal Alloys under Microgravity conditions, Computers, Materials & Continua, 2(1), 51-64.

Lappa M., (2005b), Coalescence and non-coalescence phenomena in multi-material problems and dispersed multiphase flows: Part 2, a critical review of CFD approaches, Fluid Dynamics & Materials Processing, 1, 213-234.

Lappa M., and Ferialdi H., (2017), On the Oscillatory Hydrodynamic Instability of Gravitational Thermal Flows of Liquid Metals in Variable Cross-section Containers, Physics of Fluids, 29, 064106.

Leal G. L., (2007), Advanced transport phenomena : fluid mechanics and convective transport processes. Cambridge University Press, 912 pages.

Leonard B. P., (1979), A stable and accurate convective modelling procedure based on quadratic upstream interpolation. Computer Methods in Applied Mechanics and Engineering, 19, 59-98.

Levan, M. D. and Newman, J., (1976), The effect of surfactant on the terminal and interfacial velocities of a bubble or drop. AIChE J. 22, 695.

Liu H. and Zhang Y., (2015), Modelling thermocapillary migration of a microfluidic droplet on a solid surface, Journal of Computational Physics, 280, 37-53.

Liu H., Valocchi A. J., (2013), Phase-field based lattice Boltzmann finite difference model for simulating thermocapilarry flows. Physical Review E, 87, 013010.

Liu H., Wu L., Ba Y., Xi G., (2017), A lattice Boltzmann method for axisymmetric thermocapillary flows, International Journal of Heat and Mass Transfer, 104, 337-350.

Liu H., Zhang Y., Valocchi A. J., (2012), Modeling and simulation of thermocapillary flows using lattice Boltzmann method, Journal of Computational Physics, 231, 4433-4453.

Liu, Y.J., Liao, T.Y., and Joseph, D.D., (1995), A two-dimensional cusp at the trailing edge of an air bubble rising in a viscoelastic liquid, J. Fluid Mech., 304, 321.

Ma X., Balasubramaniam R., Subramanian R. S., (1999), Numerical simulation of thermocapillary drop motion with internal circulation, Numerical Heat Transfer, 35, 291-309.

Marangoni C. (1871). Ueber die Ausbreitung der Tropfen einer Flussigkeit auf der Oberfl ache einer anderen. Ann. Phys. Chem. 143:337-54.

Martinez-Mardones J. and Perez-Garci C., (1990), Linear instability in viscoelastic fluid convection, Journal of Physics: Condensed Matter, 2, 5.

Meyyappan M., Wilcox W. R., Subramanian R. S., (1981), Thermocapillary migration of a bubble normal to a plane surface, Journal of Colloid and Interface Science, 83, 199-208.

Mhatre M. V. and Kintner R. C., (1959), Fall of liquid drops through pseudoplastic liquids, Ind. Eng. Chem. 57, 865–867.

Mirjalili, S., Jain, S. S. and Dodd, M., (2017), Interface-capturing methods for two-phase flows: An overview and recent developments. Annual Research Briefs, 117–135.

Morrison, F. A. Understanding Rheology, Oxford University Press, New York, 2001.

Moukalled F., Mangani L. and Darwish M., (2016), The Finite Volume Method in Computational Fluid Dynamics - An Advanced Introduction with OpenFOAM and Matlab, Springer International Publishing, 2016, New York.

Nadim A., Haj-Hariri H. and Borhan A., (1990), "Thermocapillary migration of slightly deformed droplets", Part. Sci. Technol., 8, 191-198.

Nguyen N., Ng K. M., Huang X., (2006), Manipulation of ferrofluid droplet using planar coils, Applied Physics Letters, 89, 052509.

Noh, W. F., Woodward, P., (1979) (SLIC) Simple Line Interface Calculation, Proceedings of the Fifth International Conference on Numerical Methods in Fluid Dynamics.

Oldroyd, J. G. (1950). On the Formulation of Rheological Equations of State. Proc. R. Soc. Lond. A. 200, 523-541.

Oliveira, P. J. (2009) Alternative derivation of differential constitutive equations of the Oldroyd-B type, Journal of Non-Newtonian Fluid Mechanics, 160, 40-46.

OpenFOAM User Guide (accessible online at https://openfoam.org)

Patankar S.V. and Spalding D.B., (1972), A calculation procedure for heat, mass and momentum transfer in three-dimensional parabolic flows, Int. J. Heat Mass Transfer, 15, 1787-1806.

Phan-Thien, N. (2002), Understanding viscoelasticity – Basics of rheology, Springer-Verlag.

Parmentier P., Lebon G. and Regnie V., (2000), Weakly nonlinear analysis of Bénard–Marangoni instability in viscoelastic fluids, Journal of Non-Newtonian Fluid Mechanics, 89, 63-95.

Philippoff W. (1937), The viscosity characteristics of rubber solutions, Rubber Chemistry and Technology 10, 76–104.

Pillapakkam S. B. and Singh P., (2001), A Level-Set Method for Computing Solutions to Viscoelastic Two-Phase Flow, Journal of Computational Physics, 174, 2, 552-578.

Pillapakkam S. B., Singh P., Blackmore D. and Aubry N., (2007), Transient and steady state of a rising bubble in a viscoelastic fluid, J. Fluid Mech., 589, 215-252.

Rhie M. C, Chow L. W., (1982), A numerical study of the turbulent fow past an isolated airfoil with trailing edge separation, AIAA-82-0998.

Rudman M., (1998), Volume tracking methods for interfacial flow calculations, International Journal for Numerical Methods in Fluids, 24, 671-691.

Rybczynski W. (1911) Über die fortschreitende Bewegung einer flüssigen Kugel in einem zähen Medium. Bull. Acad. Sci. Cracovie, A40. 40-46.

Ross S., (1950), Variation With Temperature of Surface Tension of Lubricating Oils, National Advisory Committee for Aeronautics, Washington.

Rothstein J. P. and McKinley G. H., (2001), Non-isothermal modification of purely elastic flow instabilities in torsional flows of polymeric fluids, Physics of Fluids, 13, 382.

Subramanian R. S and Balasubramaniam R., (2001), The motion of bubbles and drops in reduced gravity, Cambridge University Press.

Subramanian R.S., (1983), Thermocapillary migration of bubbles and droplets, Adv. Space Res., 3, 145-153.

Sussman M. and Fatemi, E., (1999), An efficient,interface-Preserving Level Set Redistancing Algorithm and its application to Interfacial Incompressible Fluid Flow. SIAM Journal of. Scientific Computing, 20, 1165-1191.

Sussman M., Puckett, E., (2000), A coupled level set and volume-of-fluid method for computing 3D and axisymmetric incompressible two-phase flows. Journal of Computational Physics, 162, 301-337.

Sussman S., Smereka, P., and Osher, S., (1994), A Level Set approach for computiong solutions to incompressible two-phase flow. Journal of Computaional Physics, 114, 146-159.

Szymczyk J. A., Wozniak, G. Siekmann, J. (1987), On Marangoni bubble motion at higher Reynolds- and Marangoni-numbers under microgravity. Applied Microgravity Technology, 1, 27-29.

Taylor T. D. and Acrivos A., (1965), On the deformation and drag of a falling viscous drop at low Reynolds number, J. Fluid Mech., 18, 466-476.

Thompson, R. L., Dewitt, K. J., Labus, T. L., (1980), Marangoni bubble motion phenomenon in zero gravity. Chemical Engineering Communications. 5, 299-314.

Thomson J. (1855), On certain curious motions observable at the surfaces of wine and other alcoholic liquors. The London, Edinburgh, and Dublin Philosophical Magazine and Journal of Science. Taylor & Francis.

Treuner M., Galindo, V., Gerbeth, G., Langbein, D., Rath, H. J., (1996), Thermocapillary Bubble Migration at High Reynolds and Marangoni Numbers under Low Gravity. Journal of Colloid and Interface Science. 179, 114-127.

Tryggvason G., Bunner B., Esmaeeli A., Juric D., Al-Rawahi N., Tauber W., Han J., Nas S., and Jan Y.-J., (2001), A Front Tracking Method for the Computations of Multiphase Flow, Journal of Computational Physics, 169, 708-759.

Tryggvason G., Scardovelli R., Zaleski S., (2011), Direct numerical simulations of gas-liquid multiphase flows, Cambridge University Press.

Van Doormaal J. P. and Raithby G. D., (1985), An evaluation of the segregated approach for predicting incompressible fluid flows, In National Heat Transfer Conference, Denver, Colorado, August 4-7 1985.

Vilsmeier R. and HÄanel D., (1993), Adaptive methods on unstructured grids for Euler and Navier-Stokes equations, Computers and Fluids, 22, 485-499.

Warshay, M., Bogusz, E., Johnson, M., and Kintner, R.C., (1959), Ultimate velocity of drops in stationary liquid media, Can. J. Chem. Eng., 37, 29-36.

Williams M. L., Landel R. F. and Ferry J. D., (1955), The temperature dependence of relaxation mechanisms in amorphous polymers and other glass-forming liquids, J. Am. Chem. Soc., 77, 3701–3707.

Wozniak, G., (1991) On the thermocapillary motion of droplets under reduced gravity, J. Colloid Interface Sci. 141, 245-254.

Yamamoto T., Okano Y., Dost S., (2016), Validation of the S-CLSVOF method with the density-scaled balanced continuum surface force model in multiphase systems coupled with thermocapillary flows, International Journal of Numerical Methods in Fluids, 83, 223-244.

Yin Z., Chang L., Hu W., Li Q., and Wang H., (2012), Numerical simulations on thermocapillary migrations of nondeformable droplets with large Marangoni numbers, Physics of Fluids, 24, 092101.

Young, N., Goldstein, J., and Block, M. (1959). The motion of bubbles in a vertical temperature gradient. Journal of Fluid Mechanics, 6, 350-356.

Zana, E. and Leal, L.G., (1978), The dynamics and dissolution of gas bubbles in a viscoelastic fluid, Int. J. Multiphase Flow, 4, 237-262.

Zhao J., Zhang L., Li Z., Qin W., (2011), Topological structure evolvement of flow and temperature fields in deformable drop marangoni migration in microgravity, International Journal of Heat and Mass Transfer, 54, 4655-4663.

Appendices

Terms at the order De_T

$$(1-\beta)\left[d_0 D_0\right]_{rr} = -12\left(1-\beta\right)A^2(12cos^2\theta r^3 - 4r^3 + 3cos^2\theta + 1)/r^8 \qquad (1)$$

$$(1-\beta)\left[d_0 D_0\right]_{r\theta} = (1-\beta)A^2(-96r^3 - 12)sin\theta cos\theta/r^8 \qquad (2)$$

$$(1-\beta)\left[d_0 D_0\right]_{\theta\theta} = (6\left(1-\beta\right)A^2(14(cos^2\theta)r^3 - 6r^3 - 5(cos^2\theta) - 9))/r^8 \qquad (3)$$

$$(1-\beta)\left[d_0 D_0\right]_{\phi\phi} = 6\left(1-\beta\right)A^2(10cos^2\theta r^3 - 2r^3 - 13cos^2\theta - 1)/r^8 \qquad (4)$$

$$p_1 = 18De_T A^2(1-\beta)(-18cos^2\theta r^5 + 6r^5 + 10cos^2\theta\alpha + 10cos^2\theta$$
$$+ 5\alpha + 5)/(5r^8(\alpha+1)) \quad (5)$$

$$\tilde{p}_1 = 1134A^2 De_T(cos^2\theta - 1/3)(\beta-1)r^2/(5\alpha+5) \qquad (6)$$

$$f_1 = 0 \qquad (7)$$

Terms at the order $CaDe_T$

$$\tau_{rr}^{(1)} = A^3 CaDe_T(27378((2/3+\alpha)((r^2+5/39)\alpha + 10r^2(1/13) + 20/39)cos^2\theta$$
$$+ (-491r^2(1/585) - 1/13)\alpha^2 + (-1792r^2(1/1755) - 14/39)\alpha - 80r^2(1/351)$$
$$- 8/39))(\beta-1)cos\theta(\alpha+22/13)/((35(2/3+\alpha))(\alpha+1)^2 r^6) \quad (8)$$

$$\tilde{\tau}_{rr}^{(1)} = 8424A^3 CaDe_T(\beta-1)cos\theta(\alpha+22/13)((\alpha+2/3)((r^2-15/2)\alpha + 4r^2$$
$$- 9)cos^2\theta + (-3r^2(1/5) + 10/3)\alpha^2 + (-14r^2(1/5) + 791/90)\alpha - 8r^2(1/5)$$
$$+ 232/45)r/((35(2+3\alpha))(\alpha+1)^2) \quad (9)$$

$$p^{(1)} = -A^3 CaDe_T(27(5cos^2\theta - 3))(13\alpha+10)(\beta-1)(13\alpha$$
$$+ 22)cos\theta/(70(\alpha+1)^2 r^4) \quad (10)$$

$$\tilde{p}^{(1)} = A^3 C a D e_T (6318((2/3 + \alpha)(\alpha + 4)r^2 cos^2\theta + (-3r^2(1/5) - 35/9)\alpha^2$$

$$+ (-14r^2(1/5) + 35/27)\alpha - 8r^2(1/5) + 140/27))\alpha(\beta - 1)cos\theta(\alpha +$$

$$22/13)r/((35(2 + 3\alpha))(\alpha + 1)^2) \quad (11)$$

Terms at the order De_T^2

$$(1 - \beta)\,[d_0 D_1]_{rr} = 432(\beta - 1)^2 A^3 cos\theta(18cos^2\theta r^5 - 50cos^2\theta r^3 - 12r^5 + 9cos^2\theta r^2$$

$$+ 30r^3 - 4cos^2\theta - 3r^2)/(5r^9(\alpha + 1)) \quad (12)$$

$$(1 - \beta)\,[d_0 D_1]_{r\theta} = -(324(-\beta + 1))A^3(\beta - 1)sin\theta(16cos^2\theta r^5 - 50cos^2\theta r^3 - 4r^5$$

$$+ 5cos^2\theta r^2 + 10r^3 + 2cos^2\theta - 3r^2 + 6)/(5r^9(\alpha + 1)) \quad (13)$$

$$(1 - \beta)\,[d_0 D_1]_{\theta\theta} = (216(-\beta + 1))(21cos^2\theta r^5 - 65cos^2\theta r^3 - 15r^5 - 3cos^2\theta r^2$$

$$+ 45r^3 + 17cos^2\theta - 9r^2 + 15)(\beta - 1)A^3 cos\theta/(5r^9(\alpha + 1)) \quad (14)$$

$$(1 - \beta)\,[d_0 D_1]_{\phi\phi} = (648(-\beta + 1))A^3 cos\theta((r^5 - (7/3)r^3 - r^2 + 7/3)cos^2\theta$$

$$- 3r^5(1/5) + r^3 + (1/5)r^2 - 1/5)(\beta - 1)/(r^9(\alpha + 1)) \quad (15)$$

$$(1 - \beta)\,[d_1 D_0]_{rr} = (3888(-\beta + 1))((r^2$$

$$+ 4/3)cos^2\theta - r^2)cos\theta(\beta - 1)A^3/(5r^9(\alpha + 1)) \quad (16)$$

$$(1 - \beta)\,[d_1 D_0]_{r\theta} = (972(-\beta + 1))A^3 sin\theta(\beta - 1)(5cos^2\theta r^2$$

$$+ 3cos^2\theta - r^2 + 1)/(5r^9(\alpha + 1)) \quad (17)$$

$$(1 - \beta) \, [d_1 D_0]_{\theta\theta} = -(648(-\beta + 1))(9cos^2\theta r^2 - 2cos^2\theta - 3r^2$$
$$- 6)A^3cos\theta(\beta - 1)/(5r^9(\alpha + 1)) \quad (18)$$

$$(1 - \beta) \, [d_1 D_0]_{\phi\phi} = -(648(-\beta + 1))A^3cos\theta(\beta - 1)(9cos^2\theta r^2 - 10cos^2\theta$$
$$- 3r^2 + 2)/(5r^9(\alpha + 1)) \quad (19)$$

$$(1 - \beta) \left[d_0^2 D_0\right]_{rr} = -(24(1 - \beta))A^3cos\theta(100cos^2\theta r^6 - 60r^6 + 40cos^2\theta r^3$$
$$- 5cos^2\theta - 3)/r^{12} \quad (20)$$

$$(1 - \beta) \left[d_0^2 D_0\right]_{r\theta} = -(36(1 - \beta))A^3sin\theta(50cos^2\theta r^6 - 10r^6 + 5cos^2\theta r^3$$
$$- 9r^3 + 2cos^2\theta + 4)/r^{12} \quad (21)$$

$$(1 - \beta) \left[d_0^2 D_0\right]_{\theta\theta} = (24(1 - \beta))A^3cos\theta(65cos^2\theta r^6 - 45r^6 - 40cos^2\theta r^3$$
$$- 48r^3 + 29cos^2\theta + 48)/r^{12} \quad (22)$$

$$(1 - \beta) \left[d_0^2 D_0\right]_{\phi\phi} = (24(1 - \beta))A^3cos\theta(35cos^2\theta r^6 - 15r^6 - 100cos^2\theta r^3$$
$$+ 12r^3 + 65cos^2\theta + 12)/r^{12} \quad (23)$$

$$p_2 = 27De_T^2 A^3(\beta - 1)(12215cos^2\theta\alpha^2 + 19383cos^2\theta\alpha\beta - 19928cos^2\theta\alpha$$
$$- 18642cos^2\theta\beta + 5882cos^2\theta + 735\alpha^2 - 4641\alpha\beta + 21096\alpha + 18174\beta$$
$$- 2454)cos\theta/(455(\alpha + 1)^2) \quad (24)$$

$$\tilde{p}_2 = -A^3 De_T^2(113724((2/3 + \alpha)(\beta + 111\alpha(1/169) - 58/169)cos^2\theta$$

$$- 27953\alpha^2(1/68445) + (-3\beta(1/5) - 5848/68445)\alpha - 2\beta(1/5)$$

$$+ 8416/68445))cos\theta(\beta - 1)/((7(2 + 3\alpha))(\alpha + 1)^2) \quad (25)$$

$$f_2 = -(11664(((\beta - 1)r^5 + (-25\alpha(1/54) - 25/54)r^3 + 10\alpha(1/27)$$

$$+ 10/27)cos^2\theta + ((1/15)\beta - 1/15)r^5 + (-125\alpha(1/162) - 125/162)r^3$$

$$+ 28\alpha(1/81) + 28/81))(\beta - 1)sin\theta A^3/(r^{13}(\alpha + 1)) \quad (26)$$